Understanding Nanoscale Surface Roughness and its Effect on Macroscale Adhesion

by

Abhijeet Gujrati

Bachelor of Engineering (Hons.), BITS Pilani | K.K. Birla Goa Campus, 2012

Master of Science, University of Pittsburgh, 2014

Submitted to the Graduate Faculty of the

Swanson School of Engineering in partial fulfillment

of the requirements for the degree of

Doctor of Philosophy

University of Pittsburgh

2020

UNIVERSITY OF PITTSBURGH

SWANSON SCHOOL OF ENGINEERING

This dissertation was presented

by

Abhijeet Gujrati

It was defended on

March 17, 2020

and approved by

Dr. William Slaughter, Ph.D., Associate Professor, Department of Mechanical Engineering and Materials Science

Dr. Markus Chmielus, Ph.D., Associate Professor, Department of Mechanical Engineering and Materials Science

Dr. Maarten de Boer, Ph.D., Professor, Department of Mechanical Engineering, Carnegie Mellon University

Dissertation Director: Dr. Tevis Jacobs, Ph.D., Assistant Professor, Department of Mechanical Engineering and Materials Science

Copyright © by Abhijeet Gujrati

2020

Understanding Nanoscale Surface Roughness and its Effect on Macroscale Adhesion

Abhijeet Gujrati, PhD

University of Pittsburgh, 2020

Surface roughness affects the functional properties of surfaces, including adhesion, friction, and wear. However, experimental investigations to quantify these links are often inconclusive, primarily because surfaces are fractal and the values of measured roughness parameters depend on measurement size. The objectives of this dissertation research were two-fold: first, to establish a new way to characterize multi-scale topography; and second, to demonstrate how it can be used to understand the effect of topography on surface properties.

In the present research the topography of rough surfaces was characterized beyond the limits of conventional surface measurement techniques. Using transmission electron microscopy, surface features were measured down to the Ångström-scale. This small-scale topography information was combined with conventional larger-scale surface characterization to achieve a comprehensive surface description spanning eight orders of magnitude in size. Data from various length scales were combined using the power spectral density (PSD), and this was used to compute scale-independent roughness parameters. This approach was applied to four different types of polycrystalline diamond films to interrogate differences between materials with similar surface chemistry but different surface topography.

Then, this comprehensive description of topography was used to understand the topography dependence of soft-material adhesion. Specifically, adhesion measurements with *in situ* observation of contact size were performed using soft elastic polydimethylsiloxane

hemispheres (modulus ranging from 0.7 to 10 MPa) on the polycrystalline diamond films of varying roughness. The results showed that the apparent work of adhesion when coming into contact was reduced below the intrinsic value by the energy required to achieve conformal contact. Further, the total energy lost during contact and removal is equal to the product of the intrinsic work of adhesion and the true contact area. These findings provide a simple mechanism to quantitatively understand the dependence of soft-material adhesion on surface roughness.

Table of Contents

List of Tables

List of Figures

Preface

Foremost, I want to express my deepest gratitude to my research advisor, Dr. Tevis D.B. Jacobs, thank you very much for taking a chance on a random student who knocked your office door on that fateful September evening. Due to his expert guidance, motivation and immense knowledge I was able to complete my Ph.D. study and research.

Next, I would like to thank Dr. Lars Pastewka from University of Freiburg and Dr. Ali Dhinojwala from The University of Akron, for their collaboration and help with all my research.

I want to thank mom and dad for their patience and encouragement. They provided me with everything that I ever needed and more. To my lovely wife, my rock, Harsha, she was always by my side through sleepless nights and through rough days, though we have been living apart for my complete Ph.D. she never made me feel alone. I will always be in your gratitude.

My sincere thanks to my committee, Dr. William Slaughter, Dr. Markus Chmielus and Dr. Maarten de Boer, for all their insightful comments and all their questions, they were extremely helpful.

Finally, I would be remiss if do not thank Jacobs research group: Sai, Subarna, Sunny, Luke and Andrew for all the support and help.

1.0 Background on the Effect of Roughness on Adhesion

A fundamental understanding of adhesion is of critical importance in many small-scale devices and advanced manufacturing techniques. The micro- and macroscopic surface adhesion is predicted to be strongly affected by surface topography across many length scales. It was realized more than a century ago[1] that nominally planar surfaces will only make contact at the points of highest protrusion because of surface roughness. The area of close mechanical contact can thus be thousands of times smaller than the projected, apparent area of the surface. Although adhesive interactions are well understood for atomically smooth interfaces,[2,3] adhesion is not quantitatively understood for most manufactured components, which contain multi-scale roughness. There are many analytical models which predict adhesion as a function of single- or multi-scale roughness;[4–8] however, these models have not been sufficiently verified experimentally and cannot be readily applied to real-world surfaces. A primary cause for this lack of experimental application is the fractal-like multi-scale nature of typical surface roughness, such that different measurements yield different results. Furthermore, conventional experimental techniques fail to accurately capture the smallest-scales of topography, which many models predict to be the most important for determining surface adhesion. Thus, there is a critical need for (1) improved approaches for the characterization of surface topography and (2) quantitative experimental testing of models that describe the effect of roughness on surface adhesion.

Many investigations have attempted to connect surface properties with a single statistical roughness parameter (like the scalar parameter R_a[9]) at a single scale of measurement. This line of investigation has led to contradictions in the literature, an example of which is discussed in a 2013 review about bone marrow stromal cells on ceramic materials, which concluded that, “overall, the

effect of surface roughness (at both the nano- and micron-scales) and grain size on cell adhesion is inconclusive due to contradicting data in the literature".[10] A few decades ago Mandelbrot[11] explained this paradox. In the paper titled "How Long is the Coast of Britain?", he explained that the length of coast is determined by the length of yardstick used to measure the coast. This fractal-like property is demonstrated by rough surfaces as well, and thus scalar properties like root-mean-square (RMS) roughness are highly dependent on scale of measurement.[12]

Analytical[4,6–8,13] and numerical[14–16] models account for the self-affine nature of surfaces and suggest that surface properties can be predicted from a complete statistical description of the surface in the form of the power spectral density (PSD)[17] or the autocorrelation function (ACF).[18] These same investigations suggest that adhesion, friction, and contact stiffness depend on the *true* values of RMS height h_{rms}, RMS slope h'_{rms}, and in the case of adhesion[8] also RMS curvature h''_{rms}. This conclusion leads to a central challenge in roughness analysis: functional properties of a surface depend on the true scale-spanning topography, while any experimental measurement of topography is inherently technique-dependent and incomplete. The resolution to this challenge is to combine measurements across length scales and, unlike with Mandelbrot's coastlines, to measure down to the smallest sizes, where scaling laws must break down.

This prior work leads us directly into the problem of measuring at very small scales (a few nanometers). More recently, it has also been shown – in analytical and numerical models of single-scale [4,19] and multi-scale [6,20] roughness – that a critical quantity controlling surface properties is the root-mean-square slope of the surface h'_{rms}. This quantity has been directly linked to true contact area, adhesion, and friction between surfaces. Further, for a surface with multi-scale roughness, the smallest-scale features dominate h'_{rms}, which is shown schematically in Fig 1a, and is shown mathematically in the equations for computing h'_{rms} from a real-space or frequency-space

description of a surface [20,21]. However, conventional surface measurement techniques (such as stylus or optical profilometry, and atomic force microscopy) are incapable of reliably measuring roughness at the smallest lateral length scales, primarily due to tip-size artifacts and noise in the measurements [17]. Therefore, it is impossible to accurately measure this critical quantity h'_{rms} with conventional techniques. Instead, new approaches are required for measuring surface topography at the smallest scales.

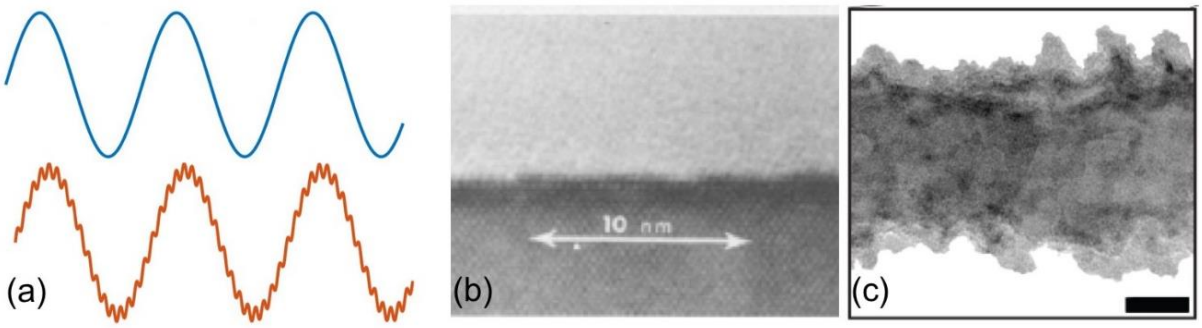

Figure 1 The smallest-scale roughness has the biggest impact on local surface slope; yet it is hardest to measure. A simple schematic (a) shows a single sinusoid (top) with a root-mean-square slope of 0.5, and the superposition of a second sinusoid with a smaller amplitude (1/10th of the original) and a smaller wavelength (1/15th of the original), which raises the root-mean-square slope to 1.0. Early TEM measurements (b) of the boundary between single-crystal silicon and its oxide were used to measure the topography of interfaces. More recent TEM measurements (c) enable the characterization of free-surface topography, but only on nanoparticles or nanowires that are electron transparent by nature. The scale bar in (c) is 20 nm. Image (a) reproduced from Ref.[22], copyright Suface Topography: Metrology and Properties, 2018. Image (b) reproduced from Ref. [23], copyright The Electrochemical Society, 1987. Image (c) reproduced from Ref. [24], copyright American Chemical Society, 2012.

Many early investigations reported only the maximum height variation observed along the interface, and correlated this height variation with growth conditions [23]. However, Goodnick and coauthors [25] went further, digitizing the interface contour, and thus enabling its statistical characterization. The authors computed scalar roughness parameters, such as the root-mean-square

height fluctuation and the correlation length. This pioneering work on the characterization of native silica roughness has been widely adopted in the study of interfaces and understanding its effect on properties (for a more recent example, Ref [26]). It has also been applied to the TEM characterization of surface roughness in nanowires [24], which are electron transparent in their native state. However, this same framework has not been widely applied to the general study of surface topography of engineered components. This lack of use likely stems primarily from the difficulty of preparing a free surface for TEM examination. There are two typical approaches for preparing a thin section for TEM examination; first common technique, the focused ion beam (FIB) lift-out, uses a FIB to mill two adjacent trenches with a free-standing thin lamella in between. While this technique is efficient and extremely widely used for materials analysis, it cannot be done without altering the original surface, and second so-called "conventional" cross-section preparation involves grinding and glancing-angle ion milling. The conventional technique is well documented elsewhere (for example, Refs. [27,28]). When performed in its normal fashion, the outermost surface can be removed or damaged during the grinding and low-angle ion milling. A modified version of this process is discussed in detail in the section 4.1.3 and 4.2.5 of the present articles, which is used to preserve the surface.

1.1 Single-scale Analytical Models.

The most influential early analytical theory for contact between rough surfaces is the 1966 model of Greenwood and Williamson[19], which represents a rough contact as a large number of non-interacting spherical asperities with identical radius and a Gaussian distribution of heights. Hertzian contact mechanics is applied to each asperity individually. Fuller and Tabor[29] and

Maugis[5] extended the Greenwood-Williamson models to include JKR and DMT adhesion, respectively. Many authors have since extended these models to include different distributions of heights to yield closed-form analytical predictions[30–32]. The critical input parameters for this class of model are: the radius of curvature of asperities; the asperity density; and the distribution of asperity heights. Various authors[4,33] discuss ways to relate these quantities to the root-mean-square height, slope, and curvature (of hrms, h'rms, and h''rms, respectively) of real surfaces.

1.2 Multi-scale Analytical Models.

Persson[6,34] has presented an analytical theory for the elastic contact of randomly rough surfaces, with topography on multiple length scales. This theory takes as an input the spectral distribution of a surface, and solves for the contact area, load-displacement relations, and pressure distributions inside the contact. Persson's theory predicts proportionality between contact area and load over a large range of loads, which is in good agreement with experimental findings[35] and numerical calculations[36], and is consistent with Amontons' widely-observed friction law[37,38]. This theory has been subsequently extended for adhesive contact[7,34,39–41]. Persson's theory and its extensions identify the RMS slope h'rms as the critical parameter controlling contact[36,42]. Crucially, while RMS height depends primarily on the largest-scale contributions to roughness, the RMS slope depends mostly on contributions from the smallest length scales[6].

*Note - Portions of the text have been taken (with or without modification) from my publications:

1. Gujrati, A.*; Khanal, S. R.*; Pastewka, L.; Jacobs, T. D. B. Combining TEM, AFM, and Profilometry for Quantitative Topography Characterization Across All Scales. *ACS Appl. Mater. Interfaces* **2018**, *10* (34), 29169–29178. © American Chemical Society, 2018.
2. Khanal, S. R.; Gujrati, A.; Vishnubhotla, S. B.; Nowakowski, P.; Bonifacio, C.; Pastewka, L.; Jacobs, T. D. B. Characterizing Small-Scale Topography Using Transmission Electron Microscopy. *Surf. Topogr. Metrol. Prop.* **2018**, *6* (4), 45004. © Surface Topography: Metrology and Properties, 2018.
3. Gujrati, A.; Khanal, S. R.; Jacobs, T. D. B. A Method for Quantitative Real-Time Evaluation of Measurement Reliability When Using Atomic Force Microscopy-Based Metrology. *2017 IEEE 17th Int. Conf. Nanotechnology, NANO 2017* **2017**, 135–138. © IEEE, 2017.
4. Dalvi, S.*; Gujrati, A.*; Khanal, S. R.; Pastewka, L.; Dhinojwala, A.; Jacobs, T. D. B. Linking Energy Loss in Soft Adhesion to Surface Roughness. Proc. Natl. Acad. Sci. U.S.A. **2019**, *116* (51), 25484-25490. © National Academy of Sciences, 2019.

2.0 Goal and Objectives

The goal of the present research is to develop new approaches to achieve comprehensive, scale-invariant descriptions of experimental surfaces that can be used to predict surface properties. The overall approach to achieve this goal is to harness existing experimental techniques (including atomic force microscopy, profilometry, and electron microscopy) and analysis techniques (including the power spectral density), and to advance and combine them in novel ways. These comprehensive descriptions can be combined with analytical and numerical models of rough-surface behavior to describe, predict, tailor and optimize surface properties.

Specifically, this goal has been pursued via three objectives:

Objective 1: Establishing and validating new approaches for surface characterization

Objective 2: Measuring a comprehensive, multi-resolution description of a technologically relevant surface.

Objective 3: Experimentally measure surface adhesion to interrogate the many competing rough-surface mechanics models.

3.0 Methods

3.1 Nanodiamond Synthesis

Nanodiamond films (Advanced Diamond Technologies, Romeoville, IL) were deposited using a tungsten hot-filament chemical vapor deposition (HFCVD) system with parameters as described in Ref. [43]. An H-rich gas mixture was used, with the chamber pressure of 5 Torr and a substrate temperature of 750°C. The ratio of boron to carbon was maintained at 0.3 at%, to achieve high conductivity in the final film. The CH4-to-H2 ratio is modified (as described in Ref.[44]) to tune the grain size: achieving microcrystalline diamond (MCD), nanocrystalline diamond (NCD), and ultrananocrystalline diamond (UNCD). All films were grown to a thickness of 2 microns. Chemical-mechanical planarization was performed on an undoped UNCD film to create the polished UNCD samples. A 2-μm-thick film of UNCD was deposited in the same batch on polished silicon wafers and microfabricated silicon wedges.[45]

3.2 Experimental Techniques for Surface Topography Measurement

3.2.1 Stylus Profilometry

The largest scales of topography were measured using one-dimensional line scans with a stylus profilometer (Alpha Step IQ, KLA Tencor, Milpitas, CA) with a 5-μm diamond tip. Data were collected at a scanning speed of 10 μm/s, with data points every 100 nm. A total of 8

measurements were taken on each substrate, with 2 measurements each at scan sizes of 0.5, 1, 2, 5 mm. These measurements were taken at random orientations of the sample and did not show meaningful variations with direction. A parabolic correction was applied to all measurements which removed the tilt of the sample and the bowing artifact from the stylus tool. In two sessions (for the UNCD and polished UNCD), the larger scan sizes exhibited consistent non-parabolic trends due to instrument artifacts. In these cases, this was corrected by performing reference scans on polished silicon wafers and subtracting the averaged profiles from all measurements.[45]

3.2.2 Atomic Force Microscopy

The substrates were measured using an atomic force microscope (AFM) (Dimension V, Bruker, Billerica, MA) in tapping mode with diamond-like carbon-coated probes (Tap DLC300, Mikromasch, Watsonville, CA). For all substrates, a total of 11 square measurements were taken with the following lateral sizes: 3 scans each at 100 nm, 500 nm, and 5 μm; 1 scan each at 250 nm and 1 μm. The scanning speed was maintained at 1 μm/s for all scans. Each scan had 512 lines, with 512 data points per line, corresponding to pixel sizes in the range of 0.2 to 98 nm. The values of free-air amplitude and amplitude ratio were kept in the range of 37 – 49 nm and 0.15 – 0.3, respectively. While AFM provides a two-dimensional map of surface topography, the data were analyzed as a series of line scans, both to facilitate direct comparison with other techniques and to avoid apparent anisotropy due to instrument drift.[45]

3.2.3 Transmission Electron Microscopy

Topography was measured on scales from microns to Ångströms following the approach developed in Ref.[22]. For the UNCD, NCD, and MCD, the "wedge deposition technique" was used, whereas for polished UNCD, the "the surface-preserving cross-section technique"[22] was used. Briefly, the wedge deposition technique involves depositing the film of interest, in the same batch, on both flat silicon wafers (used for adhesion testing) and on standardized TEM-transparent silicon wedge samples (for TEM imaging). The surface-preserving cross-sectioning technique is similar to conventional techniques for extraction of a TEM cross-section from a bulk sample (using grinding, polishing, dimple-grinding, and ion etching); however, modifications to the ion etching step ensure that the original surface topography is unmodified from its original state. The samples were imaged using a TEM (JEOL JEM 2100F, Tokyo, Japan) operated at 200 keV. The images were taken with a 2000x2000-pixel camera using magnification levels from 5000x to 600,000x.[45]

The nanoscale surface contours were extracted from the TEM images using custom Matlab scripts that create a digitized line profile based on a series of points selected by the user. The TEM images obtained were first rotated to make the surface horizontal and then the outer-most boundary was traced. While the vast majority of the measured surfaces were well-behaved functions *(i.e.*, there was a single value of height (y-axis) for each horizontal position (x-axis), there were some cases where two adjacent points were captured with identical or decreasing horizontal position. In these cases, the latter point was removed. In just 12 out of the 210 measurements, there were small portions of the profile that were reentrant. This character is not necessarily physically meaningful as it depends on the rotation of the TEM image during image analysis. Because the mathematical analyses (especially the calculation of PSD) require well-behaved functions, these regions were excluded from analysis.

3.3 Analysis Techniques for Characterization of Surface Topography

3.3.1 Power Spectral Density

For a line scan with height $h(x)$ over lateral position x, the Fourier transform of the surface topography is given by $\tilde{h}(q) = \int_0^L h(x)e^{-iqx}dx$. The PSD[17] is the Fourier transform of the autocorrelation of $h(x)$ or, equivalently, the square of the amplitude of $\tilde{h}(q)$; *i.e.*, $C(q) = L^{-1}\left|\tilde{h}(q)\right|^2$. For a self-affine line scan, the PSD will show power-law scaling of the form $C(q) = C_0 q^{-1-2H}$, where C_0 is a constant. This enables the extraction of a Hurst exponent from the self-affine region of the combined PSD.

The combined PSD represents the arithmetic average of all of the individual PSDs that were computed from each topography measurement. Because random surfaces are often described as Gaussian random fields (according to the random process model of surface roughness[46]) then each value of $\tilde{h}(q)$ should be a complex number that has random real and imaginary components distributed according to a Gaussian distribution. Therefore, $C(q)$ should be distributed according to a χ^2-distribution with 2-degrees of freedom, *i.e.*, an exponential distribution. Therefore, the maximum likelihood estimator for true value of C(q) is computed from the arithmetic averages of the individual measurements.[47]

*Note - Portions of the text have been taken (with or without modification) from my publications:

1. Gujrati, A.*; Khanal, S. R.*; Pastewka, L.; Jacobs, T. D. B. Combining TEM, AFM, and Profilometry for Quantitative Topography Characterization Across All Scales. *ACS Appl. Mater. Interfaces* **2018**, *10* (34), 29169–29178. © American Chemical Society, 2018.
2. Khanal, S. R.; Gujrati, A.; Vishnubhotla, S. B.; Nowakowski, P.; Bonifacio, C.; Pastewka, L.; Jacobs, T. D. B. Characterizing Small-Scale Topography Using Transmission Electron Microscopy. *Surf. Topogr. Metrol. Prop.* **2018**, *6* (4), 45004. © Surface Topography: Metrology and Properties, 2018.
3. Gujrati, A.; Khanal, S. R.; Jacobs, T. D. B. A Method for Quantitative Real-Time Evaluation of Measurement Reliability When Using Atomic Force Microscopy-Based Metrology. *2017 IEEE 17th Int. Conf. Nanotechnology, NANO 2017* **2017**, 135–138. © IEEE, 2017.
4. Dalvi, S.*; Gujrati, A.*; Khanal, S. R.; Pastewka, L.; Dhinojwala, A.; Jacobs, T. D. B. Linking Energy Loss in Soft Adhesion to Surface Roughness. Proc. Natl. Acad. Sci. U.S.A. **2019**, *116* (51), 25484-25490. © National Academy of Sciences, 2019.

4.0 Results and Discussions for Objective 1: Establishing and Validating New Approaches for Surface Characterization

4.1 Multi-scale Topography Measurement

4.1.1 Stylus Profilometry and Atomic Force Microscopy Measurements

The UNCD film was measured using conventional surface topography techniques, for the purposes of combining with the TEM measurements, in order to create a comprehensive description of the surface. The UNCD film was characterized (see Methods) using stylus profilometry and atomic force microscopy (AFM), as shown in Fig. 2a-c. The measurements included 20 stylus scans with sizes from 0.3 to 10 mm, and 28 AFM scans with sizes from 100 nm to 50 μm. Values of commonly used roughness parameters were computed, including RMS height h_{rms}, RMS slope h'_{rms}, and RMS curvature h''_{rms}, as well as the full surface area A_{surf}. Further, we performed a quantitative analysis of tip-size artifacts following the approach of Refs. [17,48] (as described in Methods). This analysis demonstrates a strong tip effect, especially at the smaller length scales. For stylus measurements (Fig. 2d), the entire region that appears to show self-affine scaling was artifacted and thus unreliable. The AFM data also showed significant sensitivity to tip-radius effects, which were exacerbated by wear-induced tip blunting. Even using best-practices (tapping mode with low tip wear, and accounting for the reliability cut-off), conventional surface characterization techniques were unable to capture the roughness of UNCD at lateral length scales smaller than tens of nm. While AFM (and also scanning tunneling microscopy) techniques can achieve Ångström-scale resolution on atomically-flat samples,[49] for most engineering surfaces the

interaction of the tip size and the surface roughness imposes a minimum lateral length scale for reliable measurement. These tip-size artifacts in topography measurements underscore the need for combination with TEM-based Ångström-scale measurements to accurately characterize a surface across all scales.

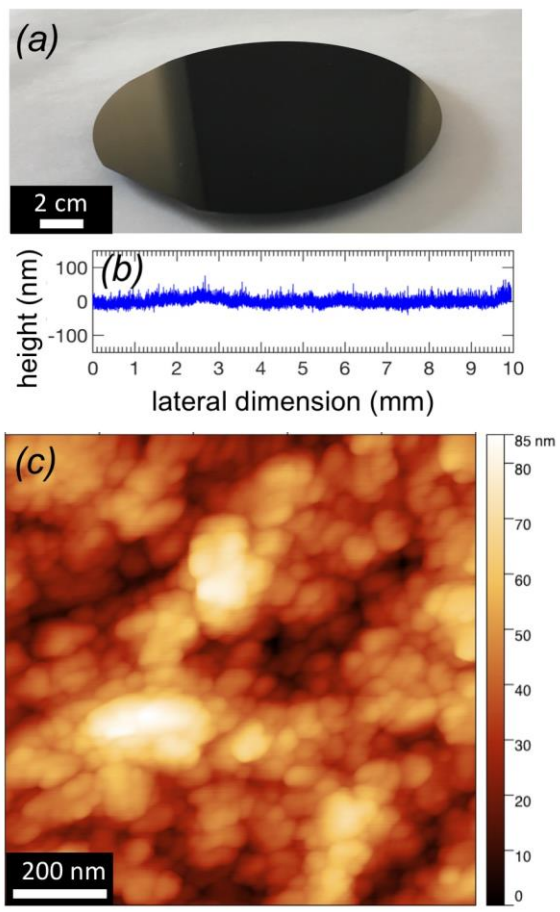

Figure 2 Complementary topography characterization is performed using conventional techniques, and underscores the unreliability of measurements at the smallest lateral length scales. The UNCD film, which has a mirror-like external appearance (a), was characterized using stylus profilometry (b) and AFM (c). The power spectral density (d, e) was computed and tip-size artifacts accounted for (see Methods). For stylus data, the PSD of each measurement is shown; for AFM data, each curve represents an average of all line-scans taken in a single square measurement. The left-most portions of the measured PSD curves (solid, darker-color lines) are considered reliable; beyond the reliability cutoff (dashed vertical line), the remaining data (dashed, lighter-color lines) is considered artifacted. For the stylus measurements, the entire region that appears to be self-affine is unreliable. The AFM-based PSDs enable measurements to smaller sizes, but tip wear can reduce reliable lateral resolution by at least an order of magnitude. Tip wear was detected using TEM images of the tip taken before and after use (insets in (e)). Even the lowest-wear probes could not accurately characterize the statistics of topography for UNCD at lateral length scales below several tens of nanometers. Images (a), (b), (c), (d) and (e) reproduced from Ref.[47], copyright American Chemical Society, 2018.

4.1.2 Transmission Electron Microscopy Measurements

Here, transmission electron microscopy is used to achieve these smallest-size-scale measurements for ultrananocrystalline diamond. Specifically, a 2-μm film was deposited (see Methods) onto a thin-wedge TEM substrate and 79 side-view images of the surface were taken on scales from hundreds of nanometers down to Ångströms (Fig. 3a-c). Each image was post-processed to digitize the contour of the surface, thereby extracting line profiles. These profiles were then analyzed as topographic line contours, analogous to measurements from a stylus profilometer or a line-scan from an AFM. These TEM-based measurements were also used to compute the power spectral density of topography for a statistical description of the surface. See Methods for details of the TEM measurement and image analysis, as well as the calculation of roughness parameters and PSDs. Most importantly, the TEM-measured PSD of the UNCD film (Fig. 3d) enables characterization of topography over lateral length scales ranging from tens of nm down to 4 Å – a regime of roughness that has not been measured in prior investigations of UNCD (e.g., Ref. [50]) and which is not accessible using any conventional technique for topography measurement.[17]

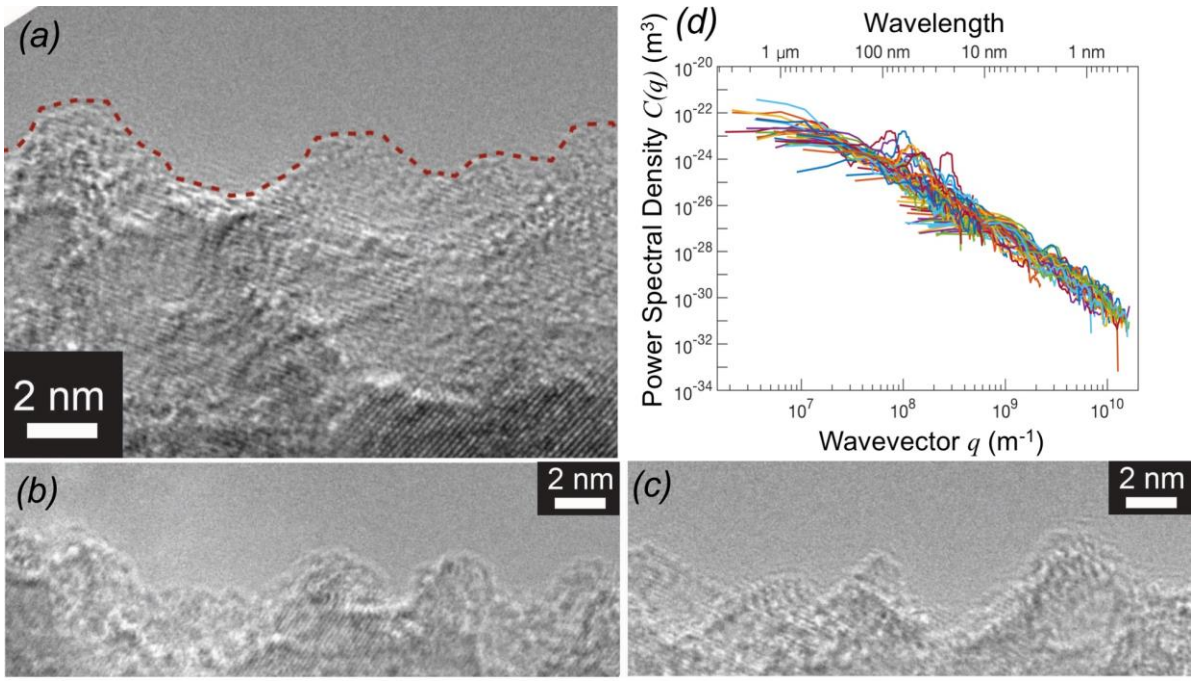

Figure 3 Transmission electron microscopy reveals the surface structure at the Ångström-scale. The topography was captured using side-view TEM images with a wide range of magnifications, resulting in image sizes ranging from over a micron to less than 10 nm. Representative high-resolution images are shown (a-c). The topography was extracted from the outermost contour of the surface (red dashed line in panel a). The power spectral density (d) was computed from each measurement of topography at various magnifications. Overall, the TEM measurements yield topography in size ranges between tens-of-nm and few-Å, which is inaccessible using conventional topography measurement techniques. Images (a), (b) and (c) reproduced from Ref.[47], copyright American Chemical Society, 2018.

While the TEM has been used previously to measure *interface* roughness, the only TEM analysis of *free-surface* topography has been on nanoparticles and nanowires, which are electron transparent by nature. Using the TEM to characterize surface topography of general surfaces presents two difficulties: the preservation of the free surface during TEM sample preparation; and the analysis of the surface contour once it is created, especially with the question of how the TEM's 2D projection affects the measurement of topography.

Two different approaches were used: (1) a modified version of the "conventional" cross-section preparation technique, which we call the surface-preserving cross-section technique; and (2) a simple deposition of the surface of interest onto a thin-wedge substrate that is already electron transparent, which we call the wedge deposition technique. The first technique is generally applicable to all materials; the second technique can only be used for materials that can be deposited or grown in a thin layer.[22]

4.1.2.1 Method 1: Sample Creation for Bulk Materials: The Surface-preserving Cross-section Technique

The process is shown schematically in Fig. 4. For bulk materials, two surface-containing pieces of material are removed from the bulk, typically using a low-speed saw. For the present samples, which were supported by a silicon wafer substrate, two 4x5-cm pieces were cut out using an ultrasonic disk cutter (Model 170, Fischione Instruments, Export, PA). These two small pieces were sandwiched, with the surfaces of interest facing each other, with additional "dummy" silicon wafers added to increase the top-to-bottom thickness. A carbon-based adhesive secures the pieces together, and also prevents the surfaces of interest from making direct mechanical contact and damaging one another. Once the structure is bonded, a cylindrical core (3 mm in diameter) is extracted using the same ultrasonic disk cutter with a circular cutting bit. This cylindrical core is

inserted into a brass tube and is then sliced into thin (~0.5 mm) discs using a wafer saw. These discs are ground (using grits of 600 to 1200) and polished (using 6-µm to 1-µm diamond lapping) to a thickness of 0.1 mm using a specimen grinder tool (Model 160, Fischione Instruments). These thin disks were then dimpled using a dimpling grinder (Model 200, Fischione Instruments) to a minimum thickness of approximately 10 µm. Finally, glancing angle ion milling (Model 1050, Fischione Instruments) is used to only just achieve perforation of the sample in region of interest.[22]

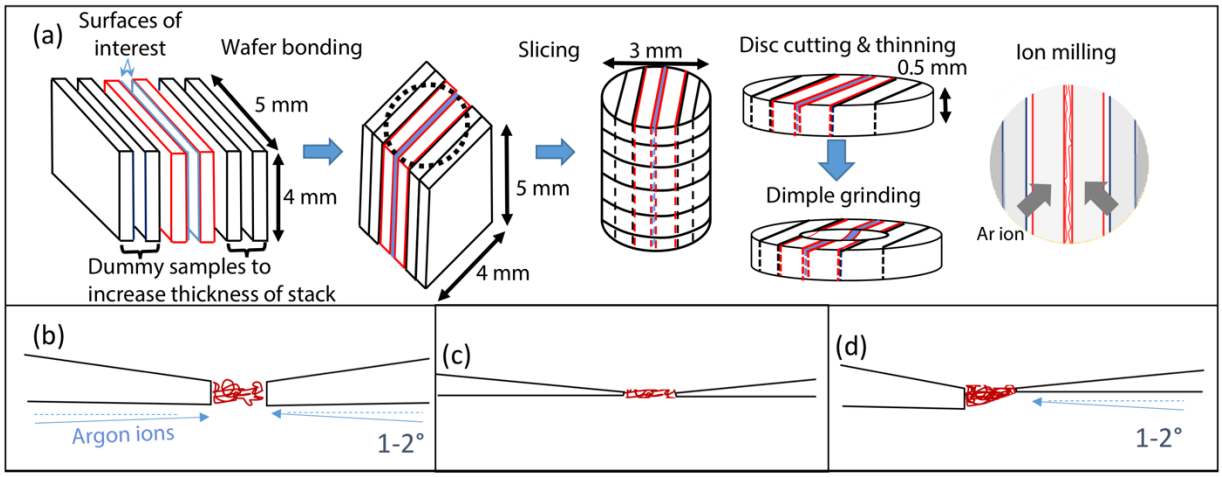

Figure 4 For bulk samples, a cross-section must be prepared for TEM imaging, but with extra care to preserve the original surface. The so-called "conventional" cross-section preparation is shown schematically in panel (a). The principal modifications for surface surface-preserving cross-sections include: the use of low-energy, ultra-low-angle ion milling (b); the characterization of a region which never fully perforates, and still has some adhesive present (c); and optionally, the use of single-side milling to ensure that on efface is free from direct impingement of ions (d). Images (a), (b), (c) and (d) reproduced from Ref.[22], copyright Suface Topography: Metrology and Properties, 2018.

There are two sets of slight modifications required for the creation of surface-preserving cross-sections. First, extra care is required during the ion milling process to avoid damaging the free surface. This was achieved by applying a low incidence milling angle of ±2° during thinning, in contrast to the typically used angle of ±5° or higher. Because of this small angle, the thinning

can only proceed from the non-dimpled side because the dimpled side has a steeper angle and the region of interest will be shadowed. Further, a lower energy of ions was used for the final thinning steps (2 keV instead of typically used 4 keV) and the sample condition is checked more frequently. These last two modifications add time but ensure that thinning does not proceed too rapidly and damage or destroy the free surface.[22] Second, while the sample is normally milled all the way until perforation in the region of interest, here the region of interest was thinned down to *near* perforation, to ensure minimal exposure of the free surface to the ions. This was achieved by attaining perforation in a location adjacent to the region of interest, and then carefully increasing the size of the perforated hole until it approached (but did not reach) the region of interest. The characterization can then be performed only in regions where the adhesive remains intact, or where the adhesive has only *just* been removed. In the former region, the original surface has never been directly exposed to the ion beam; in the latter region, the ion exposure of the surface is minimal.[22] Third, for especially beam-sensitive materials, single-side ion milling can be performed. This ensures that the ions can never impinge directly on the free surface.[22]

4.1.2.2 Method 2: Sample Creation for Thin-film Materials: The Wedge Deposition Technique

For thin-film materials that can be grown or deposited, the preparation for TEM is simpler because they can be applied to a substrate that is already electron transparent. In general, such a substrate can be microfabricated, *e.g.*, by anisotropic etching of silicon, or can be made by purchasing and/or modifying a commercial TEM specimen grid. In the present investigation, the 2-μm-thick UNCD, NCD and MCD films were applied to a commercial substrate (Hysitron Picoindenter wedge samples, Bruker, Billerica, MA). These substrates have a microfabricated wedge that is several millimeters in length, with a thickness that tapers from several microns at the

base to either 1 micron or 100 nm at the apex (Fig. 5). This geometry provides a long region that is electron transparent, while the flat plateau enables the approximation of deposition on a flat substrate. For films with large residual stresses or other geometry dependence, the thicker 1-μm plateau is recommended, as the larger lateral area provides more mechanical constraint. However, for the present work, the UNCD, NCD and MCD films were deposited using a process specifically designed to reduce residual stress (as discussed in Ref. [43]); therefore, the narrow 100-nm plateau was used to minimize the through-thickness for optimal imaging.[22]

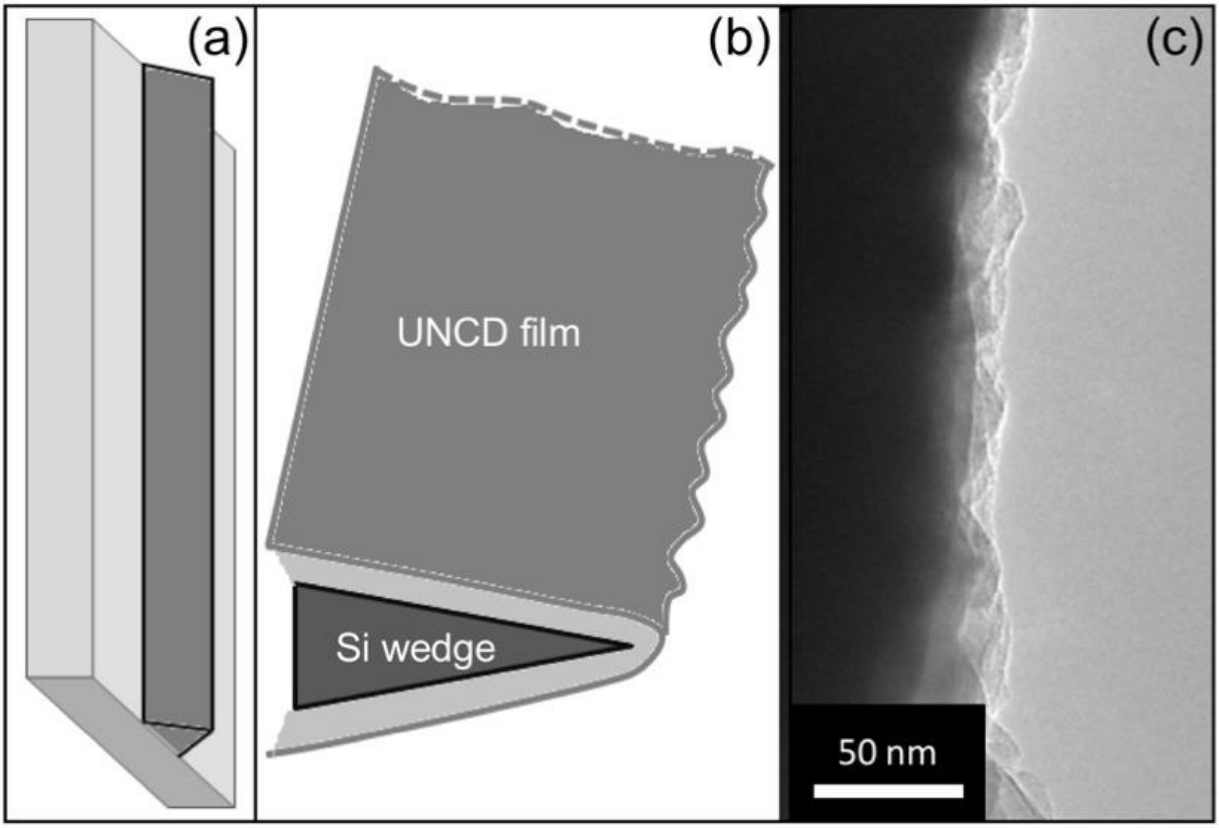

Figure 5 For deposited samples, a pre-fabricated thin-wedge substrate provides a simple route to TEM sample preparation. A commercial substrate was used (a) which contains a large (mm-scale) flat carrier chip with a long, narrow microfabricated wedge. tapered wedge was coated with the UNCD material of interest (b) and then imaged in profile in the TEM (c). Images (a), (b) and (c) reproduced from Ref.[22], copyright Suface Topography: Metrology and Properties, 2018.

The individual measurements of root-mean-square height, slope, and curvature were computed from each line scan by numerically integrating in real-space:

$$h_{\mathrm{rms}}^2 = \frac{1}{L}\int_0^L h^2(x)\,dx, \qquad h_{\mathrm{rms}}'^2 = \frac{1}{L}\int_0^L \left(\frac{dh}{dx}\right)^2 dx, \qquad h_{\mathrm{rms}}''^2 = \frac{1}{L}\int_0^L \left(\frac{d^2h}{dx^2}\right)^2 dx \qquad 4\text{-}1$$

These general equations for RMS height, slope, and curvature (h_{rms}, h'_{rms}, and h''_{rms}, respectively) are implemented using the trapezoidal method. While the trapezoidal method is simple and standardized, its implementation here takes on a slightly unique form because of the embedded derivatives. Using a Taylor expansion of the derivatives, a trapezoidal implementation of Eq. 4-1 takes the following form:

$$h_{\mathrm{rms}}^2 = \frac{1}{L}\sum_{i=2}^{N}\left[\frac{1}{2}\left({h_i}^2 + h_{i-1}^2\right)(x_i - x_{i-1})\right] \tag{4-2a}$$

$$h_{\mathrm{rms}}'^2 = \frac{1}{L\left(\frac{N-1}{N}\right)}\sum_{i=3}^{N}\left[\frac{1}{2}\left(\left(\frac{h_i - h_{i-1}}{x_i - x_{i-1}}\right)^2 + \left(\frac{h_{i-1} - h_{i-2}}{x_{i-1} - x_{i-2}}\right)^2\right)(x_i - x_{i-1})\right] \tag{4-2b}$$

$$h_{\mathrm{rms}}''^2 = \frac{1}{L\left(\frac{N-2}{N}\right)}\sum_{i=4}^{N}\left[\frac{1}{2}\left(\left(\frac{\frac{h_i - h_{i-1}}{x_i - x_{i-1}} - \frac{h_{i-1} - h_{i-2}}{x_{i-1} - x_{i-2}}}{(x_i - x_{i-2})/2}\right)^2 + \left(\frac{\frac{h_{i-1} - h_{i-2}}{x_{i-1} - x_{i-2}} - \frac{h_{i-2} - h_{i-3}}{x_{i-2} - x_{i-3}}}{(x_{i-1} - x_{i-3})/2}\right)^2\right)(x_{i-1} - x_{i-2})\right] \tag{4-2c}$$

where N measurements were made over a scan size L, and the i^{th} measurement of height h_i was measured at horizontal position x_i.

We compute the ratio of full surface area A_{surf} to projected area A_{proj} from a line scan $h(x)$ of length L_x by assuming isotropic surfaces. The equations to do so are derived in the Supplemental Materials for Ref.[47] , but the final result is as follows:

$$\frac{A_{\mathrm{surf}}}{A_{\mathrm{proj}}} \approx \frac{\sqrt{\pi}}{h'_{\mathrm{rms}} L_x}\int_0^{L_x}\left|\frac{\partial h}{\partial x}\right|\sqrt{1 + \left(\frac{\partial h}{\partial x}\right)^2}\,dx \text{ for } h'_{\mathrm{rms}} > 0.2 \tag{4-3a}$$

$$\frac{A_{\text{surf}}}{A_{\text{proj}}} \approx 1 + \frac{1}{2} h'^{2}_{\text{rms}} \text{ for } h'_{\text{rms}} < 0.2 \qquad \text{4-3b}$$

The second Eq. (4-3b) represents the traditional approximation[34] for the limit of small RMS slope h'_{rms}.

4.1.3 Combining TEM, AFM, and Profilometry

The first key outcome from this investigation is the measurement of commonly used roughness parameters (Eq. 4-2) at the smallest length scales. Across all techniques, the individual measurements of RMS height, RMS slope, and RMS curvature vary by orders of magnitude with size scale, as shown in Fig. 6 a-c. For example, the magnitude of the RMS slope – a critical parameter in numerical and analytical models[14–16] of rough-surface properties – varies by more than two orders of magnitude as a function of yardstick size (pixel size) *l*. At the largest scale, the stylus profilometer measured an average RMS slope of 0.03, corresponding to an angle of just 1.7°, reflecting the fact that the UNCD has the appearance equivalent to a polished silicon wafer (see Fig. 2a)[47]. At the smallest scales that are accessible by conventional techniques, the AFM data showed an average RMS slope of 0.27 (15° from horizontal)[47], in rough agreement with prior measurements on related films.[51] However, the novel TEM measurements showed an average value of RMS slope equal to 0.92 (43° from horizontal), more than triple the AFM-measured value.[47] For comparison, the mean surface slope of the UNCD, when measured with high resolution, exceeds the average RMS slope of the Austrian Alps (0.8) when measured with a yardstick on the order of a human step length.[52] The RMS curvature (Fig. 6c) showed yet a greater influence of measurement parameters, with five orders of magnitude in difference between the

smallest and largest values measured. Likewise, the true surface area (the most analogous parameter to Mandelbrot's coastline length) showed significant variation (Fig. 6d). While the stylus data suggested a roughness-induced increase in surface area of just 0.1% above the projected area, the TEM data demonstrated that the true surface area is approximately double the projected value.[47] Taken together, the variation in these measurements conclusively demonstrate the impossibility of linking any single scalar measurement of topography to a functional property, and suggest a primary cause of the inconclusive results that are widely reported in roughness literature (for example, Ref. [10]).

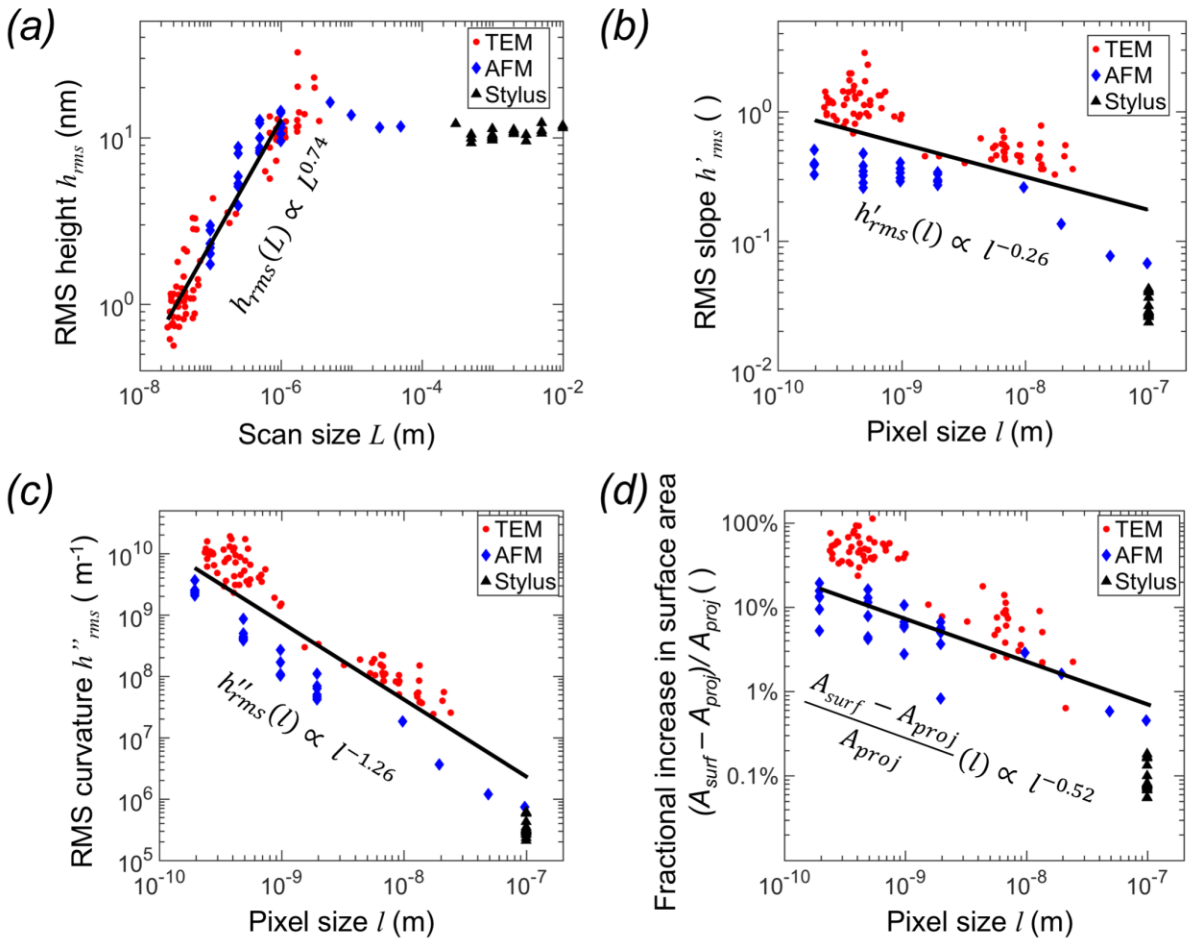

Figure 6 Measurements of scalar roughness parameters show variation by orders of magnitude both within and between experimental techniques. The RMS height (a) varies by more than an order of magnitude depending on how it is measured. Here, the RMS height is presented as a function of scan size, because the largest features have the most significant effect. The solid line shows the best-fit power-law exponent, which corresponds to the Hurst exponent in the variable-bandwidth model (see main text); this value is used to predict the scaling behavior of the other roughness parameters (b-d, solid lines). The RMS slope (b), RMS curvature (c), and computed fractional increase in surface area (d) all show systematic variation by at least two orders of magnitude with measurement size. These parameters are presented as a function of pixel size because the smallest-size features have the most significant effect. Images (a), (b), (c) and (d) reproduced from Ref.[47], copyright American Chemical Society, 2018.

More quantitatively, the scalar roughness parameters can be analyzed as a function of measurement size. Results are analyzed in the style of the variable-bandwidth method (VBM).[53,54] For a self-affine surface, measured values of h_{rms} should scale with scan size L according to $h_{\mathrm{rms}}(L) \propto L^{H}$, where H is the Hurst exponent.[53] Since measurements were taken at a wide range of scan sizes, this sets the upper limit of wavevector for each calculation. For this analysis, we therefore do not need to numerically restrict the bandwidth of our measurements,[53] but rather rely on their natural bandwidths. The individual measurements of RMS height $h_{\mathrm{rms}}(L)$ (Fig 6a) demonstrate power-law scaling corresponding with a Hurst exponent of $H = 0.74 \pm 0.05$ at small L and a crossover to a plateau at approximately L = 1 μm.[47] The RMS slope and RMS curvature of a self-affine surface are predicted[6,17] to scale as: $h'_{\mathrm{rms}}(l) \propto l^{H-1}$ and $h''_{\mathrm{rms}}(l) \propto l^{H-2}$, but these trends had not previously been demonstrated experimentally. These results demonstrate this scaling behavior of these parameters and show that it is in reasonable agreement with the expected behavior for H = 0.74 (extracted from Fig. 6a). The plateau at 1 μm does not appear in Figs. 9b-d because the pixel size of all measurements is below this scale. The fractional increase in surface area for a self-affine surface should scale[47] as $\left(A_{\mathrm{surf}} - A_{\mathrm{proj}}\right)/A_{\mathrm{proj}} \propto l^{2H-2}$; Fig. 6d presents the data in this form. While it has been shown that roughness parameters vary with scan size, this investigation demonstrates the functional form of the scaling for RMS slope, RMS curvature, and true surface area. Further, the TEM measurements enable the calculation of parameters at the very smallest scales.

The second key outcome from this investigation is the calculation of true, scale-invariant roughness parameters. As mentioned, analytical and numerical models[4,6–8,13–16] suggest that adhesion, friction, and contact stiffness depend on the true RMS height, RMS slope, and RMS curvature of the surface. However, Fig. 6 demonstrated the variability of any individual

measurement of these parameters. To overcome this paradox, we combine all of the present measurements, spanning eight orders of magnitude in size scale, together into one complete description of the surface. The power spectral density is used as the tool for combining these multi-scale measurements into a single description. Figure 7 shows the computed PSDs from all measurements, with unreliable data not included. The 127 individual measurements, taken at more than 30 different magnifications using three different instruments, collapse onto a single curve.[47] Only three measurements, taken with the same AFM probe, showed deviation (cyan data in Fig. 7) and these are attributed to tip-size artifacts (Fig. 2e). The arithmetic average of all measurements comprises a single function that fully describes the topography for the UNCD surface.

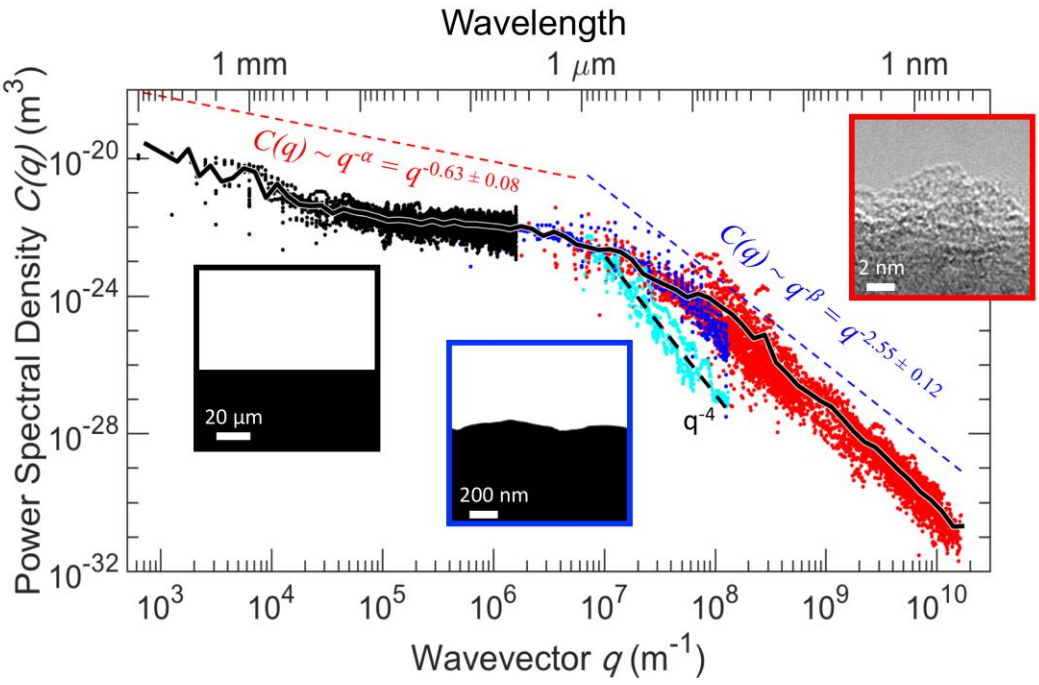

Figure 7 Topography measurements across eight orders of magnitude in length scale are combined into a single description of the surface. The power spectral densities of all 127 measurements at various resolutions were combined into a single plot. The reliable portions of line-scan measurements from stylus (black), AFM (blue), and TEM (red) are shown as points. The cyan data is affected by tip-size artifacts (see main text). Representative side-view images are shown at 1-to-1 scaling in the insets, which are outlined in the corresponding color. The individual measurements are combined into a single PSD (black line with white outline), which represents a comprehensive description of surface topography. The curve can be approximately fit using power-law scaling relations (colored dashed lines). However, having an experimental measurement of the full multi-resolution PSD curve eliminates the need for assumptions about self-affinity. Reproduced from Ref.[47], copyright American Chemical Society, 2018.

The curve shows a power-law with exponent $\alpha = 0.63$ at small q (long wavelengths) and $\beta = 2.55$ at large q (short wavelengths).[47] The exponents α and β extracted from the multi-resolution PSD therefore characterize the long wavelength and short wavelength behavior of the UNCD surface, respectively. The cutoff between large and small q is somewhat arbitrary; here is has been chosen as 1 μm, in accordance with Fig. 6a. We note that these exponents are consistent with a data series generated according to fractional Gaussian noise,[55–57] where the Hurst exponent H characterizes the asymptotic decay of the correlation at large time scales while the short-time behavior is characterized by the fractal dimension D.[57,58] For self-affine processes, both quantities are related to each other[57,59] by $D + H = n + 1 = 2$ where n is the dimension of space. ($n = 1$ for our line scans.) For fractional Gaussian noise, the Hurst exponent can be extracted as $H = (\alpha + 1)/2$ and the fractal dimension can be extracted as $D = (2n + 3 - \beta)/2 = (5 - \beta)/2$.[57,58] Using the values of α and β quoted above, this yields $H = 0.82 \pm 0.04$ and $D = 1.23 \pm 0.06$. Since $D + H \approx 2$. We can convert the fractal dimension into an equivalent Hurst exponent using $H_D = 2 - D = (\beta - 1)/2 = 0.77 \pm 0.06$.[47] This value agrees well with the value of 0.74 ± 0.05 extracted using the VBM, although numerical simulations[53,60] have shown that fitting Hurst exponents to power-laws can lead to a systematic error of up to 0.2 with the method of calculation. We note that at present it is unclear to us why fractional Gaussian noise seems to serve as a good model for our spectral densities, but it indicates that the topography of the long-wavelength region, typically denoted as the "roll-off",[6] has the statistical structure of the derivative of the short-wavelength region and hence $\alpha = \beta - 2$.

The measured values of H are consistent with many experimental observations on scales from mountain ranges[61] to atoms[62] and processes such as fracture[63–65] and plastic deformation[66]. A value of $H > 0.5$ indicates persistent behavior of the spatial correlations, *i.e.*, a high value is

likely to be followed by another high value. We note that our UNCD films are grown on a surface and that common growth models (*e.g.*, Edwards-Wilkinson[67] or Kardar-Parisi-Zhang[68]) predict $H = 0.5$, but $H > 0.5$ is commonly observed in deposition from vapor[69] or liquid[70]. Finally, we note that the curve is not completely linear in either the low- or high-q region, and therefore the exact value of the scaling exponent will depend on the size-scale over which it is measured. For example, if a line is fit to only the highest-q region of the curve ($q>10^8$), then the values shift to $D = 1.0 \pm 0.04$ and $H_D = 1.0 \pm 0.04$.[47] In general, to eliminate this uncertainty in how the curve is fit, the following paragraph discusses the use of the entire PSD curve (without assumptions of self-affinity) to compute scale-independent parameters.

This combined data from all measurements was used to compute scale-independent values of h_{rms}, h'_{rms}, and h''_{rms}, which describe the underlying surface. These roughness parameters are equal to the zeroth, second, and fourth moments of the PSD, respectively[17]. For a one-dimensional PSD, these parameters are computed as follows:

$$(h_{\mathrm{rms}})^2 = \frac{1}{\pi}\int_0^\infty C(q)dq,\ (h'_{\mathrm{rms}})^2 = \frac{1}{\pi}\int_0^\infty q^2\, C(q)dq,\ (h''_{\mathrm{rms}})^2 = \frac{1}{\pi}\int_0^\infty q^4\, C(q)dq \qquad 4\text{-}4$$

These integrations were performed numerically using the trapezoidal method, eliminating the need for assumptions about self-affinity. The bounds of integration are defined by the largest measured scan size (1 cm) and the smallest pixel size (4 Å). No smaller-size contribution is expected because this is approaching the atomic scale, beyond which topography is not clearly defined. Using this approach, the computed true values of roughness parameters for the surface were h_{rms} = 17.5±1.3 nm, h'_{rms} = 1.2±0.28 equivalent to an angle of 50°, and h''_{rms} =

$6.3 \times 10^9 \pm 1.2 \times 10^9$ m^{-1}.[47] The uncertainty was computed using standard error propagation as applied to the numerical implementation of Eq. 4. For the h'_{rms} and h''_{rms}, which depend on the finest scales of roughness, these results demonstrate that the novel TEM data yields the most accurate estimate of RMS slope and curvature, with conventional topography techniques erring by an order of magnitude or more.

The combination of techniques across all scales yields even more robust measurements of roughness parameters than can be achieved by any method in isolation, and this combined approach is necessary to achieve a comprehensive and predictive description of a surface.

4.2 Validation of TEM-based Approach.

Since, a novel technique was developed to measure TEM topography, there is a need to check whether the surface is preserved and what is the effect of different techniques. To investigate that we measured and extracted using 168 different TEM measurements of the UNCD film at various locations and magnifications.[22] The characterized UNCD samples fell into three types: (1) samples created using the *surface-preserving cross-section technique,* where the adhesive had only just been removed (Fig. 8a); (2) samples created using the *surface-preserving cross-section technique,* but where the adhesive that glued the samples together was extremely thin but still covered the surface (Fig. 8b); and (3) samples created using the *wedge deposition technique*.

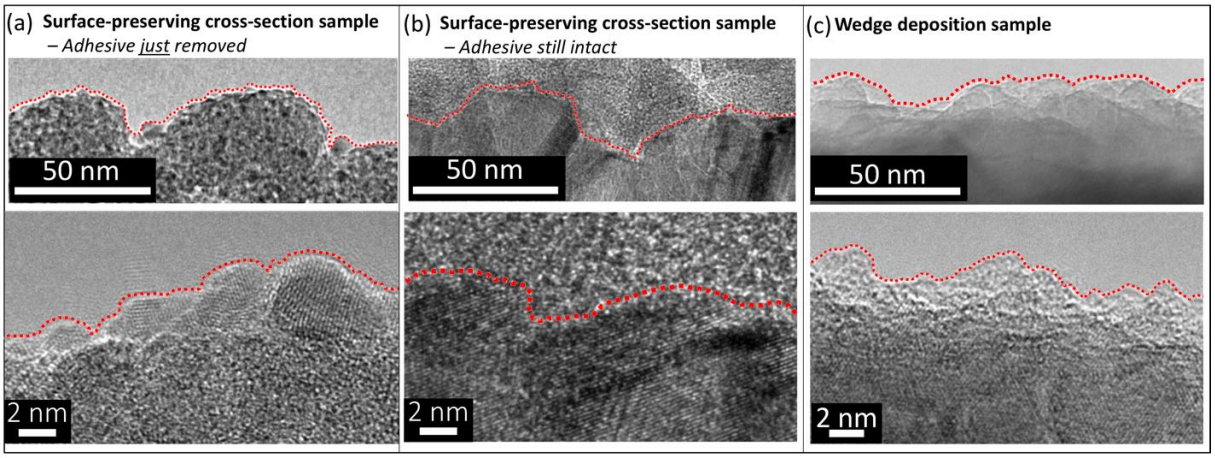

Figure 8 Using both sample preparation approaches, the topography can be directly extracted using the contrast in the TEM images. TEM images were captured at low magnification (top row) and at high resolution (bottom row). Line contours of the topography of the free surface were extracted using algorithms to trace the boundary of the material when viewed in profile. As discussed in the main text, samples were prepared using surface-preserving cross-section sample preparation (a-b), and by depositing material on a premade electron-transparent substrate (c). For the surface-preserving cross-section samples, the material was imaged both in regions where the adhesive was *only just* removed (a) and also in regions where the adhesive was still intact and covering the sample (b). Both conditions ensure minimal exposure of the free surface to the ion beam and therefore minimal modification from its native state. For the regions where the adhesive was still intact (b), the boundary was readily determined as the UNCD has visible atomic lattice and a darker contrast than the amorphous adhesive. Images (a), (b) and (c) reproduced from Ref.[22], copyright Suface Topography: Metrology and Properties, 2018.

4.2.1 Comparing Results Across Different Sample Preparation Techniques

To quantitatively assess and compare results across sample preparation techniques, two types of roughness descriptors were computed: a statistical descriptor in the form of the power spectral density $C(q)$; and scalar roughness descriptors, the root-mean-square height h_{rms}, RMS slope h'_{rms}, and RMS curvature h''_{rms}. The power spectral density was computed according to the best practices described in Refs.[17]. Fig. 9a shows the averaged power spectra for all samples of each preparation. When the data larger than wavelength of 20 nm is fit using a power-law function, the scaling exponents are -2.87 ± 0.08 for the wedge-deposition sample, and -2.85 ± 0.12 and -2.97 ± 0.16 for the cross-section sample (adhesive intact, and adhesive removed, respectively).[22] From this the Hurst exponent of the surface can be calculated (as described in Ref. [47]) as H=0.93 ± 0.04, 0.92 ± 0.06, and 0.98 ± 0.08, respectively.[22] Note that the wedge sample is the same one that was characterized in previous sub-section which used the wedge-deposition method (Section 4.1.3.2). As discussed earlier, the precise value of Hurst exponent that is measured depends on the range of wavevectors over which the fitting is done. The measured Hurst exponents between the different sample preparations are identical within experimental uncertainty. This finding demonstrates that the statistics of the measured surface do not depend on preparation, whether *wedge deposition technique* or *surface-preserving cross-section technique* – and in the latter case, whether the adhesive is left intact or just barely removed. The scalar descriptors were computed from the real-space measurements using Eq. 4-2 and the computed values vary significantly depending on scan size and pixel size as shown previously and in Ref. [47], and therefore must be presented in this context. The RMS height is shown as a function of scan size L in Fig. 9b, because the largest-scale features have the most significant effect. The RMS slope (Fig. 9c) and RMS curvature (Fig. 9d) are presented as a function of pixel size, because these parameters depend most

strongly on the small-size features as discussed previously. In all cases, there is scatter in the data from sample to sample, but at a given scan size there is no consistent trend with the type of sample preparation.[22] The purpose of this investigation is to compare and assess the measured results between different techniques of TEM preparation; for comparison of results against other methods of roughness measurement. In short, the TEM-measured data with AFM measurements on the same material but provides small-scale roughness information that is not accessible using AFM.

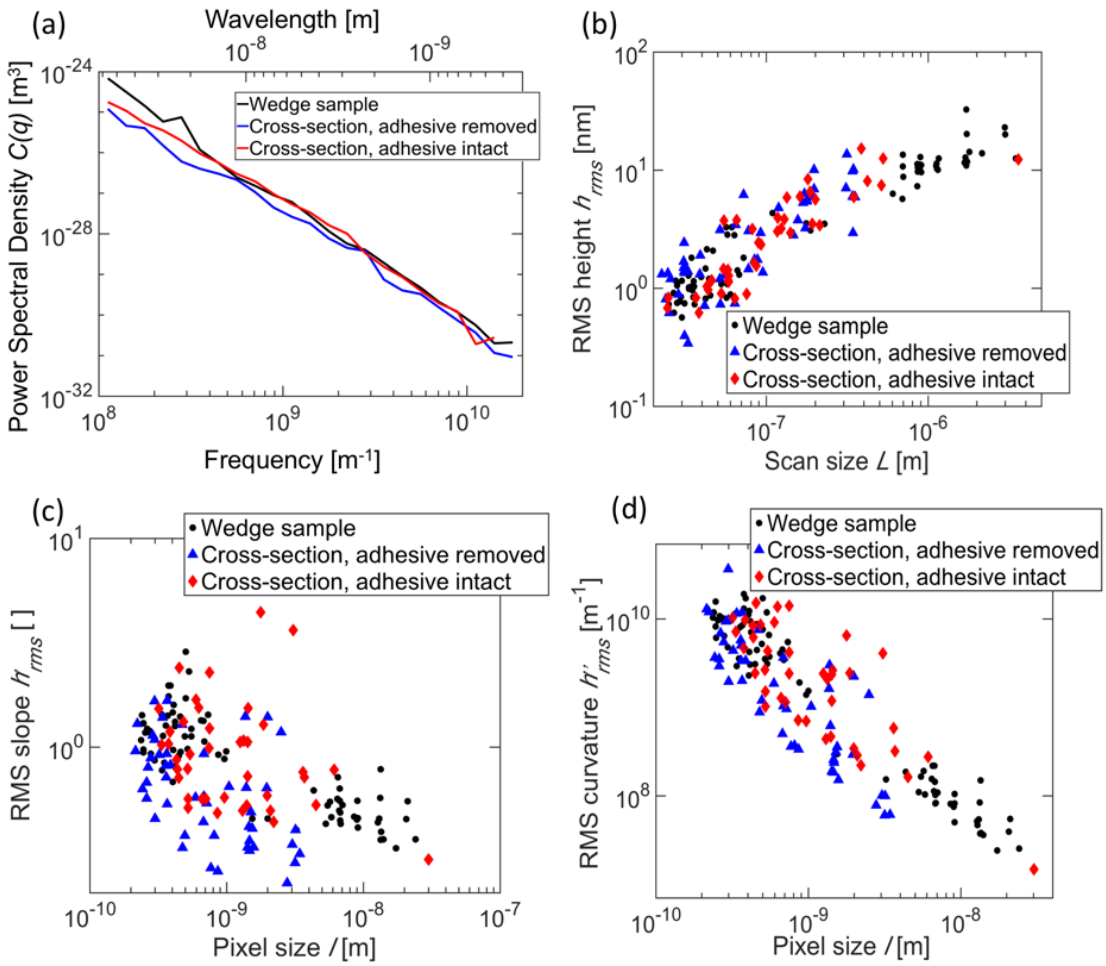

Figure 9 The statistics of roughness are measured at the smallest length scales and are not affected by the method of sample preparation. Roughness statistics were measured from 168 different TEM images, including various locations and various magnifications for each type of sample. The PSD of topography (a) contains a statistical picture of the contributions to roughness from different lateral size scales. Here, an averaged PSD has been stitched together from the individually measured PSDs computed from each image (using the techniques described in Refs. [47]). The PSDs demonstrate that the material can be characterized at scales below $\boldsymbol{\lambda}$ =10 nm (above $\boldsymbol{q} = \boldsymbol{6} \times 10^8$ m^{-1}); these scales are inaccessible using conventional techniques. The root-mean-square height (b), slope (c), and curvature (d) of topography are important scalar descriptors of the surface, which are used in many mechanical models of rough-surface properties. Their values are known to depend on measurement size, and here they are measured at various magnifications, including down to the atomic scale. For all four roughness descriptors, the measurements are indistinguishable across sample preparation techniques. Images (a), (b), (c) and (d) reproduced from Ref.[22], copyright Suface Topography: Metrology and Properties, 2018.

These results imply that both of the sample preparation approaches for sample preparation are equally valid for topography examination. For bulk materials, there is no choice except to use the more time-consuming cross-section preparation. However, for deposited materials (including many technologically relevant materials, such as films and coatings) the wedge-deposition method represents an easier way for topography evaluation. This technique can be used quite broadly in materials deposition, simply by including an electron transparent wedge as a witness chip that is co-deposited with any other material of interest. After deposition, the topography of the witness chip can be straightforwardly evaluated in the TEM to represent the topography of the flat sample.

4.2.2 Quantitative Measurement of Thickness for Cross-section and Wedge Samples Using Electron Energy Loss Spectroscopy (EELS)

In addition to imaging the sample and extracting its topography, as described above, it is often useful to understand the thickness of the measured sample. This can be readily done in TEM using EELS, which were performed in this investigation using dark-field STEM operating at 200 kV. The thickness of a sample can be measured by measuring the fraction of electrons that are inelastically scattered by the sample[27]. For a thicker sample, the electrons pass through more atoms and more electron clouds and have a higher likelihood of knocking out a valance or core shell electron from the sample. The thickness *t* can be determined from the EELS spectrum using the following expression[71,72]:

$$t/\lambda = \frac{\ln(I_{tot})}{\ln(I_0)} \qquad 4\text{-}5$$

where I_0 is the intensity (integrated number of detector counts) associated with the zero-loss peak, I_{tot} is the intensity of all collected electrons, and λ is the total inelastic mean free path for all inelastic scattering. Because the UNCD is primarily composed of sp3 carbon[43], the λ for carbon in diamond cubic structure was used, which is 112 nm [72].

4.2.3 Investigation into the Effect of Thickness on Experimental Results

It seems possible that the thickness of a TEM sample will have a strong effect on the measured topography, because samples with different thicknesses may cause different features to contribute to the observed surface profile. Therefore, in this study, the effect of thickness was directly investigated using the analytical capabilities of the TEM. For each location where topography was measured, as shown in Fig. 10a, electron energy loss spectroscopy (EELS) data was collected (Fig. 10b). The thickness at each of these locations was determined using Eq. 4-5. The thicknesses varied between samples from 28 nm to 150 nm for the cross-section samples; for the wedge samples, the thickness at the surface varied from 14 nm to 59 nm, and because of the rounded apex of the wedge, the thickness increased rapidly with depth into the material.[22] By 10 nm below the surface, the through-thickness was between 80 and 120 nm.[22] Figure 10(c, d) directly present the PSD and RMS height as a function of sample thickness. The PSD is completely indistinguishable between all samples, regardless of thickness. The computed RMS height does show variation between samples but exhibits no systematic effect of thickness. Because it is only the outermost contour of the UNCD that contributes to the measured profile (red line in Fig. 10 a), and because the method of preparation of the sample does not affect the measured statistics, then it seems unlikely that other parameters of the sample preparation will have a strong influence on the final result. For instance, factors such as the precise angle of the ion milling of the cross-section

sample, or the thickness of the thin film in the wedge-deposition sample (which determines the radius of curvature of the outermost edge), seem unlikely to affect the measurements. This assumption is specifically tested in the following sub-section by systematically varying the radius of curvature of a simulated rough surface. Overall, the results demonstrate for UNCD that the measured statistics describing the surface roughness of these specially prepared TEM samples have no dependence on the type of preparation used, nor the final thickness of the sample.

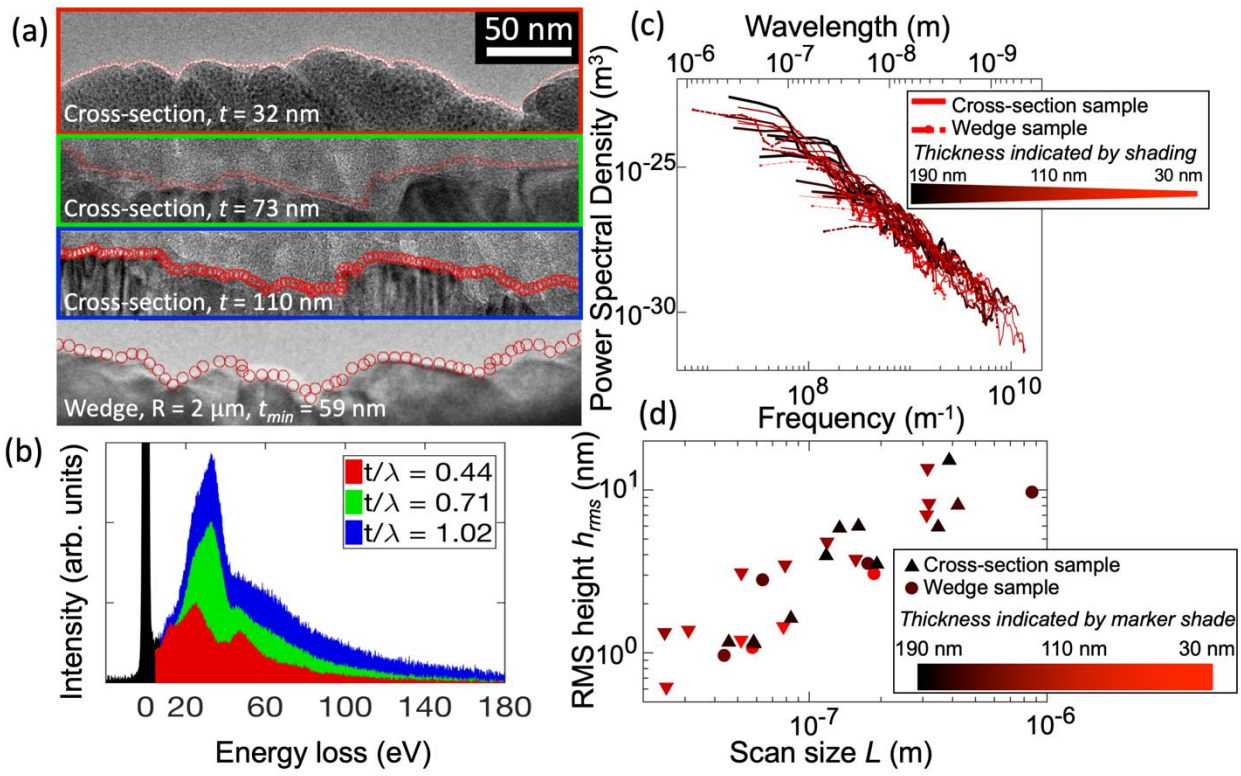

Figure 10 Direct measurements of thickness using analytical TEM demonstrate no systematic effect of thickness on results. Using electron energy loss spectroscopy (EELS), the thickness was measured (see main text) for a subset of the profiles from Fig. 6. Four representative profiles are shown (a), from cross-sections (with and without adhesive removal) and from a wedge-type sample. The corresponding EELS spectra for the cross-section samples (b) show the intensity as a function of energy loss, and the ratio of zero-loss intensity (black region) to total intensity (sum of black and colored areas) yields a measure of thickness. Plots of PSD (c) and RMS height (d) show random variation within the measurements but show no systematic trend with increasing thickness. Plots of RMS slope and curvature (not shown) show a similar lack of dependence on thickness. Images (a), (b), (c) and (d) reproduced from Ref.[22], copyright Suface Topography: Metrology and Properties, 2018.

4.2.4 Measuring the Effect of Thickness Using Artificial Surfaces

While the experimental trends are robust, the samples size is not as large as it would ideally be to draw firm conclusions. To more systematically evaluate the effect of thickness on measured results, artificial (computer-generated) self-affine surfaces were created and evaluated. First, an artificial random, self-affine surface using a Fourier filtering algorithm was created, described *e.g.*, in Refs. [17,73]. The surface has a resolution of 4000 x 4000 pixels spanning a size of 400 nm x 400 nm. It is self-affine across all scales with a Hurst exponent of H=0.8. The surface was created such that its rms slope is unity, $h_{rms}' = 1$.[22]

Two types of TEM-analogous profiles were created and analyzed. First, to approximate the cross-section samples, long strips of thickness t were extracted from the overall surface, as shown schematically in Fig. 11a. A TEM-analogous side-view profile was constructed as the lateral projection of this strip. More specifically, the maximum height found at each horizontal position was taken as the height of the emulated TEM profile (Fig. 11b). Second, to approximate the wedge-deposited samples, a similar approach was used but with the superposition of a radius R of curvature along the through-thickness direction, as shown in Fig. 11e. The resulting profiles for different strip thicknesses and different wedge radii are shown in Fig. 11b and 11f, respectively. Finally, the power spectral densities of the various profiles were computed (Fig. 11c and 11g) and demonstrate no variation with thickness.

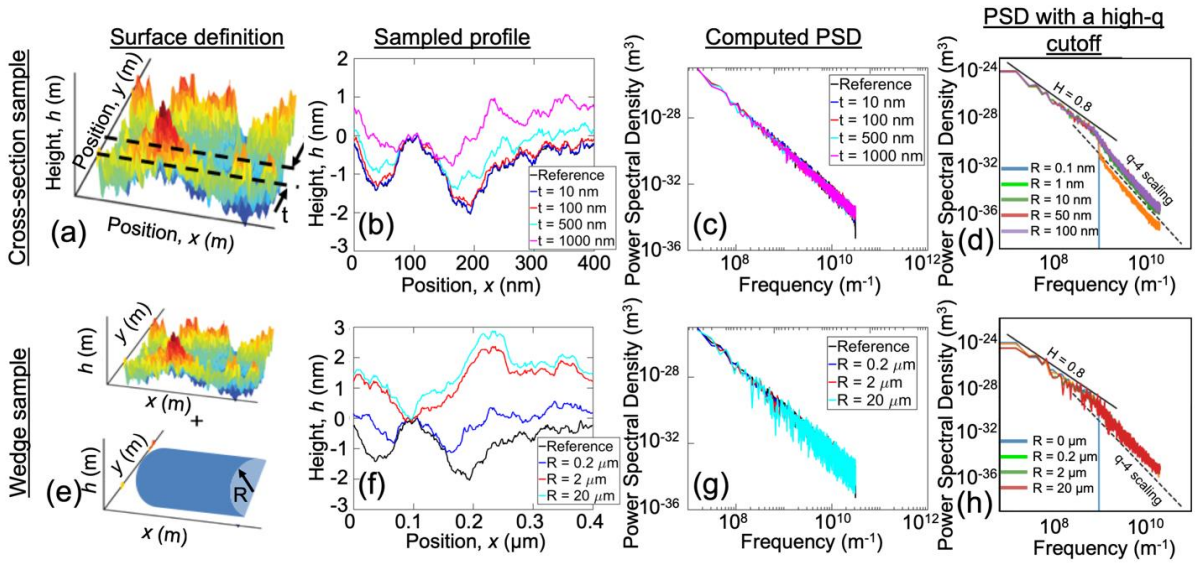

Figure 11 Measuring the effect of thickness on the statistics of roughness for artificially-created surfaces. A random self-affine surface was computer-generated and sectioned to a desired thickness (a). This process was repeated to create line contours (b) with variable thickness *t*. For self-affine surfaces, the computed power spectral densities (c) were shown to be completely independent of thickness of the profile. When a minimum wavelength of roughness was introduced (see main text) at 5 nm ($q = 1.26\ nm^{-1}$), then the thicker samples do show an effect, manifesting as q^{-4} scaling behavior, which was never observed experimentally. The process was repeated (e-h) to simulate the wedge-deposited surfaces. For various values of cylinder radius *R*, the results were the same as the cross-section simulations. Images (a), (b), (c), (d), (e), (f), (g) and (h) reproduced from Ref.[22], copyright Suface Topography: Metrology and Properties, 2018.

As demonstrated in the profile images of Fig. 11(b, f), there are certainly change in the particular surface features that contribute to the sampled profile, but because the newly-appearing surface features have the same statistical character as the disappearing surface features, there is no net change in the statistical character of the measured surface.[22] It is noted that these findings are in contrast to the results obtained for surfaces with Gaussian or exponential height-height correlations investigated in Ref. [25].

To further investigate the difference from earlier models, a characteristic length-scale was introduced to the simulated profiles in the form of either a short-wavelength cut-off or a long-wavelength roll-off. The short-wavelength cut-off means that there is no contribution to overall roughness from wavelengths smaller than a certain size, and the profile will be smoothly varying if examined at smaller size-scales. As shown in Fig. 11d, h, this introduces a spurious contribution to the PSD that scales as q^{-4} (corresponding an apparent Hurst exponent of 1.5), similar to the effect of tip radius in atomic force microscopy images [17,48]. However, such a transition was not observed in any of the experimental data. Instead, the PSD is observed to be approximately self-affine all the way to the highest measurable q. Additionally, the real-space images clearly show Ångstrom-scale variations in roughness that contradict the idea of a length scale at which the profile becomes smooth.

4.2.5 Combining Insights from Experimental and Simulation Results

The experimental and simulation measurements taken together demonstrate that the thickness and preparation of the sample does not affect the measured statistics of roughness. From a practical perspective, there will be two maximum thresholds of thickness that should be considered. First, the maximum thickness of the sample is bound by the need for electron

transparency in the TEM. The inelastic mean free path of an electron depends on the material it is passing through and, for example, is several times larger for carbon than it is for heavy elements like gold.[27] Therefore, the thickness of the measured portion of the sample (red lines in Fig. 5) should be comparable to the length of the mean free path in that material. Fortunately, a violation of this condition is easily observed in the TEM as a significant reduction in resolution in the region of interest. This can be remedied by further thinning in the ion mill (for the cross-section method) or by deposition of a thinner film of material (for the wedge-deposition method). Second, if the material itself shows "roll-off" behavior (where the PSD is flat below some critical value of q (*i.e.*, above some critical length scale $\lambda_{roll\text{-}off}$)), then the thickness of the sample should be less than $\lambda_{roll\text{-}off.}$ If the thickness is larger than $\lambda_{roll\text{-}off}$, there will be a reduction in the magnitude of the measured PSD. However, in our experience and that of several other authors (e.g. Ref. [62]), the roll-off region of most real surfaces begins at in the range of 1-100 μm – a larger thickness than is practical for use in the TEM. Furthermore, it should be noted that the roll-off behavior was still adequately detected at larger thicknesses, just with a reduced magnitude of the PSD at smaller q. Therefore, the TEM data can be paired with atomic force microscopy data, which will more accurately characterize the larger-scale topography (see, for example, Ref. [47]). Overall, in the vast majority of real-world materials, the described methods will enable the accurate measurement of roughness statistics with no significant effect of sample thickness.

4.3 Conclusions from Objective 1

By characterizing a surface across eight orders of magnitude in size scale, this investigation demonstrates two key advancements in our understanding of surface topography. First, while individual measurements of such critical roughness parameters as RMS slope and RMS curvature will vary by orders of magnitude between and within different experimental techniques, TEM-based measurements are able to approximate the true values for the surface by capturing the smallest-scale topography. For a smooth, conformal UNCD film, the measured value of RMS slope is of order unity and the value of RMS curvature corresponds to Ångström-scale radii; these are significantly larger than those that have been measured previously with conventional techniques.[47] Second, we demonstrate the combination of topography measurements across all size scales to compute true, scale-independent parameters for the underlying surface. By using the power spectral density, we show that the more than 127 individual measurements collapse to a single curve. The resulting curve is approximately self-affine with different scaling exponents in the short- and long-wavelength regions. We show that the Hurst exponent can be computed independently from both regions, indicating that the long-wavelength portion of the PSD (which is often discarded in topography investigations as a "roll-off" regime) also carries information on the self-affine nature of the surface.[47] We further show that, instead of relying on self-affine approximations, one can use the combined multi-resolution PSD curve to compute scalar roughness parameters for the surface: RMS height, RMS slope, RMS curvature, and also the roughness-induced increase in true surface area.[47] In summary, while the values of the PSD and roughness parameters are unique to the measured material (unpolished UNCD), the present approach to characterization and analysis is widely generalizable to many materials. The demonstrated approach enables more accurate evaluation of surface topography of real-world

components, and more meaningful correlation with surface properties. Further, it allows the systematic testing of the many existing analytical and numerical models, in order to uncover the physical links between surface topography and surface function.

Finally, the use of transmission electron microscopy to obtain the critical small-scale topography characterization that is inaccessible using conventional techniques. Two separate sample preparation techniques are presented including the preparation of a surface-preserving cross-section and the deposition of a thin-film material onto a pre-fabricated TEM substrate. The latter technique is rapid and straightforward enough for inclusion in standard deposition techniques used for semiconductors or devices.[22] To validate these methods, both techniques were applied to the same UNCD film to extract line contours which were used to calculate statistical roughness parameters. Both techniques were demonstrated to yield equally reliable statistics, and the thickness of the prepared sample was shown to have no consistent effect on measured results.[22] For confirmation, mathematical simulation was used to create analogous samples of self-affine, randomly rough surfaces. The simulations yielded nearly identical outcomes and demonstrated an explanation for the lack of dependence on thickness: increasing the sample thickness changes the particular features that are sampled, but not the statistical character of those features.[22]

*Note - Portions of the text have been taken (with or without modification) from my publications:

1. Gujrati, A.*; Khanal, S. R.*; Pastewka, L.; Jacobs, T. D. B. Combining TEM, AFM, and Profilometry for Quantitative Topography Characterization Across All Scales. *ACS Appl. Mater. Interfaces* **2018**, *10* (34), 29169–29178. © American Chemical Society, 2018.
2. Khanal, S. R.; Gujrati, A.; Vishnubhotla, S. B.; Nowakowski, P.; Bonifacio, C.; Pastewka, L.; Jacobs, T. D. B. Characterizing Small-Scale Topography Using Transmission Electron Microscopy. *Surf. Topogr. Metrol. Prop.* **2018**, *6* (4), 45004. © Surface Topography: Metrology and Properties, 2018.

5.0 Results and Discussions for Objective 2: Measuring a Comprehensive, Multi-resolution Description of a Technologically Relevant Surface

Nanodiamond surfaces can be used as industrial material whose properties and performance characteristics can be characterized and reproduced. In general nanodiamond thin films are smooth enough to exhibit low friction in most applications, but they have a very small grain size, thus as one keeps going smaller in scan size the roughness keeps increasing, so for our investigation Though we employ four different diamond films (Polished UNCD, UNCD, NCD and MCD) we started our investigation with only UNCD and it serves as model surface here and all the techniques used and investigated here will then be employed to other diamond films to characterize them similarly.

5.1 Multi-scale Topography Measurement

The stylus profilometry and atomic force microscopy (AFM) data reveal the large- and medium-scale topography, respectively, as shown in Figs. 12 and 13. In both cases, the tip radius is measured in order to compute a "reliability cutoff,"[17] above which tip artifacts are expected to dominate the PSD[48]. The stylus tip is imaged in the SEM, and a circle was inscribed on the tip apex to determine its radius (Fig. 12c); the AFM tips are imaged and analyzed in a TEM (Fig. 13c). Nine stylus scans were taken per material, with scan sizes from 0.5 to 5 mm. A total of 11 AFM scans were performed on each material with sizes from 100 nm to 5 μm. The wear of the AFM tip was minimized using the best practices described in Ref.[74].

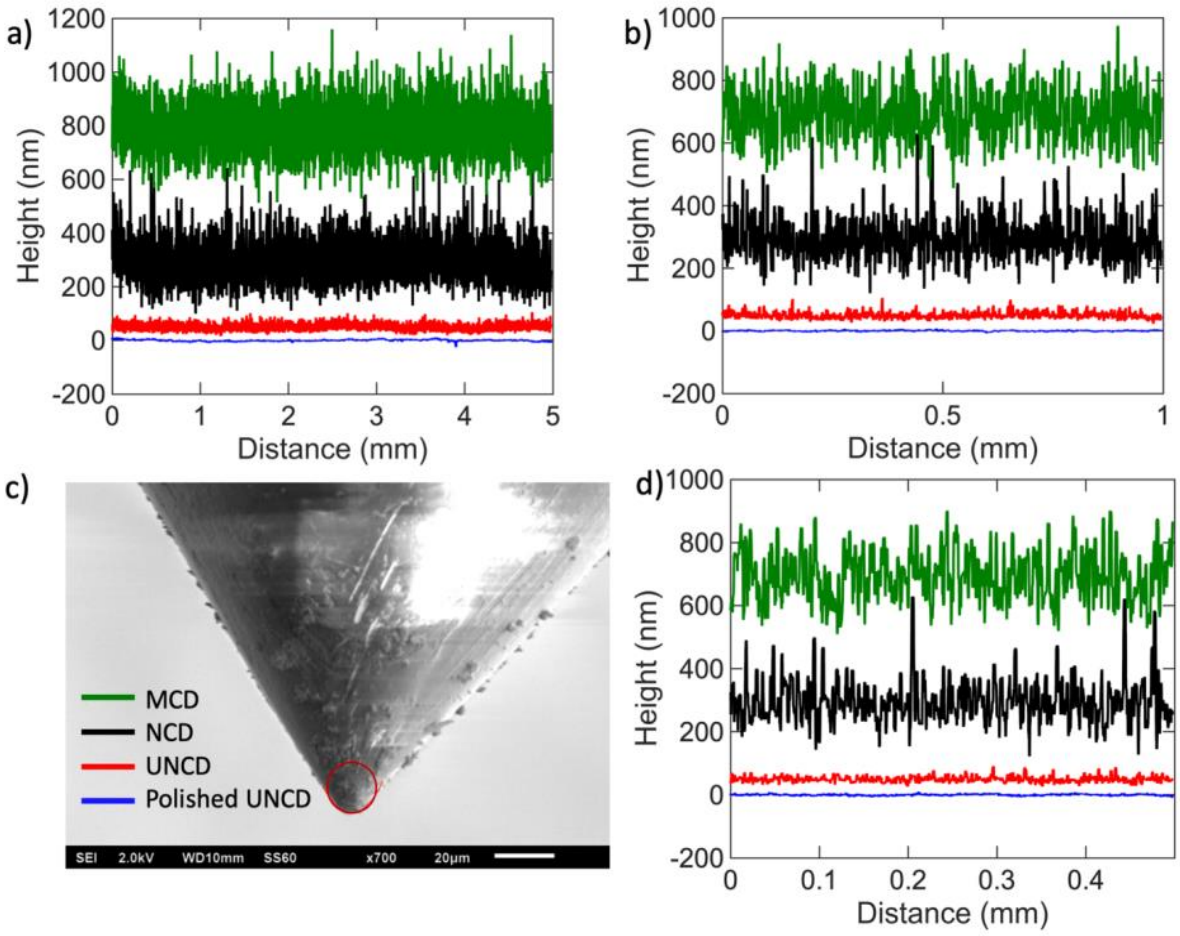

Figure 12 Large-scale topography was characterized using stylus profilometry. Lines scans were collected at three different scan sizes: 5 mm (a), 1 mm (b), and 0.5 mm (c). Throughout this paper, green data represents MCD, black for NCD, red for UNCD, and blue for Polished UNCD. The stylus tip is imaged using a scanning electron microscope (d), so that the measured radius can be used to compute the reliability cut-off of the stylus data.

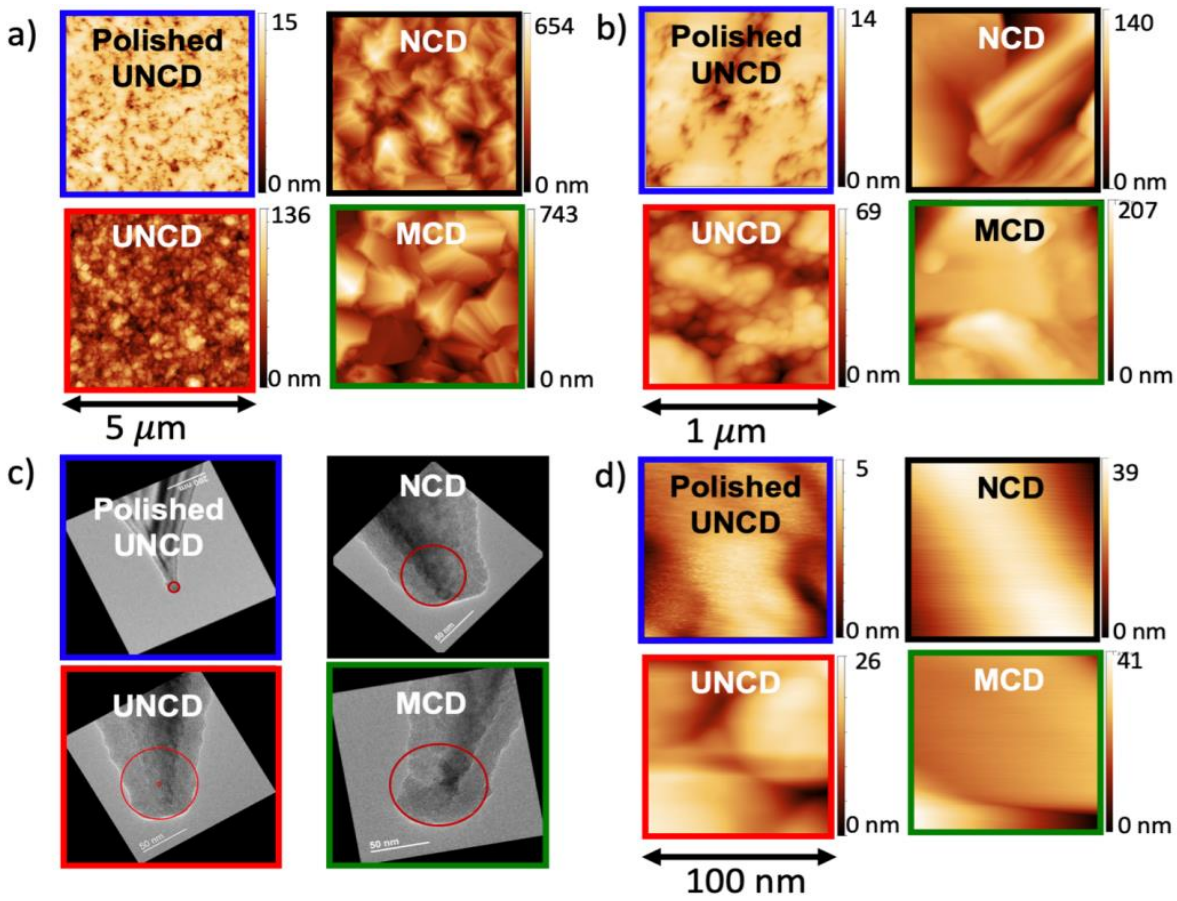

Figure 13 Medium-scale topography was characterized using atomic force microscopy. Square scans were collected with sizes of 5 μm (a), 1 μm (b), and 100 nm (c). However, the one-dimensional power spectral density was computed from each line scan separately, and then averaged for all lines of the square scan. The AFM tips were imaged using a TEM (d), to measure tip radius.

Finally, more than 40 transmission electron microscopy images were collected at various magnifications from 25 kx to 600 kx times, in a variety of locations on each of the surfaces. For the polished UNCD (cross-section samples), the measurements are taken at various locations where the adhesive is just milled out to access virgin surface.[22] For the MCD, NCD and UNCD (wedge sample), the measurements are taken at many different locations on the wedge.

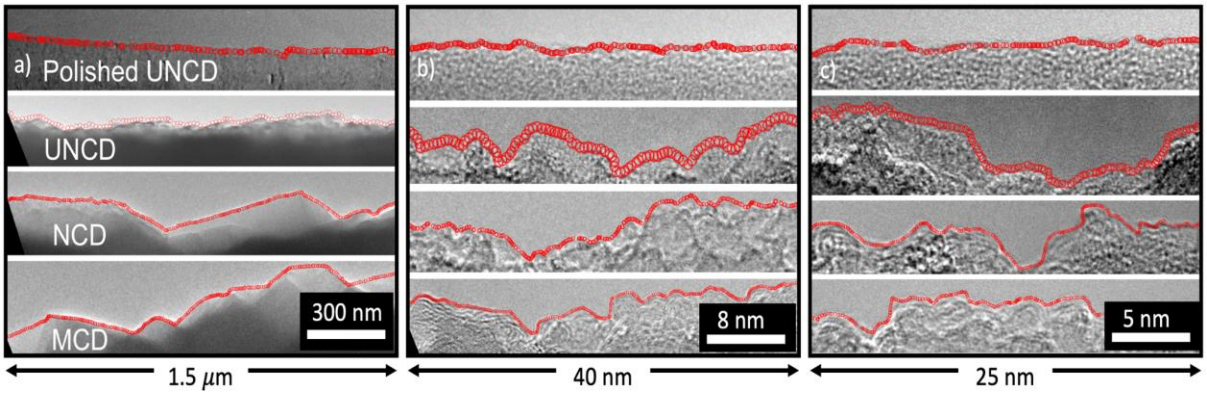

Figure 14 Small-scale topography was characterized using transmission electron microscopy. The top surface was imaged in profile in the TEM at various magnifications, and the surface topography was measured by digitizing the outer contour, shown as red points. While the large grain size of the MCD and NCD is apparent at large scan sizes, these materials have similar small-scale topography as compared the ultrananocrystalline diamond.

5.2 Computing Topography Metrics

In order to understand and predict surface properties, a complete description of topography for each surface is required: this is provided by a single comprehensive PSD that is averaged from all measurements. These comprehensive PSDs are shown in Fig. 15. The artifacted data from each PSD has been identified and removed, then the complete PSD is computed as the arithmetic average of all individual measurements in (logarithmically spaced) bins. There are no fitting

parameters in this analysis; rather the PSD serves to separate the different size scales of topography, and the various techniques agree within experimental uncertainty. These comprehensive PSDs can then be used in analytical and numerical models (such as[4,6–8,13,14,16,75]) to understand and predict surface properties, as was done in Ref.[45].

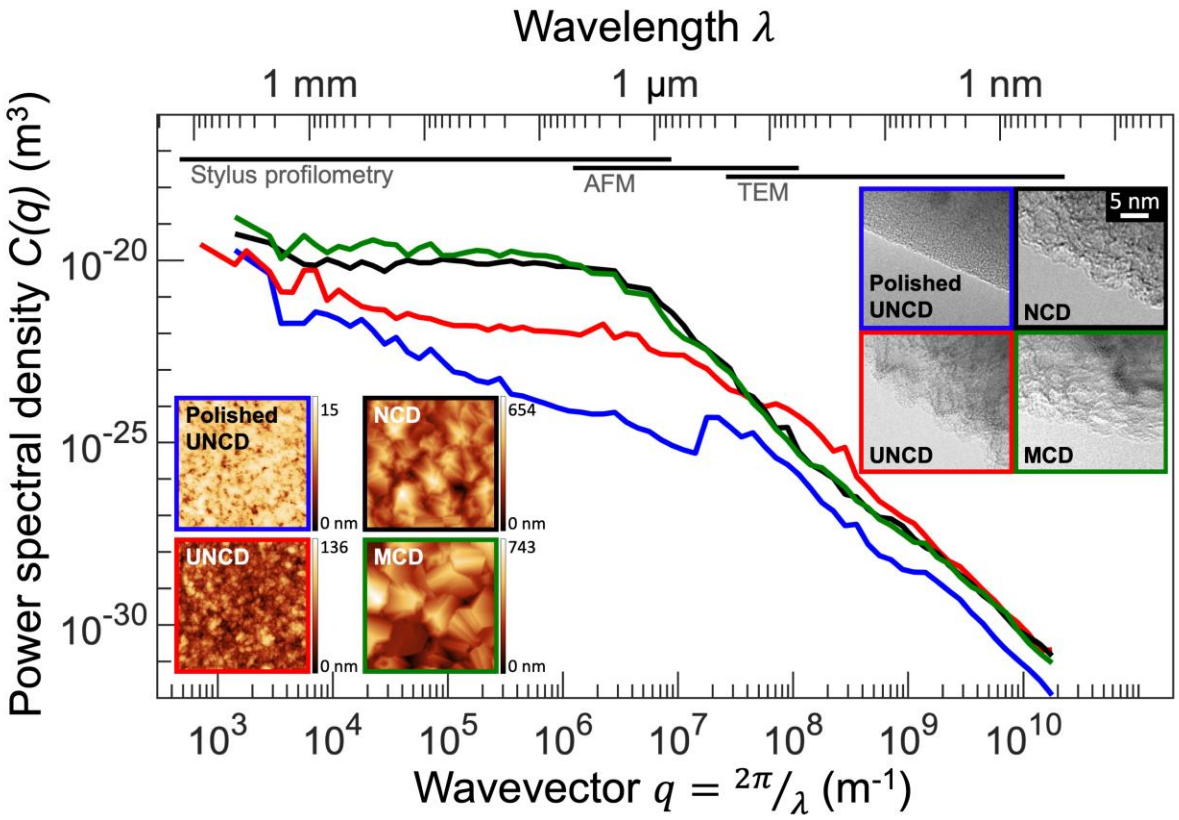

Figure 15 Comprehensive topography characterization for four rough nanodiamond surfaces. The surface topography was measured using a multi-resolution approach that combines transmission electron microscopy (TEM), atomic force microscopy (AFM), and stylus profilometry. Regions of applicability of each technique are indicated with horizontal bars, and are delineated more specifically in Appendix Fig. 1. The nanodiamond surfaces are designated using the following nomenclature: ultrananocrystalline diamond (UNCD) is shown in red; nanocrystalline diamond (NCD) in black; microcrystalline diamond (MCD) in green, and a polished form of UNCD (polished UNCD) in blue. AFM images (of 5-micron lateral size) are shown in the left inset; TEM images are shown in the right inset. More than 50 measurements for each surface are combined using the power spectral density, which reveals the contribution to overall roughness from different length scales (wavelengths). These comprehensive descriptions of surface topography enable the determination of true surface area and stored mechanical energy due to the topography, which are necessary to understand adhesion. Image reproduced from Ref.[45], copyright National Academy of Science, 2019.

If scalar metrics are desired, the full, stitched-together PSD enables the calculation of scale-independent values for RMS height, slope, and curvature. of h_{rms}, h'_{rms}, and h''_{rms}. These are computed using Eq. 4-4 and the values are given in Table 1. Note that, while these may represent the mathematically correct or "true" values of RMS parameters for a surface, any individual application may be sensitive to only a certain range of topography. In that case, the most relevant parameters would be computed by integrating only across the size scales that matter.

Table 1 1D RMS parameters for nanodiamond substrates.

	Polished UNCD	UNCD	NCD	MCD
RMS height	4.2 ± 0.8 nm	17.4 ± 1.3 nm	97.2 ± 11.7 nm	101.2 ± 8.0 nm
RMS slope	0.31 ± 0.03	1.17 ± 0.28	0.92 ± 0.10	0.85 ± 0.10
RMS curvature	1.99 ± 0.35 nm^{-1}	6.32 ± 1.20 nm^{-1}	5.91 ± 1.83 nm^{-1}	5.04 ± 1.45 nm^{-1}

5.3 Evaluating the Meaning of Hurst Exponents

Many real-world surfaces are self-affine[47,61,76]. Self-affinity is characterized by the Hurst exponent *H*: Rescaling a surface of length *L* to λL, and rescaling heights from *h to* $\lambda^H h$ leads to two surfaces that are statistically indistinguishable if the overall surface is self-affine with Hurst exponent *H*. Most commonly, the Hurst exponent is calculated in frequency-space from the power

spectral density. Typically, the PSD is separated (somewhat arbitrarily) into the "self-affine" region, where the topography appears to be described by a power law relationship of $C \propto q^{\beta}$, and the "roll-off" region, where the PSD appears to be flatter. As discussed previously, it is considered here that the 'self-affine' region starts from 1 μm. Accordingly, H is calculated for the 'self-affine region' and H = 0.62 and 0.77 for polished UNCD and UNCD respectively; and H = 0.89 and 0.87 for NCD and MCD respectively. The "roll-off" region and the fractional Gaussian noise (FGN) results in H_{FGN} = 1.10 and 0.82 for polished UNCD and UNCD, respectively; and H_{FGN} = 0.62 and 0.70 for NCD and MCD, respectively.

In comparing and contrasting the various values of Hurst exponent, three observations become apparent. First, previously (section 4.1.3), it was speculated that there may be a connection between H_{FGN} and H (from the self-affine region). This observation would be extremely useful as it suggests that the small-scale behavior could be predicted from large-scale measurements. Unfortunately, when these four different surfaces are compared, there is no clear relationship that emerges. Second, when using the traditional "self-affine" portion of the PSD, a variety of Hurst exponents can be extracted for a single surface. This is particularly true for MCD and NCD: when Hurst exponents were calculated by dividing the "self-affine" region into two parts, ($q = 6.3 \times 10^6 - 2 \times 10^8$ and $q = 2 \times 10^8 - 1.8 \times 10^{10}$, the extracted Hurst exponents for are $H_{larger\lambda}$ = 1.18 and 1.11 and $H_{smaller\lambda}$ = 0.75 and 0.78 for NCD and MCD, respectively. Indeed, the roughness seems to be qualitatively different in these two portions of the curve, with the upper portion having a scaling behavior of $C \propto q^{-4}$, corresponding to H=1.5. The physical origin of these differences in scaling behavior between different length scales is discussed in detail in the next section. Third, and most importantly, the whole practice of assigning a single Hurst exponent to describe a surface seems inapplicable to these materials. In general, it is mathematically

convenient to assume self-affinity in numerical and analytical models, and it is common practice in experiments to measure topography over a limited range of scales and then to extrapolate to other scales using the assumption of self-affinity. However, at least for the present materials this practice is not supported. It is instead preferable to measure the entire size scale of topography and input this full PSD into the mathematical models.

5.4 The Effect of Grain Size on Topography

As mentioned previously, the larger-grain-size materials (NCD and MCD) demonstrate a clear region of scaling of q^{-4} for the larger-wavelength portion of the "self-affine" region. This scaling is characteristic of kinks in the real-space line scan. Such kinks can be an artefact of the nonvanishing tip radius[17,48]. Therefore, these artifacts must be first ruled out as an origin for q^{-4} scaling in the PSD. However, in the present work, this q^{-4} scaling is clearly observed both in the reliable portion of the AFM measurement and in the TEM measurement, both of which are free from tip-based artifacts. Therefore, this q^{-4} scaling in the PSDs of the MCD and NCD is a feature of the measured topography, rather than emerging from an artifact. Furthermore, the kinks in the real-space height behavior are directly observable in the TEM imaging, as shown in Fig. 14a and Fig. 16.

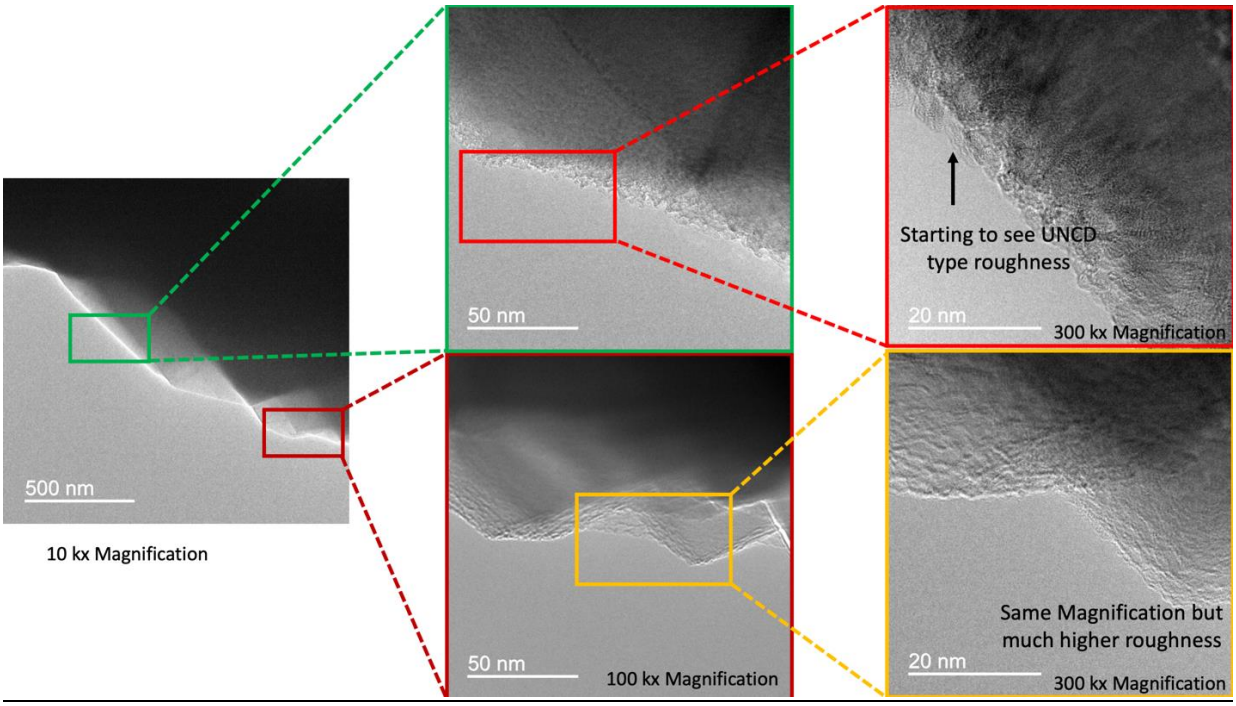

Figure 16 TEM images of MCD at different magnifications. As the surface is zoomed more features start becoming visible and MCD roughness starts looking like UNCD.

The hypothesis to describe this q^{-4} scaling is that it is characteristic of topography below the grain size of the material (i.e., for $q \gg 2\pi/l_g$, where l_g is the mean grain size). At sizes much below the grain size, the topography reverts to random, self-affine behavior, showing roughness very similar to UNCD (Fig. 16), where the PSD scales as q^{-1-2H}. The mathematical basis for this hypothesis is given in Appendix B.

In order to demonstrate how the PSD is affected by the superposition of a characteristic grain size and random roughness below that size, artificial one-dimensional surfaces were generated that were made up of (a) a superposition of triangular peaks, (b) self-affine roughness, and (c) the combination of those two into a single surface. The facetted profiles are generated following two different approaches. In surface 1 (Fig 17a) the slope alternates between -1 and 1 and the heights of the peaks are drawn from a Gaussian distribution. The spacing of the peaks and

the valleys separating them results from the heights and the slopes. The last valley makes the connection between the last peak and the first, ensuring periodicity. The heights and the positions x are rescaled so that the average kink spacing is l_k and the rms-slope is h'_{rms}. In surface 2 (Fig 17b), the kink heights were drawn from a Gaussian distribution and the spaces between the kinks from a Rayleigh distribution. Uniform and exponential distribution of kink spacing was also tested and find that the overall picture remains. The positions were scaled so that the average kink spacing is l_k and the heights are scaled to match the desired rms-slope h'_{rms}. Fig 17c shows that the PSDs of the two profiles are almost identical. The small scale self-affine random roughness (surface 3, Fig 17d) was generated using a Fourier-filtering algorithm[17,73]

The PSD of the superposition (surface 4, Fig 17e) of the facetted scan (surface 2, Fig 7b) and the self-affine random roughness (surface 3, Fig 17d) can be separated in 3 regions: (1) at large wavelength (small wavevector q) the PSD is flat, reflecting the uncorrelated heights of the kinks (random noise), (2) at wavelength below $4l_k$ the PSD scales as q^{-4}, (3) at wavelengths below $2\pi/q_{sa}$it shifts from q^{-4} to q^{-1-2H}. q_{sa} is defined as the wavevector at which the PSD of the the small scale self-affine random roughness (Surface 3) crosses the PSD of the facetted profile (Surface 2).

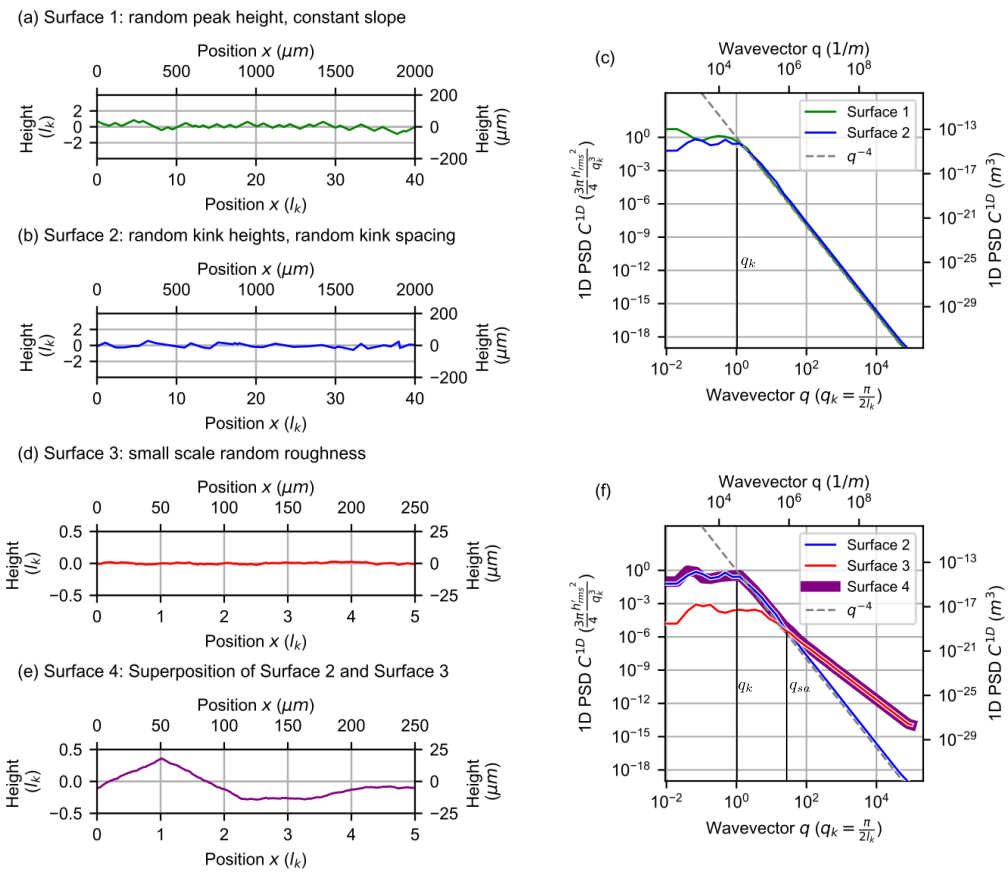

Figure 17 Computer generated random profiles (a,b, d, e) and their PSDs (c, f). The PSDs are averaged over logarithmically spaced bins. The top and right axis of each plot are in dimensional units and the bottom and left axis are normalized. (a, b) Facetted profiles with an rms-slope of 0.5, a length of 1 cm and 100 peaks, yielding an average kink spacing $\boldsymbol{l_k}$ of 100µm. (a) Surface 1 is generated with random peak height but constant slope. (b) Surface 2 is generated with random heights and random spacing. (c) PSD of the two surfaces shown in panels (a) and (b). (d) Self-affine random roughness (Surface 3) with Hurst exponent 0.7 and slope 1.4 generated using a Fourier-filtering algorithm[17,73]. (e) Sum of surface 2 and surface 3, yielding a composite surface with self-affine roughness below the grain scale. (f) PSDs of surface 2, 3 and 4. $\boldsymbol{q_k}$indicates the transition from the flat roll-off region to the $\boldsymbol{q^{-4}}$ scaling region. The choice of the particular value $\boldsymbol{q_k = \frac{\pi}{2l_k}}$ is motivated from the mathematical considerations in the Appendix B. $\boldsymbol{q_{sa}}$ is defined as the crossing of the PSDs of Surface 3 and Surface 2. The rms-slope of the facetted profiles $\boldsymbol{h'_{rms}}$ has been used to normalize all PSDs.

Surface 2 in Fig.17 has uncorrelated peak heights and hence has the flat PSD characteristic of random noise for wavelengths above the grain size. While this model fits quite well to the PSD of MCD and NCD, other surfaces may be self-affine also well above the grain size. We generate such a surface by altering slightly the method used to generate surface 2, where the kink heights are taken from a self-affine random surface instead of being uncorrelated random variables. We checked that changing the spacing of the kinks from regular to random values didn't change substantially the PSD in the self-affine scaling region. The PSD of the combined surface exhibit 4 regions: flat roll-off, self-affine scaling, q^{-4}-scaling and self-affine scaling (Fig.18).

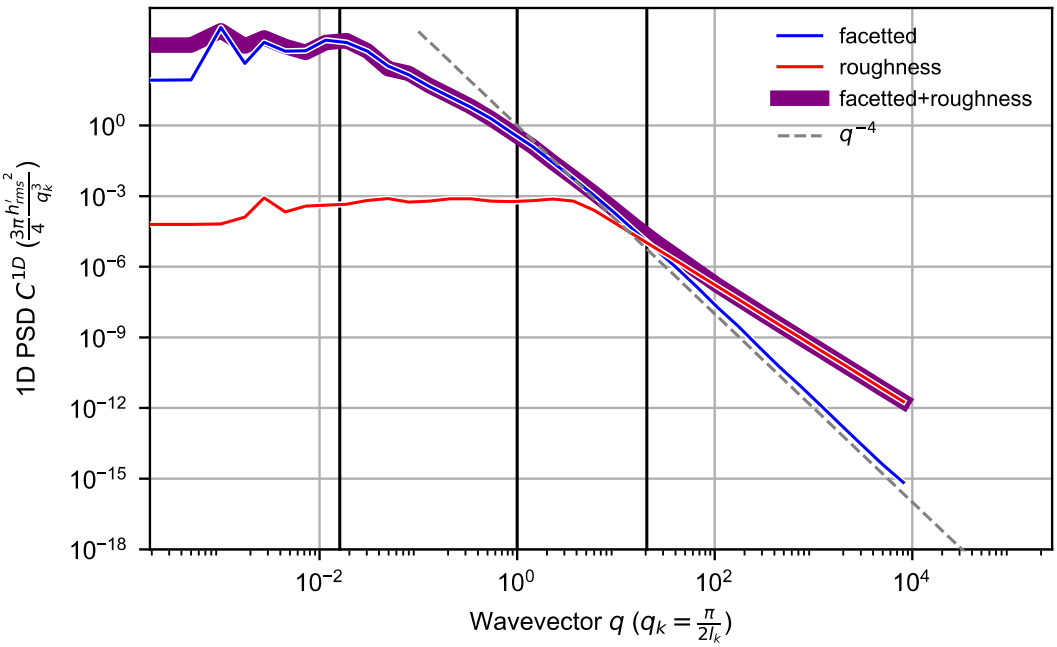

Figure 18 PSD of computer generated random profiles with self-affine scaling above the grain size. The PSDs are averaged over logarithmically spaced bins and the rms-slope of the facetted profile $\boldsymbol{h'_{rms}}$ has been used to normalize all the PSDs. The facetted profile is self-affine above the grain-size, so that the combined PSD exhibit 4 regions separated by black vertical lines: flat roll-off, self-affine scaling, $\boldsymbol{q^{-4}}$scaling and self-affine scaling.

*Note – All the simulation that are shown and computer-generated surfaces that were created were performed by the collaborators at University of Freiburg.

5.5 Conclusions from Objective 2

In conclusion, the topography of four different nanocrystalline diamond substrates have been evaluated and compared. A comprehensive description of topography at all scales can be generated by measuring topography using three different techniques: stylus profilometry; atomic force microscopy; and side-view electron microscopy, all combined using the power spectral density.The surface roughness varies significantly with scale, with surfaces that are smoother when measured at the large-scale showing roughness that is identical or even higher, when measured at the smaller scales. For these nanocrystalline diamond surfaces, we could *not* identify a single-valued scaling exponent (Hurst exponent or fractal dimension) that accurately described the topography over a large range of scales. Instead, their grain size introduced a signature into the power spectral density, showing q^{-4} scaling behavior below the grain size, with self-affine-like scaling (H~0.6-0.8) at size scales larger or much smaller than the grain size. It was shown using computer-generated surfaces why these signatures should emerge.

6.0 Results and Discussions for Objective 3: Experimentally Measure Surface Adhesion to Interrogate the Many Competing Rough-surface Mechanics Models.

Many natural and engineering processes—such as a human picking up an object, a gecko climbing trees, or a tire gripping the road—require enough adhesion and friction to achieve the task, while maintaining the ability to release the surface afterward [6,77,78]. All natural and manmade surfaces contain roughness at some scales, and this roughness strongly affects adhesion [8,79,80]. Therefore, fundamental understanding of the reversible adhesion of a soft material to a rough surface is a grand scientific challenge, with significant technological applications. For instance, pick-and-place techniques in manufacturing are used from large-scale factories [81] all the way down to nanoscale transfer printing [82]. Biomedical devices must securely adhere to skin when measuring vital signs or delivering drugs, but then must be removed without pain for disposal or reuse [83]. Tires, seals, and gaskets are used extensively in vehicles and industrial machinery [6]. And finally, there has been significant recent progress in the field of soft robotics, with the goal of creating machines that will be able to manipulate objects like the human hand or climb walls like geckos[84].

Our understanding of adhesive contact between smooth soft elastic materials was elegantly resolved in a seminal paper in 1971, where Johnson, Kendall, and Roberts (JKR) showed that the contact area under applied load is larger than predicted by the classic Hertz model [85,86]. However, the presence of surface roughness significantly alters the contact behavior. As a rough contact is loaded, it obeys the *trends* of the JKR model, but the measured apparent work of adhesion W_{app} is significantly lower than the intrinsic value W_{int}; the latter is a thermodynamic parameter that depends on intermolecular interactions between the materials[2]. Upon retraction, adhesion hysteresis is observed on rough surfaces, where the behavior deviates significantly from that of

loading and from the JKR predictions. If the JKR formalism is applied, one calculates a work of adhesion (for retraction) that is much larger than W_{int} and may not have thermodynamic significance [87–91].

Even though all practical surfaces are rough, quantifying the loss of adhesion due to roughness has remained a challenge. One widely-used category of models describes rough surfaces as an array of individual contacting bumps (asperities) of a certain size [19,92,93], where the surface properties are computed from the collective behavior of the individual asperities. However, these models focus only on a single size scale of roughness, whereas most natural and engineering surfaces are rough over many length scales [94,95]. To address the multi-scale nature of roughness, Persson developed a set of continuum mechanics models to describe soft-material adhesion at rough contacts as a function of the power spectral density (PSD) [13,34,96]. In particular, under the assumption that the soft material fully conforms to the roughness of the hard material, and by assuming that the materials behave linear elastically, one such model [34] predicts how the intrinsic work of adhesion W_{int} can be replaced by an apparent value W_{app} that depends on material parameters and surface roughness.

While the aforementioned mechanics models describe the behavior of a material under load, they do not predict the adhesion hysteresis, the difference in behavior between loading and separation. Instead, the increase in adhesion energy upon retraction is often attributed (sometimes without evidence) to velocity-dependent dissipation of energy due to bulk viscoelasticity [97–99]. However, roughness-induced adhesion hysteresis is still observed even for systems that show no evidence of viscoelasticity on smooth surfaces [100,101]. Furthermore, it may not even be appropriate to apply an equilibrium-based theoretical model (such as JKR for smooth surfaces or Persson's model for rough surfaces) to the non-equilibrium separation behavior [102,103].

Thus, our current understanding of adhesion hysteresis is incomplete. Here, we investigate the origins of energy loss in order to demonstrate the fundamental contribution of surface roughness.

6.1.1 *In Situ* Adhesion Experiments

To understand the dependence of adhesion on roughness, *in situ* measurements of the load-dependent contact of sixteen different combinations of soft spheres and rough substrates were performed. PDMS was chosen as elastomer and synthetically grown hydrogen-terminated diamond as the hard-rough substrates because both have low surface energies. We wanted to avoid adhesion hysteresis due to interfacial bonding (for example, PDMS in contact with silica surfaces) [104,105]; therefore, low-energy materials were chosen [106] to focus specifically on the adhesion hysteresis that arises due to surface topography.

Four types of soft, elastic PDMS hemispheres were synthesized following the methods from Refs. [99,107,108] with elastic moduli ranging from 0.7 to 10 MPa. The PDMS hemispheres were loaded under displacement control to a maximum load of 1 mN before unloading to separation. (The synthesis and testing are described in Appendix C and Appendix D, respectively). Real-time measurements were made of contact radius, load, and displacement, as shown in Fig. 19.

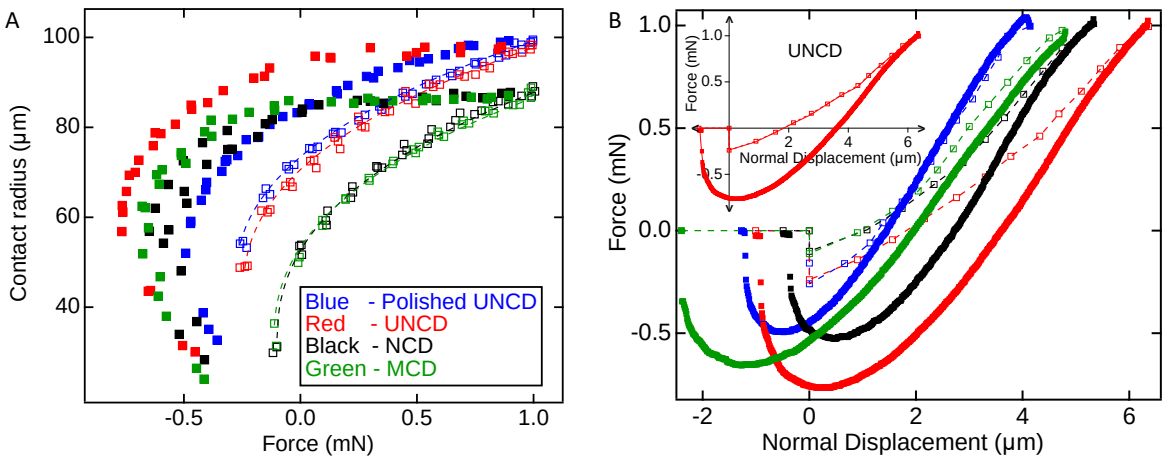

Figure 19 Adhesion measurements during approach and retraction. Loading and adhesion tests were performed with ultra-smooth PDMS hemispheres of varying stiffness from 0.7 to 10 MPa. Representative curves from one material (with E=1.9 MPa) are presented in this figure, with those of other materials shown in Appendix Fig. 4. The load-dependent contact radius (A) was measured using in situ optical microscopy. The apparent work of adhesion upon approach $\boldsymbol{W_{app}}$ was extracted by fitting the loading data (hollow points) using the JKR model (dashed lines). The force-displacement curves (B) were used to calculate the energy loss $\boldsymbol{E_{loss}}$ during contact by performing a closed-circuit integral (inset). Both approach and retraction experiments were conducted at a very low speed, 60 nm/s. . Images A and B reproduced from Ref.[45], copyright National Academy of Science, 2019.

The apparent work of adhesion during approach W_{app} was extracted by using the JKR model to fit the measured contact radius a as a function of load F [86]:

$$a = \left[\frac{3R}{4E^*}\left(F + 3\pi R W_{app} + \sqrt{6\pi R F W_{app} + \left(3\pi R W_{app}\right)^2}\right)\right]^{1/3} \qquad 6\text{-}1$$

where R is the radius of the hemispherical lens and the effective modulus E^* is defined as $1/E^* = (1-\nu_{\text{sphere}}^2)/E_{\text{sphere}} + (1-\nu_{\text{substrate}}^2)/E_{\text{substrate}}$, E is Young's modulus and ν the Poisson

ratio. This yielded a different value of apparent work of adhesion for each of the sixteen contacts. The surface chemistry of the PDMS and the nanodiamond is expected to be similar in all cases, therefore all contacts should have approximately the same value of W_{int}. Before testing the hemispheres with rough surfaces, they were tested against a smooth silicon wafer coated with a low-surface energy octadecyltrichlorosilane (OTS) monolayer to verify that there is negligible adhesion hysteresis due to viscoelasticity (Appendix Fig. 5).

*Note: The adhesion experiments were performed by our collaborator at The University of Akron.

6.1.2 Work of Adhesion Calculations

To analyze the dependence of W_{app} on modulus and multi-scale surface topography, a model of conformal contact, based on Persson and Tosatti[34] was used. Those authors postulated that the product of W_{app} and A_{app} (the apparent or projected area) is given by a balance of adhesive energy and stored elastic energy U_{el}:

$$W_{app}A_{app} = W_{int}A_{true} - U_{el} \qquad 6\text{-}2$$

with $W_{int} = \gamma_1 + \gamma_2 - \gamma_{12}$, where γ_1 and γ_2 are the surface energies of the soft and hard surfaces, respectively, and γ_{12} is the interfacial energy between them. The term A_{true} is the true surface area of the rough hard surface. However, Eq. 6-2 makes two important assumptions that must be addressed: it neglects the change in area of the soft elastomer surface from A_{app} to A_{true} upon

contact; and it assumes that the surface energy of the soft material is independent of strain. These two assumptions can be corrected by modifying the energy balance to explicitly include the work done in increasing the surface area of the elastomer.

The Persson-Tosatti energy balance implicitly implies that the area of the PDMS surface does not change. While this may be valid for small-slope surfaces, in the more general case the area will increase from A_{app} to A_{true}, as shown schematically in Fig. 20.

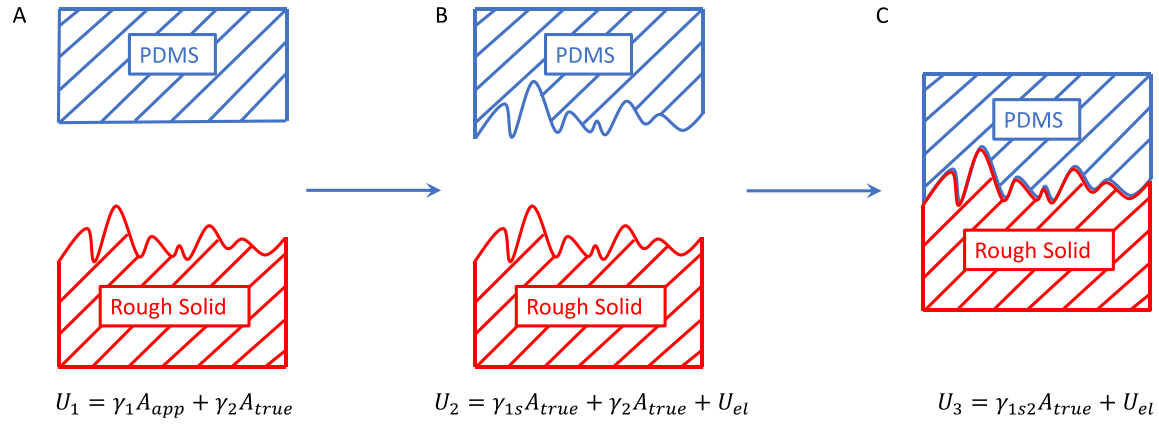

Figure 20 During adhesion, the materials go from the initial state (left) to the final state (right). However, to fully account for the energy change, one must consider the change in area of the soft material, which is represented schematically by including the intermediate state (middle). Images A, B and C reproduced from Ref.[45], copyright National Academy of Science, 2019.

To go from the initial state (Fig 20A) to the intermediate state (Fig. 20B), there is an energy change from U_1 to U_2. The PDMS is stretched and its surface energy changes depending upon the applied strain, which can be represented as a function of the area:

$$\Delta U_{1\to 2} = \int_{A_{app}}^{A_{true}} \gamma_1(A) dA + U_{el} \qquad 6\text{-}3$$

Then, to go from the intermediate state U_2 (Fig. 20B) to the final state U_3 (Fig. 20C), there is an energy change of:

$$\Delta U_{2\to3} = (\gamma_{1s2} - \gamma_{1s} - \gamma_2)A_{true} \tag{6-4}$$

Thus, the total work to go from the initial state to the final state is equal to $\Delta U_{1\to2} + \Delta U_{2\to3}$:

$$\Delta U_{1\to3} = \int_{A_{app}}^{A_{true}} \gamma_1(A)dA + U_{el} + (\gamma_{1s2} - \gamma_{1s} - \gamma_2)A_{true} \tag{6-5}$$

This is the total energy change equal to $-A_{app}W_{app}$. Finally, the total energy balance can be re-written as:

$$W_{\text{app}}A_{\text{app}} = W^*_{\text{int}}A_{\text{true}} - \int_{A_{app}}^{A_{true}} \gamma_{1s}(A)dA - U_{el} \tag{6-6}$$

where, $W^*_{\text{int}} = \gamma_{1s} + \gamma_2 - \gamma_{1s2}$, and γ_{1s} is the surface energy of the stretched elastomer. If the assumption is now made that the surface energy of the soft elastomer is not a strong function of strain[109], then $W^*_{\text{int}} = W_{\text{int}}$ and we can simplify the energy balance, and rearrange it to explicitly show W_{app} as a function of two roughness-dependent terms, A_{true}/A_{app} and U_{el}/A_{app}:

$$W_{app} = W_{int}\frac{A_{true}}{A_{app}} - \gamma_1\left(\frac{A_{true}}{A_{app}} - 1\right) - \frac{U_{el}}{A_{app}} \qquad 6\text{-}7$$

The stored elastic strain energy can be calculated from the power spectral density using the approach of Persson and Tosatti[34]:

$$\frac{U_{el}}{A_{app}} = \frac{E^*}{8\pi}\int_0^\infty q^2 C^{iso}(q)\,\mathrm{d}q \qquad 6\text{-}8$$

where, C^{iso} is the radial average of the two-dimensional power-spectral density. For calculating the power spectral density, the conventions used in Ref.[17] are followed. C^{iso} was calculated from the one-dimensional PSD (Fig. 15) as follows: under the assumption of isotropic roughness, the 2D PSD can be calculated from the 1D PSD, as described in Ref.[17]. For this, Eq. A.28 of Ref.[17] is used:

$$C^{iso}(q) \approx \frac{\pi}{q\sqrt{1-\left(\frac{q}{q_s}\right)^2}}C^{1D}(q) \qquad 6\text{-}9$$

where q_s is the short wavelength cut-off, in this case defined by the minimum wavelength at which roughness is measured (4 Å). This form of the 2D PSD is shown in Appendix Fig. 2 and is used in the calculations for stored elastic energy and true surface area (Eqs. 6-8 and 6-10).

Finally, a closed-form expression for the roughness-dependent increase in surface area is derived, which works for arbitrary values of root-mean-square surface slope h'_{rms} (Appendix E):

$$\frac{A_{true}}{A_{app}} = 1 + \frac{\sqrt{\pi}}{2} h'_{\text{rms}} \exp\left(\frac{1}{h'^2_{rms}}\right) \text{erfc}\left(\frac{1}{h'_{rms}}\right) \qquad 6\text{-}10$$

with h'_{rms} calculated from the PSD as $(h'_{rms})^2 = \frac{1}{2\pi}\int_0^\infty q^3 C^{iso}(q)\,\mathrm{d}q$[17]. For generality, all integrals were performed over the entire range of size scales over which topography was measured; if the range of wavevectors is instead cut off at the contact size (c.a. 100 microns), the extracted results are identical (within 0.1%). Taken together, Eqs. 6-7,6-8 and 6-10 demonstrate the predicted dependence of W_{app} on material properties (E, ν) and topography C^{iso}.

The model for W_{app} (Eq. 6-7) was applied to the measured data as shown in Fig. 21A using γ_1 = 25 ± 5 mJ/m^2 for PDMS. This value was chosen based on prior work [106,110], which also showed that the surface energy of PDMS does not change significantly with molecular weight. Furthermore, in the present investigation, water contact-angle measurements were performed on all PDMS materials and yielded values in the range of 103° - 107°, further supporting that all PDMS materials used in this investigation have similar surface energy. In applying this model, the minimum physically reasonable value of W_{app} is set to zero; predicted values below zero (for 10 MPa PDMS on NCD and MCD) imply that the surfaces will not perfectly conform. The best correlation between the experimentally measured work of adhesion and the predictions of Eq. 6-7 was obtained using the intrinsic work of adhesion of 37.0 ± 3.7 mJ/m^2 (R^2 = 0.67). The reasonable value of R^2 (0.67) and the low value of standard error (3.7 mJ/m^2) suggest good agreement between the model and the experimental measurements. The scatter in the experimental values as compared to the model was attributed to spot-to-spot variations. The theory outlined above cannot capture these spot-to-spot variations because it assumes a thermodynamic limit, corresponding to contacts

of infinite size. The finite size of the experimental contact means that it is subject to finite-size fluctuations, such as a non-negligible probability for single anomalous asperities to dominate the response at low loads [111]; this does not happen for theoretical contacts which sample the whole statistical distribution of the surface's roughness. Overall, the proposed model which explicitly accounts for the change in area of the soft surface (Eq. 6-7) achieves significantly improved model predictions; if we do not account for this change (calculations shown in Appendix F), the best fit to the measured data is significantly poorer ($R^2 = 0.29$).

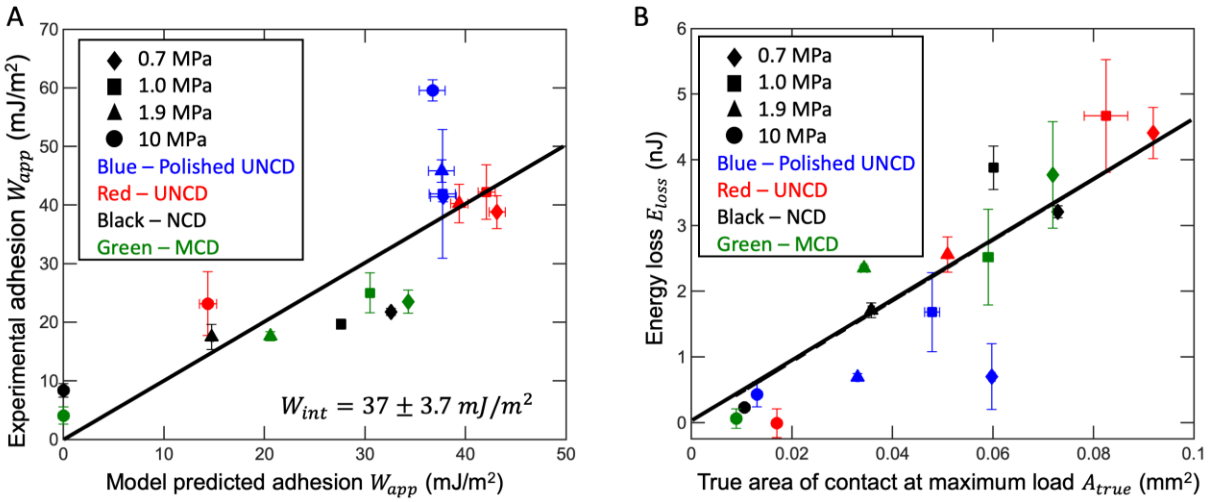

Figure 21 Comparison of work of adhesion and energy loss with the proposed model of conformal contact. In panel A, experimental measurements of apparent work of adhesion during approach are well-fit using the balance of adhesive and elastic energy described in the main text (Eqs. 6-7, 6-8 and 6-10); here the solid line represents y = x. In panel B, the energy loss is plotted as a function of true contact area (Eq. 6-11). The solid line is a linear fit to the data and has a slope of 46.1 ± 7.7 mJ/m^2 ($R^2 = 0.8$). Images A and B reproduced from Ref.[45], copyright National Academy of Science, 2019.

The retraction portion of contact differs sharply from approach (as shown in Fig. 19), and the JKR model does not provide an adequate fit to the unloading data. Despite the poor fit, the JKR model can be used to extract a value for work of adhesion upon retraction, either by applying

it only to the pull-off point, or by applying it to the several (c.a. 6) points before pull-off. Doing so (Appendix D) yielded work of adhesion values in the range of 20 – 160 mJ/m^2. However, there was little consistency between these values and there was no connection to the intrinsic value of work of adhesion determined from the approach data.

Instead, the total energy loss during contact and separation was analyzed. This quantity was computed as the integral under the loading and unloading curve, as shown in the inset in Fig. 19B. The *in situ* measurements of contact size yielded the *apparent* area of contact during testing; to determine the true area of contact, the roughness-induced increase in true surface area (Eq. 6-10) was multiplied. The energy loss E_{loss} versus the true area of contact A_{true} *at maximum preload* was plotted. Figure 21B showed a linear correlation:

$$E_{loss} = W_{int} A_{true} \qquad 6\text{-}11$$

with a best-fit intrinsic work of adhesion of 46.2 ± 7.7 mJ/m^2. The prior value of the work of adhesion (37.0 ± 3.7 mJ/m^2) was measured during approach from the measured contact radius as a function of applied load. The latter value of work of adhesion (46.2 ± 7.7 mJ/m^2) was obtained for the whole contact cycle (approach and separation) using the closed-circuit integral of the force-displacement curve. These values agreed within their experimental uncertainties, despite being measured using very different approaches. This agreement suggests that we are indeed measuring an intrinsic work of adhesion for the materials, governed by the fundamental molecular interactions, rather than an effective property that may be governed by experimental parameters.

The present description of soft-material contact on rough surfaces assumes fully conformal contact. No method exists at present to directly verify this assumption; neither the *in situ* optical microscopy used in this investigation, nor the fluorescence or other techniques for imaging contact used elsewhere (e.g., Ref. [112]). However, the present results demonstrate that the experimentally measured behavior of these sixteen material pairs, during both loading and separation, is consistent with a model of conformal contact. This provides indirect evidence for the accuracy of this description of contact, and its underlying assumptions.

6.2 Conclusions from Objective 3

These results in Fig. 21 provide a simple physical mechanism to explain both the lower work of adhesion during approach and the adhesion hysteresis upon retraction. During approach, the apparent work of adhesion is reduced from W_{int} by the energy required to deform the soft material to achieve conformal contact. This reduction can be quantitatively calculated using comprehensive, multi-scale measurements of topography (Eqs. 6-7,6-8 and 6-10). Furthermore, the energy loss during contact and separation matches with the product of W_{int} and the *true* contact area A_{true} at the maximum preload. Surface heterogeneities are known to pin the contact edge such that the retraction process depins the surface in instantaneous jumps over small localized microscopic regions [113]. We show that Griffith's argument can be applied: these jumps occur once the elastic energy available is equal to the interface energy, and all elastic energy is dissipated in the creation of new surface [114].

Overall, the results show significant adhesion hysteresis in the absence of viscoelastic dissipation, and therefore demonstrate a fundamental origin of irreversible energy loss in soft materials that arises due to the roughness-induced increase in surface area and Griffith-like separation of the contact. Equations 6-7,6-8,6-10 and 6-11 quantify the relative contributions to measured adhesion from material properties (intrinsic work of adhesion, elastic modulus, and Poisson ratio) and from surface topography (as characterized by a multi-scale PSD including atomic-scale information). This understanding suggests strategies to predict adhesion and to rationally modify it by tailoring the surface composition and surface topography.

*Note - Portions of the text have been taken (with or without modification) from my publications:

1. Dalvi, S.*; Gujrati, A.*; Khanal, S. R.; Pastewka, L.; Dhinojwala, A.; Jacobs, T. D. B. Linking Energy Loss in Soft Adhesion to Surface Roughness. Proc. Natl. Acad. Sci. U.S.A. **2019**, *116* (51), 25484-25490. © National Academy of Sciences, 2019.

7.0 Future and Ongoing Work

7.1 Task 1: Determine the Influence of Surface Topography on Adhesion in Hard Materials

The difficulty of measuring small-scale topography has required significant assumptions about the correct input parameters to lot of adhesion models[5,8,19,29].These assumptions have limited the experimental validation of the models. Therefore, the objective of this task is to quantitatively evaluate the accuracy of the competing adhesion models. The overall approach is to perform micro- and macroscale adhesion measurements on the surfaces that were characterized in hard-soft adhesion. These results will be used to evaluate quantitative predictions from analytical models of rough-surface adhesion and assess the effect of small-scale roughness on large-scale adhesion.

7.1.1 Measurement of Roughness Modified Adhesion on Pre-characterized Surface

Using a micromechanical tester, adhesion is directly measured between the characterized nanodiamond films and spherical probes composed of Ruby. The test system is modular and includes a 6-axis stick-slip positioner for large positioning, a closed-loop linear piezo-actuator for testing, and capacitive MEMS-based load cells for force measurement. Adhesion tests are performed in a high-vacuum environmental chamber at a pressure of approximately 10^{-6} Pa and relative humidity kept to less than 3% to minimize capillary attraction. For each surface of interest, repeated automated adhesion tests will be performed in different locations on the planar surface, in order to ensure repeatability and to characterize the variability. The adhesion test is performed

with sphere 250 μm. A spherical shape was chosen to eliminate the problems of planarity and dependence on misorientation that complicate adhesion measurements using a flat punch (as shown in fig. 22a). All the tests were conducted 100 times on each surface with maximum load of 10 μN.

Due to high inconsistencies in the results, attached ruby spheres were characterized to check their roughness and they were found to have around 1 μm asperities and a very high average roughness (fig. 22b). To mitigate this problem, unpolished sphere is glued at a random orientation to a flat metal face a fiducial mark is made using a diamond scribe to identify the orientation. Sphere is then unglued, cleaned using acetone and isopropyl alcohol and placed onto a vee-jewel holder with the mark facing upwards. Next, it is polished 0.05 μm suspension of Alumina at 400 rpm for 2 minutes, this leads to single nanometers of average roughness. The sphere is unglued and cleaned once again and then attached to force probe using glue (Crystalbond), with polished side facing down and scribed side glued. This step ensures a highly smooth sphere (fig. 22b) with a very small shape change, of around 20 μm. Finally, some initial results are gathered on polished ultrananocrystalline diamond (UNCD), unpolished UNCD, nanocrystalline diamond (NCD) and microcrystalline diamond (MCD), with polished Silicon wafer being reference surface (fig. 22c). These tests show a predictive adhesion behavior between hard rough surfaces; with increase in roughness adhesion decreases. One more thing to notice is that unpolished UNCD has a slightly lower adhesion than MCD, which might suggest that there is an effect of small-scale roughness.

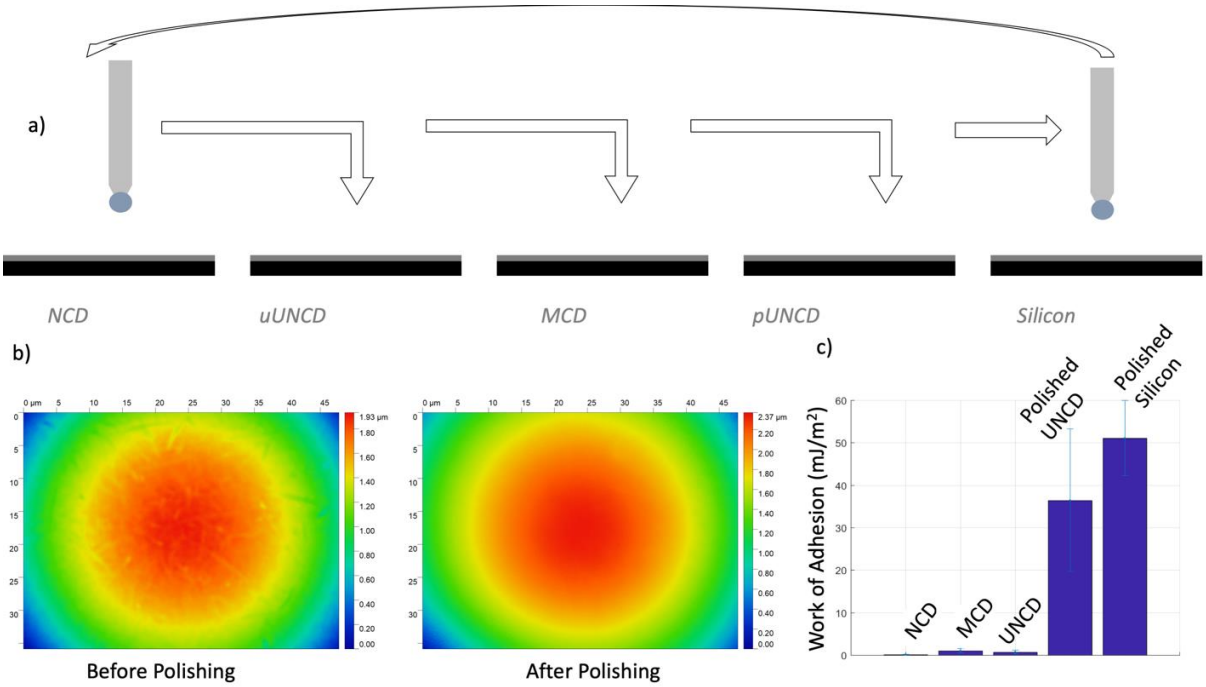

Figure 22 Adhesion tests on variety of crystalline diamond surfaces. 100 tests each are conducted cyclically on five different surface (a). The spherical probes are characterized and polished to get them highly smooth (b). Initial results show a trend of higher adhesion with lower roughness (c)

Precise adhesion measurements are made and coupled with extensive roughness characterization. Careful adhesion measurements reveal adhesive properties of hard interfaces of interest. Next steps are to do: 1) AFM on the polished sphere and simulate contact with fully characterized surfaces, to gain understanding of adhesion at small scale and how it compares with experimental values. 2) Experimental measurements will be used to test the validity of contact models and continued comparisons will reveal parameters responsible for hard material contact properties.

7.2 Task 2: Systematically Investigate Roughness-dependent Adhesion by Using Lithographic Patterning to Design and Interrogate Pseudo-random Surfaces

The overall approach is to create a set of surfaces that have identical patterning on the large scales but systematically varying roughness on the small scales, and then to characterize their topography and adhesion. The rationale for this aim is to two-fold: to demonstrate the general principle of modifying small-scale roughness to rationally enhance or reduce adhesion on patterned surfaces, as well as to develop a specific technique to do so.

Working with collaborator at ORNL, silicon oxide surfaces will be created with controlled roughness at the large and small scales. For the large-scale topography, virtual surfaces will be generated using a Fourier filtering algorithm[73] and patterned into silicon using grayscale electron-beam lithography. Specifically, this will be accomplished by spin-coating a polymethylmethacrylate (PMMA) resist on the silicon substrate, and then subjecting it to a spatially varying electron dose. The dose at each pixel is programmed by the desired height of the final surface, causing the PMMA to be partially or completely removed (depending on dose) in an appropriate solvent. Finally, the patterns will be transferred into the silicon using reactive ion etching, with a recipe that etches PMMA and silicon at approximately the same rate. This process will be used to create multiple replicates with identical topography, which is well controlled over the scale from 50 nm (the pixel size) to 100 μm (the pattern size). Then, on top of the large-scale replicates, varying small-scale topography will be superimposed. This will be achieved using plasma enhanced chemical vapor deposition (PECVD) of silicon oxide films. The initial roughness can be controlled by varying the temperature of the substrate between 25 and 250℃ and will be determined through initial studies.

Then, using rapid thermal processing, the samples will be subjected to controlled annealing[115,116] at approximately 1200℃ in a controlled atmosphere of argon gas. By precisely and systematically varying the annealing time, different samples will be smoothened to different degrees.

A virtual surface was designed and then patterned in silicon using grayscale e-beam lithography, as shown in Fig. 23a. Duplicates of this surface were created to verify reproducibility, and arrays of these duplicates were stitched together to create 300x300-μm areas of controlled topography. Fig. 23e shows the double sinusoidal pattern created. AFM imaging was done to determine whether the patterned surfaces match the virtual surfaces created as shown in fig 23 b, c and d. AFM images of sinusoidal surfaces were created with normal grey scale patterning and other one with narrow grey scale pattern and this changes the amplitude (roughness) of the surface.

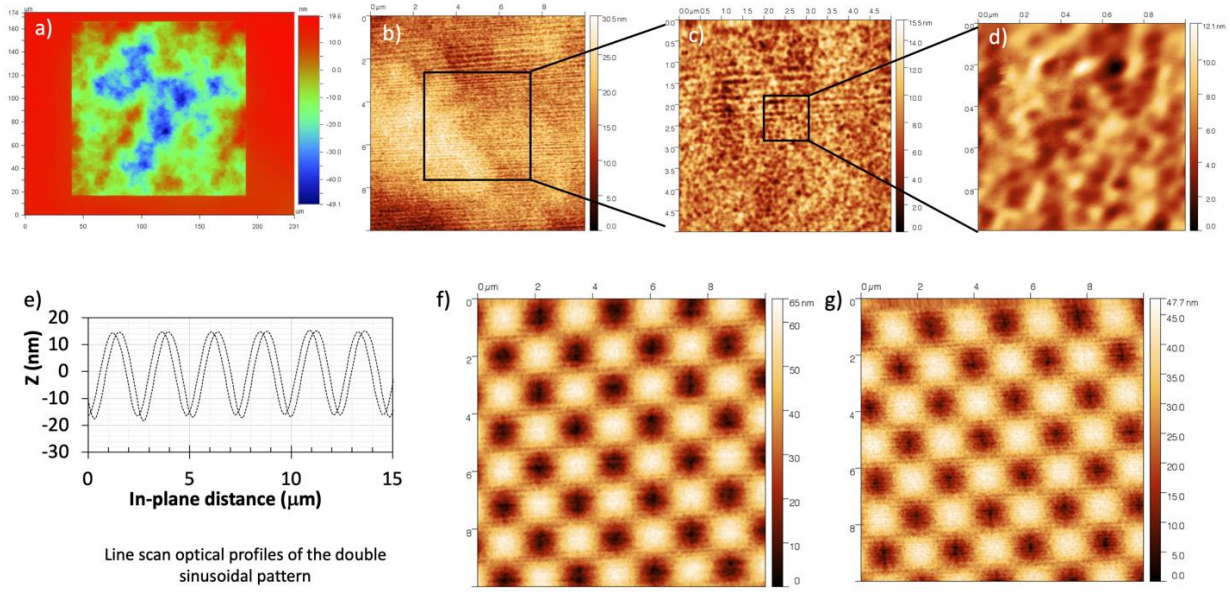

Figure 23 The patterned surfaces from ORNL. Random virtual surface (a) and double sinusoidal surfaces (e) are created. Multi resolution AFM scans are performed (b-d). Scans on double sinusoidal surface shows difference in roughness for normal greyscale patterning (f) and narrower grey scale patterning (g), where latter turned out to have less peak to valley roughness.

Adhesion test using ruby spheres (similar to previous task) and these patterned surfaces will be performed to understand the effect of small-scale roughness on adhesion between hard-hard contact. It will be interesting to see how adhesion changes when we can control and modify roughness at different scales.

Finally, with characterization of roughness at multi-scale we can have deeper understanding of fundamentals of hard-soft and hard-hard adhesion. For small-scale devices, the proposed research can not only enhance the reliability and function of existing device technologies, but it has the potential to enable new classes of devices. Entire classes of microdevices containing intermittent contact and/or sliding have been demonstrated in a lab, but never commercialized due to failures related to high adhesion and high friction (which is related to adhesion[117]).

8.0 Conclusions

As previously alluded in this document, a mechanistic understanding of adhesion the performance and lifetime of small-scale devices and advanced manufacturing techniques. Soft material adhesion in general is critical in the fields of transportation (tires, gaskets, seals), biomaterials, micro-contact printing, and soft robotics. Also, the dependence of adhesion on surface roughness is also well known. Thus, the need to get comprehensive surface characterization is of prime importance.

Here, the surface is characterized over eight orders of magnitude. This characterization was started with characterization using just the AFM, but it was soon understood that there is a definite need to capture small scale topography in some other way. It was found that there is an inherent unreliability while measuring very small scales if using convention probe-based techniques due to physical size of the probe. If the roughness is of the order of the radii of the probe, then the technique cannot capture the truly small roughness. To alleviate this problem, a novel method to capture roughness using TEM was developed.

Two separate methods were developed to prepare cross-section samples for the TEM. One, which was surface-preserving cross-section and the other, deposition of a thin-film material onto a pre-fabricated TEM substrate. Both methods were validated and were shown to be reliable. To validate that there is no effect of thickness mathematical simulations were used and they yielded nearly identical outcomes for surfaces of different thickness.

Critical surface parameters like RMS slope and curvature though are scale dependent but TEM allowed to get most accurate values for these parameters by capturing reliable data at very small scales (a few tens nanometers to Ångstroms). Another key outcome to come out of this study

was the combination of topography measurements across all size scales to get scale-independent surface parameters. It can also be seen that multiple PSDs can be combined to produce a comprehensive multi-scale curve which is almost a complete representation of the surface. This characterization approach is widely applicable to many materials as shown by using the same approach to characterize Polished UNCD, NCD and MCD. Further, this approach can be used to experimentally validate many analytical models that currently exist.

In fact, this approach is used to understand soft material adhesion with rough surfaces. By using complete spectrums of nanodiamond surfaces and using a modified Persson-Tosatti model simple physical mechanism to explain both the lower work of adhesion during approach and the adhesion hysteresis upon retraction was provided. The reduction in work of adhesion during approach can be explained by loss of energy that is required to deform and make a conformal contact. Also, during separation energy loss is matched by the product of work of adhesion and true contact area. These results revealed the direct relationship between Griffith fracture and the detachment of adhesive contacts and suggest a quantitative model that describes both the loading and separation behavior. These insights can be leveraged in applications involving reversible adhesion to real-world materials that contain roughness, such as the fields of soft robotics, biomaterials, and pick-and-place manufacturing. Thus, using multi-scale PSD and modified Persson-Tosatti model adhesion can predicted and modified using changing the surface topography and chemistry.

A vital part of the future for this study is to apply this research to get similar understanding of adhesion of hard contacts, which is mainly applicable for MEMS device and micromanufacturing. This research will also help in tailoring surfaces by modifying small scale roughness which may be able to enhance or reduce different roughness dependent contact properties and also to get a better understanding of them.

Appendix A Additional Details on the Characterization of Surface Topography of the Nanodiamond Substrates.

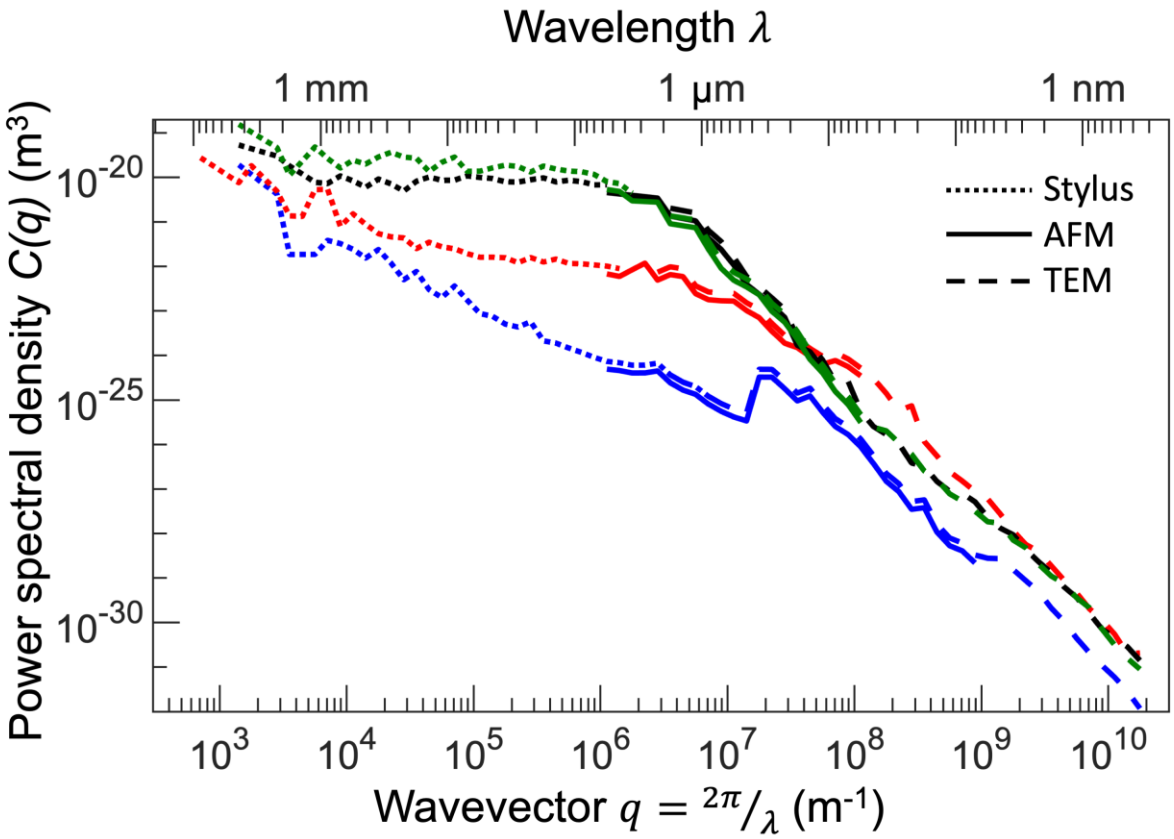

Appendix Figure 1 Power spectral densities of the four surfaces, with indication of the specific regimes of applicability of each technique. The curves on this plot represent the identical data to Fig. 15 of the main text, however the present figure uses line style (solid, dashed, dotted) to indicate the specific bandwidth over which different techniques were applied. Because of the nature of tip artifacts, the minimum size from stylus and AFM data differ between surfaces. Image reproduced from Ref.[45], copyright National Academy of Science, 2019.

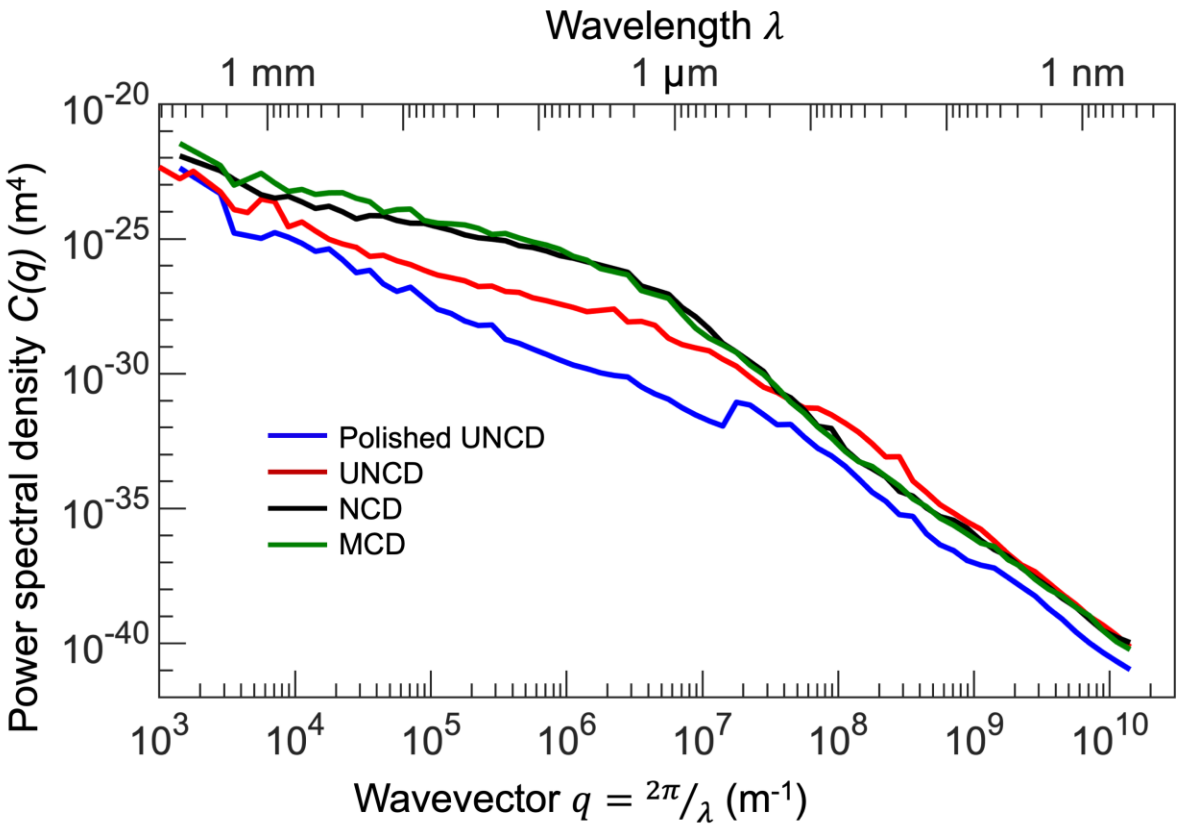

Appendix Figure 2 2D power spectral densities, after conversion from the 1D values shown in Fig. 15 of the main text. Image reproduced from Ref.[45], copyright National Academy of Science, 2019.

Appendix Table 1 2D RMS parameters for nanodiamond substrates. Table reproduced from Ref.[45], copyright National Academy of Science, 2019.

	Polished UNCD	UNCD	NCD	MCD
RMS height	4.6 ± 0.8 nm	23.4 ± 1.3 nm	121.7 ± 13.4 nm	126.6 ± 8.2 nm
RMS slope	0.39 ± 0.04	1.46 ± 0.36	1.15 ± 0.13	1.07 ± 0.13
RMS curvature	1.13 ± 0.23 nm^{-1}	3.37 ± 0.69 nm^{-1}	3.19 ± 1.15 nm^{-1}	2.83 ± 0.81 nm^{-1}

Appendix B A Mathematical Basis for the q^{-4} Scaling of the PSD Above the Grain Size

Consider a triangular peak $y_p(x)$:

$$y_p(x) = \begin{cases} h\,\dfrac{x - x_l}{x_c - x_l}, x_l \le x < x_c \\ h\left(1 - \dfrac{x - x_c}{x_r - x_c}\right), \quad x_c \le x \le x_r \\ 0, \quad else \end{cases} \qquad \text{B-1}$$

where x_l and x_r are left and right bounds of the interpolation function and x_c is the position of the peak of the triangle.

The Fourier transformation of the peak profile $y_p(x)$ is:

$$\begin{aligned} \tilde{y}_p(\mathrm{q}) &= \frac{h}{q^2}\, e^{-iqx_c}\left(\frac{1 - \mathrm{e}^{-i(x_r - x_c)\,q}}{x_r - x_c} + \frac{1 - \mathrm{e}^{i(x_c - x_l)\,q}}{x_c - x_l}\right) y_p(x) \\ &= \begin{cases} h\,\dfrac{x - x_l}{x_c - x_l}, x_l \le x < x_c \\ h\left(1 - \dfrac{x - x_c}{x_r - x_c}\right), \quad x_c \le x \le x_r \\ 0, \quad else \end{cases} \end{aligned} \qquad \text{B-2}$$

For $q \ll \min\left(\frac{\pi}{2\,(x_r - x_c)}, \frac{\pi}{2(x_c - x_l)}\right)$

$$\tilde{y}_p(q) \simeq \frac{h}{2}(x_r - x_l)\, e^{-iqx_c} \qquad \text{B-3}$$

So, for q below this value the PSD $C^{1D}(q) \propto |\tilde{y}(q)|^2$ of the peak reaches a plateau and above it oscillates with an amplitude decaying as q^{-4}.

A piecewise linear function $y(x)$ with kinks at (x_k, h_k) is a superposition of these peaks. Its Fourier transform is:

$$\tilde{y}(q) = \sum_{k=0}^{n-1} \frac{h_k}{q^2}\, e^{-iqx_k} \left(\frac{1 - \mathrm{e}^{-i(x_{k+1} - x_k)\, q}}{x_{k+1} - x_k} + \frac{1 - \mathrm{e}^{i(x_k - x_{k-1})\, q}}{x_k - x_{k-1}} \right) \qquad \text{B-4}$$

$h_n = h_0$ ensures continuity at the periodic boundary.

For $q \ll \min_k \frac{\pi}{2\,(x_{k+1} - x_k)}$, $\tilde{y}(q) \simeq \sum_{k=0}^{n-1} \frac{h_k (x_{k+1} - x_k)}{2}\, e^{-iqx_k}$ and the PSD is certainly flat. Fig 17c shows that for the example profiles considered, the PSD already changes from flat to $\propto q^{-4}$ around $q_k = \frac{\pi}{2 l_k}$, with l_k the mean spacing of the kinks.

Appendix C PDMS Sphere Synthesis

The smooth, soft elastic hemispheres were composed of cross-linked PDMS. To achieve systematic variation in modulus, we have used simple network theory, where changing the crosslinking molecular weight changes the crosslinking density and subsequently elastic modulus [99,107], $E \sim \rho RT/M_c$, where ρ is the density of the polymer, R is the gas constant, T is the temperature in Kelvin and M_c is the cross-linked molecular weight. The curing system consisted of materials obtained from Gelest Inc.: vinyl-terminated PDMS of different molecular weights M_w (DMS V-05 (M_w=800 gm/mol), V-21 (M_w=9000 gm/mol), V-31 (M_w=28000 gm/mol) and V-41 (M_w=62700 gm/mol)); tetrakis-dimethylsiloxysilane (SIT 7278.0) as tetra-functional cross-linker; platinum carbonyl cyclo-vinyl methyl siloxane complex (SIP 6829.2) as catalyst; 1,3,5,7-tetravinyl-1,3,5,7-tetramethyl cyclo-tetra siloxane (SIT 7900.0) as inhibitor. The vinyl-to-hydride molar ratio of 4.4 was maintained for all the samples avoiding excess cross-linker evaporation to minimize adhesion hysteresis from unreacted side chains as reported by Perutz *et al.* [108] The catalyst was added as 0.1% of the total batch. An additional reaction inhibitor was added to the DMS V-05 batch to avoid early cross-linking (5 times the catalyst amount). Hemispherical lenses were cast on the bottom of fluorinated glass dishes using a needle and a syringe. Since the PDMS mixture has a higher surface energy than the fluorinated surface, the drops maintain a contact angle on the surface giving a shape of a hemispherical lens. These lenses were imaged in profile using an optical microscope and could be fit easily with a three-point circle to extract the necessary radius. They were cured at 60 °C for 3 days in a heating oven and Soxhlet-extracted using toluene at 124 °C for 24 hours. After 12 hours of drying in open air, the hemispheres were dried under vacuum at 120 °C overnight. The sol fraction for all of the batches was found to be less than 5%.

The fluorinated dishes were prepared by growing a monolayer of heptadecafluoro 1,1,2,2 tetrahydrodecatrichloro silane on clean base-bath-treated borosilicate glass petri-dishes. The octadecyltrichlorosilane (OTS) monolayer was prepared on silicon wafers (obtained from Silicon Inc.), that had been pre-treated with piranha solution (3:7 ratio of 30% hydrogen peroxide: sulfuric acid (concentrated)). Silicon wafers were cleaned with an ample amount of water before use. The wafers were blown dry with nitrogen and plasma-treated before dipping in 1 wt.% OTS solution in toluene under nitrogen purge for 8 hours. The static water contact angle obtained was 110° ± 2° with negligible contact-angle hysteresis.

*Note - Portions of the text have been taken (with or without modification) from my publications:

1. Dalvi, S.*; Gujrati, A.*; Khanal, S. R.; Pastewka, L.; Dhinojwala, A.; Jacobs, T. D. B. Linking Energy Loss in Soft Adhesion to Surface Roughness. Proc. Natl. Acad. Sci. U.S.A. **2019**, *116* (51), 25484-25490. © National Academy of Sciences, 2019.

Appendix D *In Situ* Contact Experiment and Analysis

A schematic of the experimental test setup is shown in Appendix Fig. 3.

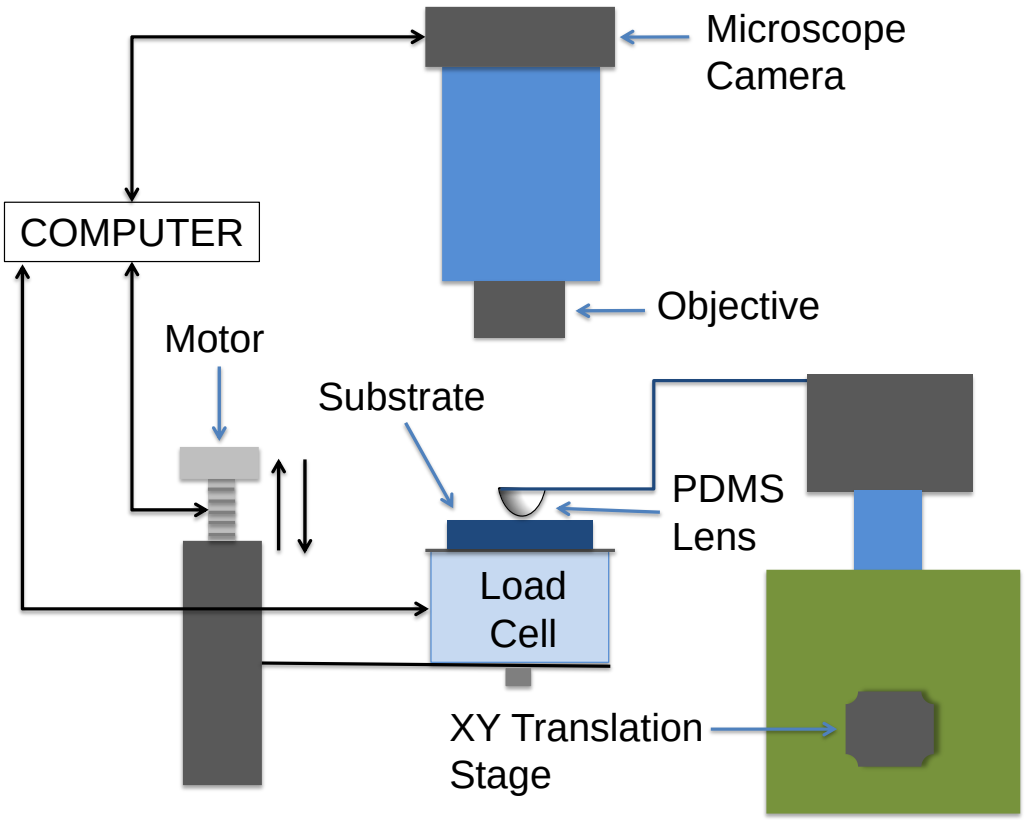

Appendix Figure 3 Schematic of the in-situ apparatus used to measure work of adhesion and elastic modulus.

Image reproduced from Ref.[45], copyright National Academy of Science, 2019.

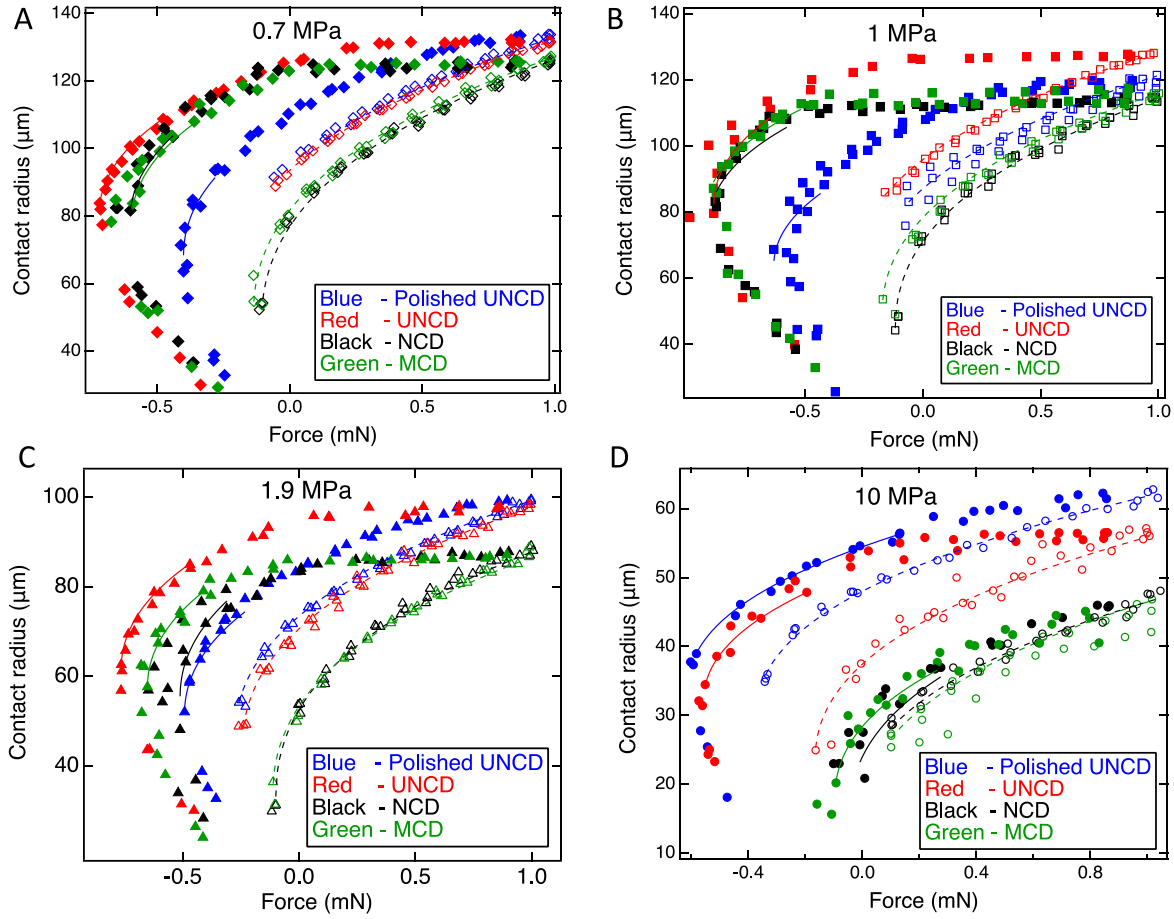

Appendix Figure 4 Contact radius was measured as a function of applied force plots for PDMS spheres with elastic modulus of 0.7 MPa (A), 1 MPa (B), 1.9 MPa (C), and 10 MPa (D). The loading data are represented using hollow symbols and are fit using Eq. 6-1 (dashed line) to extract the apparent work of adhesion $\boldsymbol{W_{app}}$. The separation data are represented using filled symbols; a subset of the data is fit using Eq. D-1 (solid line) to extract $\boldsymbol{W_{app,ret}}$. Images A,B, C and D reproduced from Ref.[45], copyright National Academy of Science, 2019.

As mentioned in the main text, the retraction portions of the experiments on the nanodiamond substrate *do not* follow the trends of the JKR model. However, values of the work of adhesion on retraction $W_{app,ret}$ can be extracted by force-fitting the JKR model to the data. This can be done in one of two ways. First, the work of adhesion can be calculated using the simple JKR equation for the theoretical value of maximum pull-off force F_{po}, which is[86]:

$$F_{po} = -\frac{3}{2}\pi R W_{\text{app,ret}} \qquad \text{D-1}$$

Alternatively, the JKR equation can be rearranged to be a function of F_{po}, and this equation can be fit to the both approach and retraction data[118]:

$$a = \left[\frac{3RF_{po}}{4E^*}\left(\frac{F}{F_{po}} + 2 + 2\left\{\frac{F}{F_{po}} + 1\right\}^{1/2}\right)\right]^{1/3} \qquad \text{D-2}$$

While this function cannot be fit to the entire unloading portion, it can be fit to several points near the point of pull-off. Both of these two approaches (Eqs. D-1 and D-2) yield similar values for $W_{app,ret}$, as shown in Appendix Table 2.

Appendix Table 2 Comparison of different work of adhesion values for nanodiamond substrates. Table reproduced from Ref.[45], copyright National Academy of Science, 2019.

Work of Adhesion upon Approach (in mJ/m^2)				
Substrate	E = 0.69 ± 0.02 MPa	E= 1.03 ± 0.02 MPa	E = 1.91 ± 0.11 MPa	E = 10.03 ± 0.88 MPa
PUNCD	41.41 ± 0.86	41.91 ± 10.97	45.82 ± 1.92	59.55 ± 1.82
UNCD	38.82 ± 2.81	42.22 ± 4.66	40.28 ± 3.28	23.15 ± 5.46
NCD	21.73 ± 0.60	19.64 ± 0.86	17.47 ± 2.15	8.37 ± 1.12
MCD	23.49 ± 1.97	24.98 ± 3.39	17.60 ± 0.79	4.06 ± 1.46
Work of Adhesion from Pull-off using Eq. D-1 (in mJ/m^2)				
PUNCD	74.73 ± 2.58	87.97 ± 2.31	83.04 ± 2.00	102.01 ± 0.96
UNCD	153.03 ± 2.46	147.60 ± 17.10	131.65 ± 0.98	94.40 ± 1.29
NCD	118.26 ± 5.07	142.02 ± 5.76	100.87 ± 10.65	17.18 ± 4.74
MCD	120.03 ± 8.19	144.95 ± 7.26	116.01 ± 3.43	21.38 ± 4.99
Work of Adhesion upon Retraction using Eq. D-2 (in mJ/m^2)				
PUNCD	72.67 ± 2.2	95.2 ± 6.8	80.65 ± 1.72	94.4 ± 1.35
UNCD	131.67 ± 1.7	143.93 ± 16.3	128.43 ± 0.06	88.21 ± 1.18
NCD	116.2 ± 5.76	144.01 ± 2.27	97.82 ± 11.5	13.76 ± 5.7
MCD	118.74 ± 8.7	142.45 ± 7.38	113.39 ± 3.71	19.0 ± 5.22

Testing PDMS for adhesion hysteresis

As mentioned in the main text, to test for adhesion hysteresis due to material viscoelasticity, the PDMS spheres were tested against a smooth silicon wafer coated with a low-surface energy octadecyltrichlorosilane (OTS) monolayer. The results are shown in Appendix Fig. 5 and quantified in Appendix Table 3.

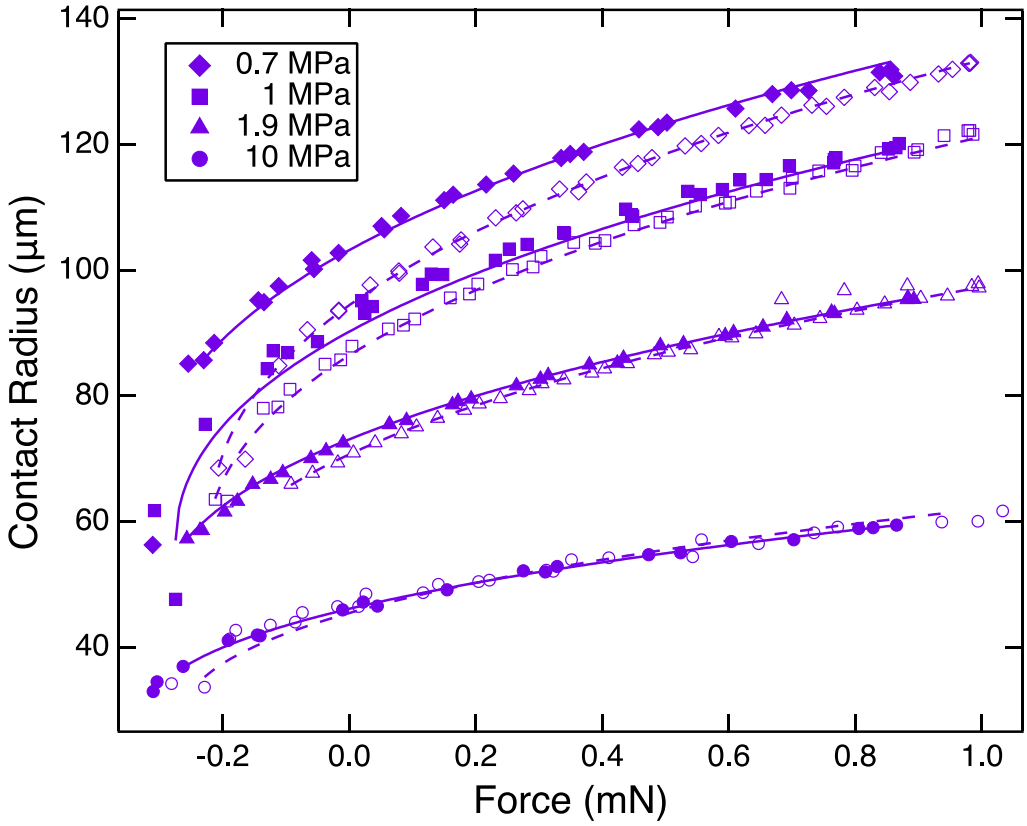

Appendix Figure 5 The contact radius data for the PDMS hemispheres on the OTS surface show low hysteresis between loading (empty symbols) and unloading (filled symbols). The dashed lines indicate JKR model fits for loading and solid lines indicate the JKR model fits for unloading. Image reproduced from Ref.[45], copyright National Academy of Science, 2019.

Appendix Table 3 Work of adhesion and excess energy measurements for the OTS reference substrate. Table reproduced from Ref.[45], copyright National Academy of Science, 2019.

Mc (gm/mol)	$W_{PDMS-OTS}$ (approach) (mJ/m^2)	Elastic Modulus (MPa)	$W_{PDMS-OTS}$ (retraction) (mJ/m^2)	Excess Energy (nJ)
800	51.0 ± 4.8	10.0 ± 0.9	56.4 ± 1.8	1.59 ± 0.91
6000	38.8 ± 2.9	1.9 ± 0.1	52.2 ± 1.3	0.45 ± 0.45
28000	36.8 ± 0.8	1.0 ± 0.0	52.5 ± 4.8	0.49 ± 0.29
62700	39.6 ± 1.2	0.7 ± 0.0	59.3 ± 1.0	0.38 ± 0.02

*Note - Portions of the text have been taken (with or without modification) from my publications:

1. Dalvi, S.*; Gujrati, A.*; Khanal, S. R.; Pastewka, L.; Dhinojwala, A.; Jacobs, T. D. B. Linking Energy Loss in Soft Adhesion to Surface Roughness. Proc. Natl. Acad. Sci. U.S.A. **2019**, *116* (51), 25484-25490. © National Academy of Sciences, 2019.

Appendix E Deriving an Expression for the Increase in Surface Area due to Roughness for Large Slopes.

Prior work (e.g. Ref. [34]) has derived expressions for $A_{\mathrm{true}}/A_{\mathrm{app}}$ in the limit of small slopes. Here, we derive an expression for $A_{\mathrm{true}}/A_{\mathrm{app}}$ that works for arbitrary values of slope h'_{rms}. The derivation follows along the arguments given in the Supplementary Material of Ref. [47].

For a full two-dimensional topography map $h(x,y)$, the surface area A_{true} is straightforwardly obtained from an expression analogous to the arc length of a function:

$$A_{\mathrm{true}} = \int_{A_{\mathrm{app}}} \sqrt{1+|\nabla h|^2}\,dxdy = \int_{A_{\mathrm{app}}} \sqrt{1+\left(\frac{\partial h}{\partial x}\right)^2+\left(\frac{\partial h}{\partial y}\right)^2}\,dxdy \qquad \text{E-1}$$

For small slopes $|\nabla h|$, the square-root can be expanded into a Taylor series and truncated above quadratic order. This gives the well-known expression [34]:

$$A_{\text{true}} \approx \int_{A_{\text{app}}} \left(1 + \frac{1}{2}|\nabla h|^2\right) dxdy = A_{\text{app}} \left(1 + \frac{1}{2} h'^2_{\text{rms}}\right) \quad \text{E-2}$$

with

$$A_{\text{true}} \approx \int_{A_{\text{app}}} \left(1 + \frac{1}{2}|\nabla h|^2\right) dxdy = A_{\text{app}} \left(1 + \frac{1}{2} h'^2_{\text{rms}}\right) \quad \text{E-3}$$

In order to arrive at an expression valid for large h'_{rms}, we now transform the integral over the surface area into an integral over slopes. We first define the slope distribution function,

$$\phi(s_x, s_y) = \frac{1}{A_{\text{app}}} \int_{A_{\text{app}}} \delta\left(s_x - \frac{\partial h(x,y)}{\partial x}\right) \delta\left(s_y - \frac{\partial h(x,y)}{\partial y}\right) dxdy \quad \text{E-4}$$

where $\delta(x)$ is the Dirac delta function. Note that using the slope distribution function, we can express the integral over any function *f* that depends on just slopes as

$$\int_{A_{\text{app}}} f\left(\frac{\partial h}{\partial x}, \frac{\partial h}{\partial y}\right) dxdy = A_{\text{app}} \int \phi(s_x, s_y) f(s_x, s_y) ds_x ds_y \quad \text{E-5}$$

We can hence re-express Eq. E-1 as:

$$\frac{A_{\text{true}}}{A_{\text{app}}} = \int \phi(s_x, s_y)\sqrt{1 + s_x^2 + s_y^2}\, ds_x ds_y \qquad \text{E-6}$$

We now make the assumption that our surfaces are isotropic and Gaussian. The slope distribution function is then given by

$$\phi(s_x, s_y) = \frac{1}{\pi h'^2_{\text{rms}}} \exp\left(-\frac{s_x^2 + s_y^2}{h'^2_{\text{rms}}}\right) \qquad \text{E-7}$$

with (see also Eq. E-3)

$$h'^2_{\text{rms}} = \int_{A_{\text{app}}} |\nabla h|^2 dx dy = \int \phi(s_x, s_y)(s_x^2 + s_y^2) ds_x ds_y \qquad \text{E-8}$$

Evaluating Eq. E-4 using this slope distribution function yields

$$\frac{A_{\text{true}}}{A_{\text{app}}} = \frac{2}{h'^2_{\text{rms}}} \int_0^\infty \exp\left(-\frac{s^2}{h'^2_{\text{rms}}}\right) \sqrt{1+s^2}\, sds = 1 + \frac{1}{2} h'^2_{\text{rms}} g(h'_{\text{rms}}) \qquad \text{E-9}$$

with

$$g(h'_{\text{rms}}) = \sqrt{\pi} \exp\left(\frac{1}{h'^2_{\text{rms}}}\right) \text{erfc}\left(\frac{1}{h'_{\text{rms}}}\right) / h'_{\text{rms}} \qquad \text{E-10}$$

Equation E-9 is Eq. 6-10 from the main text. Note that the left-hand side of Eq. E-9 is Eq. B1 from Ref.[34]. The function $g(h'_{\text{rms}})$ can be regarded a correction to the small slope approximation Eq. E-2. It has the property $g(h'_{\text{rms}}) \to 1$ as $h'_{\text{rms}} \to 0$ and hence we recover Eq. E-2 from Eq. E-9 in the small slope limit. Appendix figure 6A shows the function g up to slope of 5. Note that for slope of order unity, $g(1) \approx 0.76$ and hence the small-slope approximation Eq. E-2 would overestimate the area by 30%.

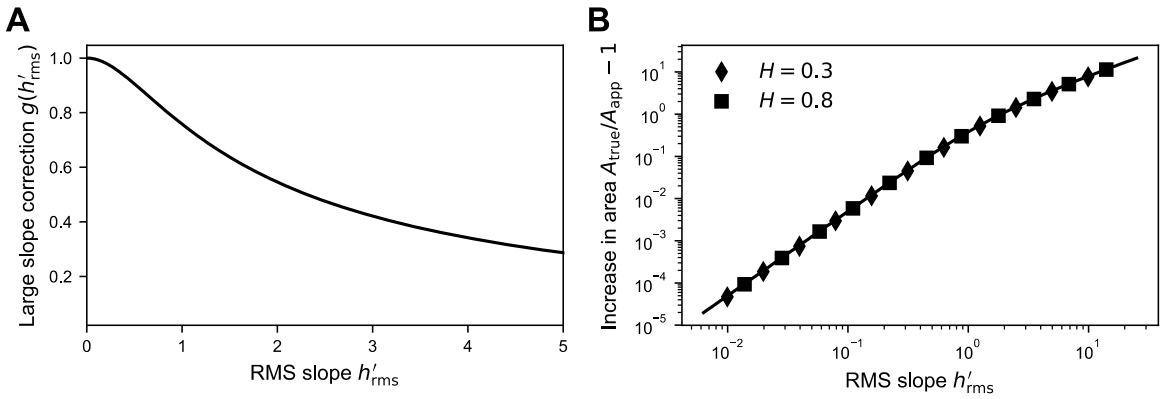

Appendix Figure 6 Plot of the correction g(h'_{rms}) to the small-slope approximation. For values of g(h'_{rms}) ≈ 1 the small slope approximation is valid (A) Validation of Eq. E-9 using computer-generated self-affine surfaces with varying RMS slope h'_{rms} and Hurst exponents *H.* (B) The solid line shows the analytic result given by Eq. E-9. Images A and B reproduced from Ref.[45], copyright National Academy of Science, 2019.

In order to numerically test the validity of Eq. A15, we have created a range of synthetic self-affine surfaces with 4096 x 4096 points and Hurst exponent H = 0.3 and 0.8 using a Fourier filtering algorithm [17,73]. We then computed the true surface area by numerical integration of Eq. E-2. Appendix figure 6B shows that the analytic expression Eq. E-9 describes the synthetic surfaces excellently up to slopes of order 10.

*Note - Portions of the text have been taken (with or without modification) from my publications:

1. Dalvi, S.*; Gujrati, A.*; Khanal, S. R.; Pastewka, L.; Dhinojwala, A.; Jacobs, T. D. B. Linking Energy Loss in Soft Adhesion to Surface Roughness. Proc. Natl. Acad. Sci. U.S.A. **2019**, *116* (51), 25484-25490. © National Academy of Sciences, 2019.

Appendix F Calculating Work of Adhesion Without Accounting for the Change in Area of the Soft Material

The original model by Persson and Tosatti[34] leads to an equation for W_{app} in terms of topography:

$$W_{\text{app}} = W_{\text{int}}\left\{\left[1 + \frac{1}{4\pi}\int_{q_0}^{q_1} dq q^3 C^{iso}(q)\right] - \left[\frac{E}{8\pi(1-\nu^2)W_{int}}\int_{q_0}^{q_1} dq q^2 C^{iso}(q)\right]\right\} \quad \text{F-1}$$

where q_0 is the long-wavelength (small-wavevector) cut-off and q_1 is the short-wavelength (large-wavevector) cut-off of the topography. Note that, as described in Ref.[17], C^{iso} differs by a constant prefactor from the PSD definition used by Persson and Tosatti, arising from different conventions used in the Fourier transform. Therefore, the prefactors in Eq. F-1 differ from those in Ref.[34]. These differences can be reconciled by acknowledging[17] that $C^{Persson}(q) = C^{iso}(q)/4\pi^2$. In Ref.[34], Eq. F-1 is further simplified for self-affine surfaces. However, in this study we have directly used the integral equations because the surfaces are not self-affine overall length-scales.

To calculate W_{app} using the combined PSD from the model, Eq. F-1 was integrated using the data in Appendix fig. 2. The wavevector cutoffs were set as the maximum and minimum measured values (q_0 = 1.3 x 10^3 m^{-1} and q_1 = 1.6 x 10^{10} m^{-1}). Appendix figure 7 shows the experimentally measured values of W_{app} compared against the predictions of Eq. F-1. The best fit was obtained using W_{int} = 25 mJ/m^2.

The proposed model (main text) is considered to more accurately describe the present data as compared to the Persson-Tosatti model for three reasons: first, it more accurately accounts for the change in area of the PDMS; second, the fit to the data is better (R^2 = 0.29 for the Persson-Tosatti model and R^2 = 0.67 for the proposed model); and third, the extracted value from the proposed model is a closer match to the intrinsic work of adhesion measured upon retraction.

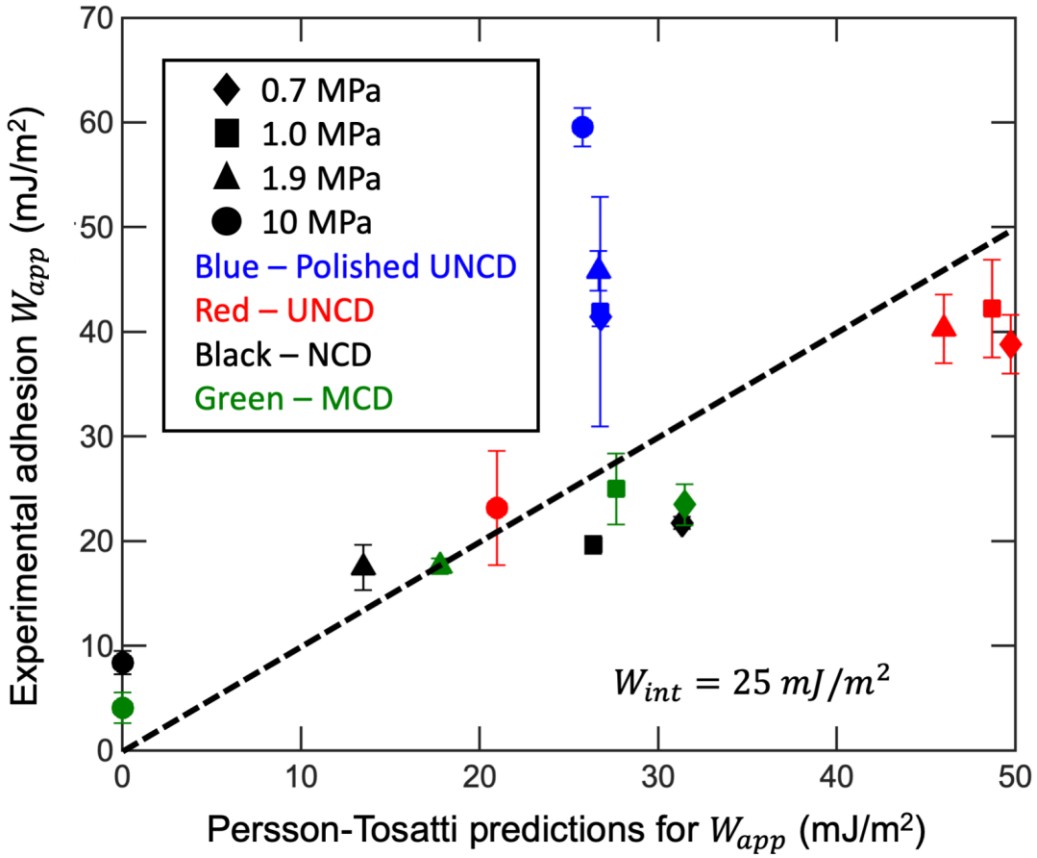

Appendix Figure 7 The experimental measurements of W_appcan be compared against the unmodified Persson-Tosatti model, which does not account for the change in area of the soft elastomer. Image reproduced from Ref.[45], copyright National Academy of Science, 2019.

*Note - Portions of the text have been taken (with or without modification) from my publications:

1. Dalvi, S.*; Gujrati, A.*; Khanal, S. R.; Pastewka, L.; Dhinojwala, A.; Jacobs, T. D. B. Linking Energy Loss in Soft Adhesion to Surface Roughness. Proc. Natl. Acad. Sci. U.S.A. **2019**, *116* (51), 25484-25490. © National Academy of Sciences, 2019.

Bibliography

(1) Binder, L. Der Widerstand von Kontakten. *Elektrotech. Maschinenbau* **1912**, *30* (September), 781–782.

(2) Israelachvili, J. N. *Intermolecular and Surface Forces*; Academic Press: London ; San Diego, 1991.

(3) Maugis, D. *Contact, Adhesion and Rupture of Elastic Solids*, 1st ed.; Springer: Berlin, Heidelberg: New York, 1999.

(4) Bush, A. W.; Gibson, R. D.; Thomas, T. R. The Elastic Contact of a Rough Surface. *Wear* **1975**, *35*, 87–111.

(5) Maugis, D. On the Contact and Adhesion of Rough Surfaces. *J. Adhes. Sci. Technol.* **1996**, *10* (2), 161–175. https://doi.org/10.1163/156856196X00832.

(6) Persson, B. N. J.; Albohr, O.; Tartaglino, U.; Volokitin, A. I.; Tosatti, E. On the Nature of Surface Roughness with Application to Contact Mechanics, Sealing, Rubber Friction and Adhesion. *J. Phys. Condens. Matter* **2005**, *17* (1). https://doi.org/10.1088/0953-8984/17/1/R01.

(7) Persson, B. N. J. Adhesion between Elastic Bodies with Randomly Rough Surfaces. *Phys. Rev. Lett.* **2002**, *89* (24), 245502. https://doi.org/10.1103/PhysRevLett.89.245502.

(8) Pastewka, L.; Robbins, M. O. Contact between Rough Surfaces and a Criterion for Macroscopic Adhesion. *Proc. Natl. Acad. Sci.* **2014**, *111* (9), 3298 LP – 3303. https://doi.org/10.1073/pnas.1320846111.

(9) ISO 4287:1997 Geometrical Product Specifications (GPS) — Surface Texture: Profile Method — Terms, Definitions and Surface Texture Parameters. ISO: Geneva.

(10) Samavedi, S.; Whittington, A. R.; Goldstein, A. S. Calcium Phosphate Ceramics in Bone Tissue Engineering: A Review of Properties and Their Influence on Cell Behavior. *Acta Biomater.* **2013**, *9* (9), 8037–8045. https://doi.org/10.1016/j.actbio.2013.06.014.

(11) Mandelbrot, B. B. How Long Is the Coast of Britain? Statistical Self-Similarity and Fractional Dimension. *Science* **1967**, *156* (3775), 636–638.

(12) Sayles, R. S.; Thomas, T. R. Surface Topography as a Nonstationary Random Process. *Nature* **1978**, *271* (5644), 431–434. https://doi.org/10.1038/271431a0.

(13) Persson, B. N. J.; Scaraggi, M. Theory of Adhesion: Role of Surface Roughness. *J. Chem. Phys.* **2014**, *124701* (12), 124701–124715. https://doi.org/10.1063/1.4895789.

(14) Campañá, C.; Müser, M. H. Contact Mechanics of Real vs. Randomly Rough Surfaces: A Green's Function Molecular Dynamics Study. *Europhys. Lett.* **2007**, *77*, 38005.

(15) Putignano, C.; Afferrante, L.; Carbone, G.; Demelio, G. The Influence of the Statistical Properties of Self-Affine Surfaces in Elastic Contacts: A Numerical Investigation. *J. Mech. Phys. Solids* **2012**, *60* (5), 973–982. https://doi.org/10.1016/j.jmps.2012.01.006.

(16) Müser, M. H.; Dapp, W. B.; Bugnicourt, R.; Sainsot, P.; Lesaffre, N.; Lubrecht, T. A.; Persson, B. N. J.; Harris, K.; Bennett, A.; Schulze, K.; et al. Meeting the Contact-Mechanics Challenge. *Tribol. Lett.* **2017**, *65* (4), 118. https://doi.org/10.1007/s11249-017-0900-2.

(17) Jacobs, T. D. B.; Junge, T.; Pastewka, L. Quantitative Characterization of Surface Topography Using Spectral Analysis. *Surf. Topogr. Metrol. Prop.* **2017**, *5* (1), 013001. https://doi.org/10.1088/2051-672X/aa51f8.

(18) Wang, A.; Martin, H. M. On the Usefulness of the Height-Difference-Autocorrelation Function for Contact Mechanics. *Tribol. Int.* **2017**, *123*, 224–233. https://doi.org/10.1016/j.triboint.2018.02.002.

(19) Greenwood, J. A.; Williamson, J. B. P. Contact of Nominally Flat Surfaces. *Proc. R. Soc. London A Math. Phys. Eng. Sci.* **1966**, *295* (1442), 300–319.

(20) Campañá, C.; Müser, M. H.; Robbins, M. O. Elastic Contact between Self-Affine Surfaces: Comparison of Numerical Stress and Contact Correlation Functions with Analytic Predictions. *J. Phys. Condens. Matter* **2008**, *20* (35), 354013.

(21) Stover, J. C. *Optical Scattering: Measurement and Analysis*, Second.; SPIE: 1000 20th Street, Bellingham, WA 98227-0010 USA, 1995. https://doi.org/10.1117/3.203079.

(22) Khanal, S. R.; Gujrati, A.; Vishnubhotla, S. B.; Nowakowski, P.; Bonifacio, C.; Pastewka, L.; Jacobs, T. D. B. Characterizing Small-Scale Topography Using Transmission Electron Microscopy. *Surf. Topogr. Metrol. Prop.* **2018**, *6* (4), 45004.

(23) Carim, A. H.; Sinclair, R. The Evolution of Si / SiO2 Interface Roughness. *J. Electrochem. Soc.* **1987**, *134* (3), 741–746. https://doi.org/10.1149/1.2100544.

(24) Lim, J.; Hippalgaonkar, K.; Andrews, S. C.; Majumdar, A.; Yang, P. Quantifying Surface Roughness Effects on Phonon Transport in Silicon Nanowires. *Nano Lett* **2012**, *12* (5), 2475–2482. https://doi.org/10.1021/nl3005868.

(25) Goodnick, S. M.; Ferry, D. K.; Wilmsen, C. W.; Liliental, Z.; Fathy, D.; Krivanek, O. L. Surface Roughness at the Si(100)-SiO2 Interface. *Phys. Rev. B* **1985**, *32* (12), 8171–8186. https://doi.org/10.1103/PhysRevB.32.8171.

(26) Zhao, Y.; Matsumoto, H.; Sato, T.; Koyama, S.; Takenaka, M.; Takagi, S. A Novel Characterization Scheme of Si/SiO2 Interface Roughness for Surface Roughness Scattering-Limited Mobilities of Electrons and Holes in Unstrained- and Strained-Si MOSFETs. *IEEE Trans. Electron Devices* **2010**, *57* (9), 2057–2066. https://doi.org/10.1109/TED.2010.2052394.

(27) Williams, D. B.; Carter, C. B. *Transmission Electron Microscopy: A Textbook for Materials Science*; Springer, 2009.

(28) Strecker, A.; Bäder, U.; Kelsch, M.; Salzberger, U.; Sycha, M.; Gao, M.; Richter, G.; van Benthem, K. Progress in the Preparation of Cross-Sectional TEM Specimens by Ion-Beam Thinning. *Zeitschrift für Met.* **2003**, *94* (3), 290–297.

(29) Fuller, K. N. G.; David, T. The Effect of Surface Roughness on the Adhesion of Elastic Solids. *Proc. R. Soc. London. A. Math. Phys. Sci.* **1975**, *345* (1642), 327–342. https://doi.org/10.1098/rspa.1975.0138.

(30) Etsion, I.; Front, I. A Model for Static Sealing Performance of End Face Seals. *Tribol. Trans.* **1994**, *37* (1), 111–119. https://doi.org/10.1080/10402009408983273.

(31) Polycarpou, A. A.; Etsion, I. Analytical Approximations in Modeling Contacting Rough Surfaces. *J. Tribol.* **1999**, *121* (2), 234–239.

(32) Liu, Z.; Neville, A.; Reuben, R. L. An Analytical Solution for Elastic and Elastic-Plastic Contact Models. *Tribol. Trans.* **2000**, *43* (4), 627–634. https://doi.org/10.1080/10402000008982387.

(33) McCool, J. I. Comparison of Models for the Contact of Rough Surfaces. *Wear* **1986**, *107* (1), 37–60. https://doi.org/https://doi.org/10.1016/0043-1648(86)90045-1.

(34) Persson, B. N. J.; Tosatti, E. The Effect of Surface Roughness on the Adhesion of Elastic Solids. *J. Chem. Phys.* **2001**, *115* (12), 5597. https://doi.org/10.1063/1.1398300.

(35) Dieterich, J. H.; Kilgore, B. D. Imaging Surface Contacts: Power Law Contact Distributions and Contact Stresses in Quartz, Calcite, Glass and Acrylic Plastic. *Tectonophysics* **1996**, *256* (1), 219–239. https://doi.org/https://doi.org/10.1016/0040-1951(95)00165-4.

(36) Hyun, S.; Pei, L.; Molinari, J.-F.; Robbins, M. O. Finite-Element Analysis of Contact between Elastic Self-Affine Surfaces. *Phys. Rev. E* **2004**, *70* (2), 26117. https://doi.org/10.1103/PhysRevE.70.026117.

(37) Amontons, G. De La Resistance Causée Dans Les Machines. *Mem. Acad. R.* **1699**, 275–282.

(38) Bowden, F. P.; Tabor, D. *The Friction and Lubrication of Solids*; Oxford University Press, 1950.

(39) Zhang, B. N. J. P. and I. M. S. and V. N. S. and K. Z. and A. I. V. and Z. On the Origin of Amonton's Friction Law. *J. Phys. Condens. Matter* **2008**, *20* (39), 395006.

(40) Peressadko, A. G.; Hosoda, N.; Persson, B. N. J. Influence of Surface Roughness on Adhesion between Elastic Bodies. *Phys. Rev. Lett.* **2005**, *95* (12), 124301. https://doi.org/10.1103/PhysRevLett.95.124301.

(41) Persson, B. N. J. Capillary Adhesion between Elastic Solids with Randomly Rough Surfaces. *J. Phys. Condens. Matter* **2008**, *20* (31), 315007.

(42) Persson, M. S. and B. N. J. Friction and Universal Contact Area Law for Randomly Rough Viscoelastic Contacts. *J. Phys. Condens. Matter* **2015**, *27* (10), 105102.

(43) Zeng, H.; Konicek, A. R.; Moldovan, N.; Mangolini, F.; Jacobs, T. D. B.; Wylie, I.; Arumugam, P. U.; Siddiqui, S.; Carpick, R. W.; Carlisle, J. A. Boron-Doped Ultrananocrystalline Diamond Synthesized with an H-Rich/Ar-Lean Gas System. *Carbon N. Y.* **2015**, *84* (1), 103–117. https://doi.org/10.1016/j.carbon.2014.11.057.

(44) Auciello, O.; Pacheco, S.; Sumant, A. V.; Gudeman, C.; Sampath, S.; Datta, A.; Carpick, R. W.; Adiga, V. P.; Zurcher, P.; Ma, Z.; et al. Are Diamonds a MEMS' Best Friend? *IEEE Microw. Mag.* **2007**, *8* (6), 61–75. https://doi.org/10.1109/MMM.2007.907816.

(45) Dalvi, S.; Gujrati, A.; Khanal, S. R.; Pastewka, L.; Dhinojwala, A.; Jacobs, T. D. B. Linking Energy Loss in Soft Adhesion to Surface Roughness. *Proc. Natl. Acad. Sci.* **2019**, *116* (51), 25484 LP – 25490. https://doi.org/10.1073/pnas.1913126116.

(46) Nayak, P. R. Random Process Model of Rough Surfaces. *J. Lubr. Technol.* **1971**, *93* (3), 398. https://doi.org/10.1115/1.3451608.

(47) Gujrati, A.; Khanal, S. R.; Pastewka, L.; Jacobs, T. D. B. Combining TEM, AFM, and Profilometry for Quantitative Topography Characterization Across All Scales. *ACS Appl. Mater. Interfaces* **2018**, *10* (34), 29169–29178. https://doi.org/10.1021/acsami.8b09899.

(48) Church, E. L.; Takacs, P. Z. Effects of the Nonvanishing Tip Size in Mechanical Profile Measurements. In *Proc. SPIE 1332, Optical Testing and Metrology III: Recent Advances in Industrial Optical Inspection*; 1991; Vol. 1332, pp 504–514. https://doi.org/10.1117/12.51099.

(49) Fukuma, T.; Ichii, T.; Kobayashi, K.; Yamada, H.; Matsushige, K. True-Molecular Resolution Imaging by Frequency Modulation Atomic Force Microscopy in Various Environments. *Appl. Phys. Lett.* **2005**, *86* (3), 1–3. https://doi.org/10.1063/1.1852721.

(50) Podgursky, V.; Bogatov, A.; Sedov, V.; Sildos, I.; Mere, A.; Viljus, M.; Buijnsters, J. G.; Ralchenko, V. Growth Dynamics of Nanocrystalline Diamond Films Produced by Microwave Plasma Enhanced Chemical Vapor Deposition in Methane/Hydrogen/Air Mixture: Scaling Analysis of Surface Morphology. *Diam. Relat. Mater.* **2015**, *58*, 172–179. https://doi.org/10.1016/j.diamond.2015.07.002.

(51) Dychalska, A.; Fabisiak, K.; Paprocki, K.; Makowiecki, J.; Iskaliyeva, A.; Szybowicz, M. A Raman Spectroscopy Study of the Effect of Thermal Treatment on Structural and Photoluminescence Properties of CVD Diamond Films. *Mater. Des.* **2016**, *112*, 320–327. https://doi.org/10.1016/j.matdes.2016.09.092.

(52) Rott, H. The Analysis of Backscattering Properties from SAR Data of Mountain Regions. *IEEE J. Ocean. Eng.* **1984**, *9* (5), 347–355. https://doi.org/10.1109/JOE.1984.1145655.

(53) Schmittbuhl, J.; Vilotte, J.-P.; Roux, S. Reliability of Self-Affine Measurements. *Phys. Rev. E* **1995**, *51* (1), 131–147. https://doi.org/10.1103/PhysRevE.51.131.

(54) Mandelbrot, B. B. Self-Affine Fractals and Fractal Dimension. *Phys. Scr.* **1985**, *32* (4), 257–260. https://doi.org/10.1088/0031-8949/32/4/001.

(55) Mandelbrot, B. B.; van Ness, J. W. Fractional Brownian Motions, Fractional Noises and Applications. *SIAM Rev.* **1968**, *10* (4), 422--437.

(56) Beran, J.; Feng, Y.; Ghosh, S.; Kulik, R. *Long-Memory Processes: Probabilistic Theories and Statistical Methods*; 2013. https://doi.org/10.1007/978-3-642-35512-7.

(57) Gneiting, T.; Schlather, M. Stochastic Models Which Separate Fractal Dimension and Hurst Effect. **2001**, *46* (2), 269–282. https://doi.org/10.1137/S0036144501394387.

(58) Orey, S. Gaussian Sample Functions and the Hausdorff Dimension of Level Crossings. *Zeitschrift für Wahrscheinlichkeitstheorie und Verwandte Gebiete* **1970**, *15* (3), 249–256. https://doi.org/10.1007/BF00534922.

(59) Mandelbrot, B. B. *The Fractal Geometry of Nature*; W. H. Freeman, 1982.

(60) Zhang, X.; Xu, Y.; Jackson, R. L. An Analysis of Generated Fractal and Measured Rough Surfaces in Regards to Their Multi-Scale Structure and Fractal Dimension. *Tribol. Int.* **2017**, *105* (June 2016), 94–101. https://doi.org/10.1016/j.triboint.2016.09.036.

(61) Candela, T.; Renard, F.; Klinger, Y.; Mair, K.; Schmittbuhl, J.; Brodsky, E. E. Roughness of Fault Surfaces over Nine Decades of Length Scales. *J. Geophys. Res. Solid Earth* **2012**, *117* (8), B08409. https://doi.org/10.1029/2011JB009041.

(62) Persson, B. N. J. On the Fractal Dimension of Rough Surfaces. *Tribol. Lett.* **2014**, *54* (1), 99–106. https://doi.org/10.1007/s11249-014-0313-4.

(63) Mandelbrot, B. B.; Passoja, D. E.; Paullay, A. J. Fractal Character of Fracture Surfaces of Metals. *Nature* **1984**, *308*, 721–722. https://doi.org/10.1038/308721a0.

(64) Ponson, L.; Bonamy, D.; Bouchaud, E. Two-Dimensional Scaling Properties of Experimental Fracture Surfaces. *Phys. Rev. Lett.* **2006**, *96*, 035506. https://doi.org/10.1103/PhysRevLett.96.035506.

(65) Bonamy, D.; Ponson, L.; Prades, S.; Bouchaud, E.; Guillot, C. Scaling Exponents for Fracture Surfaces in Homogeneous Glass and Glassy Ceramics. *Phys. Rev. Lett.* **2006**, *97* (13), 135504. https://doi.org/10.1103/PhysRevLett.97.135504.

(66) Zaiser, M.; Grasset, F. M.; Koutsos, V.; Aifantis, E. C. Self-Affine Surface Morphology of Plastically Deformed Metals. *Phys. Rev. Lett.* **2004**, *93* (19), 1–4. https://doi.org/10.1103/PhysRevLett.93.195507.

(67) Edwards, S. F.; Wilkinson, D. R. The Surface Statistics of a Granular Aggregate. *Proc. R. Soc. A Math. Phys. Eng. Sci.* **1982**, *381* (1780), 17–31. https://doi.org/10.1098/rspa.1982.0056.

(68) Kardar, M.; Parisi, G.; Zhang, Y.-C. Dynamic Scaling of Growing Interfaces. *Phys. Rev. Lett.* **1986**, *56* (9), 889.

(69) Yanguas-Gil, A.; Cotrino, J.; Walkiewicz-Pietrzykowska, A.; González-Elipe, A. R. Scaling Behavior and Mechanism of Formation of SiO2 Thin Films Grown by Plasma-Enhanced Chemical Vapor Deposition. *Phys. Rev. B* **2007**, *76* (7), 075314. https://doi.org/10.1103/PhysRevB.76.075314.

(70) Hasan, N. M.; Mallett, J. J.; dos Santos Filho, S. G.; Pasa, A. A.; Schwarzacher, W. Dynamic Scaling of the Surface Roughness of Cu Deposited Using a Chemical Bath. *Phys. Rev. B Condens. Matter* **2003**, *67* (8), 81401.

(71) Technique, E. M.; Cheng, S.; Berkeley, L.; Labor, N. EELS Log-Ratio Technique for Specimen-Thickness Measurement in the TEM. **1988**, No. May 2016, 193–200. https://doi.org/10.1002/jemt.1060080206.

(72) Egerton, R. F. *Electron Energy-Loss Spectroscopy in the Electron Microscope*; Springer Science & Business Media, 2011.

(73) Ramisetti, S. B.; Campañá, C.; Anciaux, G.; Molinari, J.-F.; Müser, M. H.; Robbins, M. O. The Autocorrelation Function for Island Areas on Self-Affine Surfaces. *J. Phys. Condens. Matter* **2011**, *23* (21), 215004. https://doi.org/10.1088/0953-8984/23/21/215004.

(74) Vahdat, V.; Carpick, R. W. Practical Method to Limit Tip À Sample Contact Stress and Prevent Wear in Amplitude Modulation Atomic Force Microscopy. *ACS Nano* **2013**, No. Xx, 9836–9850. https://doi.org/10.1021/nn403435z.

(75) Putignano, C.; Afferrante, L.; Carbone, G.; Demelio, G. The Influence of the Statistical Properties of Self-Affine Surfaces in Elastic Contacts: A Numerical Investigation. *J. Mech. Phys. Solids* **2012**, *60* (5), 973–982. https://doi.org/10.1016/j.jmps.2012.01.006.

(76) Hinkle, A. R.; Nöhring, W. G.; Leute, R.; Junge, T.; Pastewka, L. The Emergence of Small-Scale Self-Affine Surface Roughness from Deformation. *Sci. Adv.* **2020**, *6* (7), eaax0847. https://doi.org/10.1126/sciadv.aax0847.

(77) Ayyildiz, M.; Scaraggi, M.; Sirin, O.; Basdogan, C.; Persson, B. N. J. Contact Mechanics between the Human Finger and a Touchscreen under Electroadhesion. *Proc. Natl. Acad. Sci. U. S. A.* **2018**, *115* (50), 12668–12673. https://doi.org/10.1073/pnas.1811750115.

(78) Niewiarowski, P. H.; Stark, A. Y.; Dhinojwala, A. Sticking to the Story: Outstanding Challenges in Gecko-Inspired Adhesives. *J. Exp. Biol.* **2016**, *219* (7), 912–919. https://doi.org/10.1242/jeb.080085.

(79) Luan, B.; Robbins, M. O. The Breakdown of Continuum Models for Mechanical Contacts. *Nature* **2005**, *435* (7044), 929–932. https://doi.org/10.1038/nature03700.

(80) Jacobs, T. D. B.; Ryan, K. E.; Keating, P. L.; Grierson, D. S.; Lefever, J. A.; Turner, K. T.; Harrison, J. A.; Carpick, R. W. The Effect of Atomic-Scale Roughness on the Adhesion of Nanoscale Asperities: A Combined Simulation and Experimental Investigation. *Tribol. Lett.* **2013**, *50* (1), 81–93. https://doi.org/10.1007/s11249-012-0097-3.

(81) Popa, D. O.; Stephanou, H. E. Micro and Mesoscale Robotic Assembly. *J. Manuf. Process.* **2004**, *6* (1), 52–71. https://doi.org/10.1016/S1526-6125(04)70059-6.

(82) Carlson, A.; Bowen, A. M.; Huang, Y.; Nuzzo, R. G.; Rogers, J. A. Transfer Printing Techniques for Materials Assembly and Micro/Nanodevice Fabrication. *Adv. Mater.* **2012**, *24* (39), 5284–5318. https://doi.org/10.1002/adma.201201386.

(83) Yu, Z.; Cheng, H. Tunable Adhesion for Bio-Integrated Devices. *Micromachines* **2018**, *9* (10), 529. https://doi.org/10.3390/mi9100529.

(84) Tang, Y.; Zhang, Q.; Lin, G.; Yin, J. Switchable Adhesion Actuator for Amphibious Climbing Soft Robot. *Soft Robot.* **2018**, *5* (5), 592–600. https://doi.org/10.1089/soro.2017.0133.

(85) Hertz, H. On the Contact of Rigid Elastic Solids. *J. fur die Reine und Angew. Math.* **1882**. https://doi.org/10.1515/crll.1882.92.156.

(86) Johnson, K. L.; Kendall, K.; Roberts, a. D. Surface Energy and the Contact of Elastic Solids. *Proc. R. Soc. A Math. Phys. Eng. Sci.* **1971**, *324* (1558), 301–313. https://doi.org/10.1098/rspa.1971.0141.

(87) Briggs, G. A. D.; Briscoe, B. J. The Effect of Surface Topography on the Adhesion of Elastic Solids. *J. Phys. D. Appl. Phys.* **1977**, *10* (18), 2453–2466. https://doi.org/10.1088/0022-3727/10/18/010.

(88) Fuller, K. N. G.; Tabor, D. The Effect of Surface Roughness on the Adhesion of Elastic Solids. *Proc. R. Soc. London. A. Math. Phys. Sci.* **1975**, *345* (1642), 327–342. https://doi.org/10.1098/rspa.1975.0138.

(89) Maeda, N.; Chen, N.; Tirrell, M.; Israelachvili, J. N. Adhesion and Friction Mechanisms of Polymer-on-Polymer Surfaces. *Science (80-.).* **2002**, *297* (5580), 379–382. https://doi.org/10.1126/science.1072378.

(90) Luengo, G.; Pan, J.; Heuberger, M.; Israelachvili, J. N. Temperature and Time Effects on the "Adhesion Dynamics" of Poly(Butyl Methacrylate) (PBMA) Surfaces. *Langmuir* **1998**, *14* (14), 3873–3881. https://doi.org/10.1021/la971304a.

(91) Tiwari, A.; Dorogin, L.; Bennett, A. I.; Schulze, K. D.; Sawyer, W. G.; Tahir, M.; Heinrich, G.; Persson, B. N. J. The Effect of Surface Roughness and Viscoelasticity on Rubber Adhesion. *Soft Matter* **2017**. https://doi.org/10.1039/c7sm00177k.

(92) Archard J. F. Elastic Deformation and the Laws of Friction. *Proc. R. Soc. A Math. Phys. Eng. Sci.* **1957**, *243* (1233), 190–205.

(93) Jackson, R. L.; Streator, J. L. A Multi-Scale Model for Contact between Rough Surfaces. *Wear* **2006**, *261* (11–12), 1337–1347. https://doi.org/10.1016/j.wear.2006.03.015.

(94) Thomas, T. R.; Sayles, R. S. Some Problems in the Tribology of Rough Surfaces. *Tribol. Int.* **1978**, *11* (3), 163–168. https://doi.org/10.1016/0301-679X(78)90001-4.

(95) Benoit B Mandelbrot, Dann E Passoja, A. J. P. Fractal Character of Fracture Surfaces of Metals. *Nature* **1991**, *308* (5961), 721. https://doi.org/10.3323/jcorr1991.40.498.

(96) Yang, C.; Persson, B. N. J. Molecular Dynamics Study of Contact Mechanics: Contact Area and Interfacial Separation from Small to Full Contact. *Phys. Rev. Lett.* **2008**, *100* (2). https://doi.org/10.1103/PhysRevLett.100.024303.

(97) Silberzan, P.; Perutz, S.; Kramer, E. J.; Chaudhury, M. K. Study of the Self-Adhesion Hysteresis of a Siloxane Elastomer Using the JKR Method. *Langmuir* **1994**, *10* (7), 2466–2470. https://doi.org/10.1021/la00019a073.

(98) Choi, G. Y.; Kim, S.; Ulman, A. Adhesion Hysteresis Studies of Extracted Poly(Dimethylsiloxane) Using Contact Mechanics. *Langmuir* **1997**, *13* (23), 6333–6338. https://doi.org/10.1021/la970525d.

(99) Vorvolakos, K.; Chaudhury, M. K. The Effects of Molecular Weight and Temperature on the Kinetic Friction of Silicone Rubbers. *Langmuir* **2003**, *19* (17), 6778–6787. https://doi.org/10.1021/la027061q.

(100) Chen, Y. L.; Helm, C. A.; Israelachvili, J. N. Molecular Mechanisms Associated with Adhesion and Contact Angle Hysteresis of Monolayer Surfaces. *J. Phys. Chem.* **1991**, *95* (26), 10736–10747. https://doi.org/10.1021/j100179a041.

(101) Pickering, J. P.; Van Der Meer, D. W.; Vancso, G. J. Effects of Contact Time, Humidity, and Surface Roughness on the Adhesion Hysteresis of Polydimethylsiloxane. *J. Adhes. Sci. Technol.* **2001**, *15* (12), 1429–1441. https://doi.org/10.1163/156856101753213286.

(102) Kesari, H.; Doll, J. C.; Pruitt, B. L.; Cai, W.; Lew, A. J. Role of Surface Roughness in Hysteresis during Adhesive Elastic Contact. *Philos. Mag. Lett.* **2010**, *90* (12), 891–902. https://doi.org/10.1080/09500839.2010.521204.

(103) Peressadko, A. G.; Hosoda, N.; Persson, B. N. J. Influence of Surface Roughness on Adhesion between Elastic Bodies. *Phys. Rev. Lett.* **2005**, *95* (12), 1–4. https://doi.org/10.1103/PhysRevLett.95.124301.

(104) Yurdumakan, B.; Harp, G. P.; Tsige, M.; Dhinojwala, A. Template-Induced Enhanced Ordering under Confinement. *Langmuir* **2005**, *21* (23), 10316–10319. https://doi.org/10.1021/la051760w.

(105) She, H.; Malotky, D.; Chaudhury, M. K. Estimation of Adhesion Hysteresis at Polymer/Oxide Interfaces Using Rolling Contact Mechanics. *Langmuir* **1998**, *14* (11), 3090–3100. https://doi.org/10.1021/la971061m.

(106) Chaudhury, M. K. Interfacial Interaction between Low-Energy Surfaces. *Mater. Sci. Eng. R Reports* **1996**, *16* (3), 97–159. https://doi.org/10.1016/0927-796X(95)00185-9.

(107) Vaenkatesan, V.; Li, Z.; Vellinga, W. P.; de Jeu, W. H. Adhesion and Friction Behaviours of Polydimethylsiloxane - A Fresh Perspective on JKR Measurements. *Polymer (Guildf).* **2006**, *47* (25), 8317–8325. https://doi.org/10.1016/j.polymer.2006.09.037.

(108) Perutz, S.; Kramer, E. J.; Baney, J.; Hui, C. Y.; Cohen, C. Investigation of Adhesion Hysteresis in Poly(Dimethylsiloxane) Networks Using the JKR Technique. *J. Polym. Sci. Part B Polym. Phys.* **1998**. https://doi.org/10.1002/(SICI)1099-0488(19980915)36:12<2129::AID-POLB11>3.0.CO;2-1.

(109) Liang, H.; Cao, Z.; Wang, Z.; Dobrynin, A. V. Surface Stress and Surface Tension in Polymeric Networks. *ACS Macro Lett.* **2018**, *7* (1), 116–121. https://doi.org/10.1021/acsmacrolett.7b00812.

(110) Chaudhury, M. K.; Whitesides, G. M. Correlation between Surface Free Energy and Surface Constitution. *Science (80-.).* **1992**, *255* (5049), 1230–1232.

(111) Pastewka, L.; Robbins, M. O. Contact Area of Rough Spheres: Large Scale Simulations and Simple Scaling Laws. *Appl. Phys. Lett.* **2016**, *108* (22), 221601. https://doi.org/10.1063/1.4950802.

(112) Weber, B.; Suhina, T.; Junge, T.; Pastewka, L.; Brouwer, A. M.; Bonn, D. Molecular Probes Reveal Deviations from Amontons' Law in Multi-Asperity Frictional Contacts. *Nat. Commun.* **2018**, *9* (1), 888. https://doi.org/10.1038/s41467-018-02981-y.

(113) Persson, B. N. J. Nanoadhesion. *Wear* **2003**, *254* (9), 832–834. https://doi.org/10.1016/S0043-1648(03)00233-3.

(114) Griffith, A. A. The Phenomena of Rupture and Flow in Solids. *Philos. Trans. R. Soc. A Math. Phys. Eng. Sci.* **1921**, *221* (582–593). https://doi.org/10.1098/rsta.1921.0006.

(115) Lee, M.-. M.; Wu, M. C. Thermal Annealing in Hydrogen for 3-D Profile Transformation on Silicon-on-Insulator and Sidewall Roughness Reduction. *J. Microelectromechanical Syst.* **2006**, *15* (2), 338–343. https://doi.org/10.1109/JMEMS.2005.859092.

(116) Shive, L. W.; Gilmore, B. L. Impact of Thermal Processing on Silicon Wafer Surface Roughness Title. *ECS Trans.* **2008**, *16*, 401–405.

(117) Romig, A. D.; Dugger, M. T.; McWhorter, P. J. Materials Issues in Microelectromechanical Devices: Science, Engineering, Manufacturability and Reliability. *Acta Mater.* **2003**, *51* (19), 5837–5866. https://doi.org/https://doi.org/10.1016/S1359-6454(03)00440-3.

(118) Krick, B. A.; Vail, J. R.; Persson, B. N. J.; Sawyer, W. G. Optical In Situ Micro Tribometer for Analysis of Real Contact Area for Contact Mechanics, Adhesion, and Sliding Experiments. *Tribol. Lett.* **2012**, *45* (1), 185–194. https://doi.org/10.1007/s11249-011-9870-y.